JAIST Repository

https://dspace.jaist.ac.jp/

Title	REST-UNet-Based Interference Mitigation for Concurrent PNC Scheme in Full-Duplex Wireless Networks
Author(s)	孫, 健文
Citation	
Issue Date	2025-09
Туре	Thesis or Dissertation
Text version	author
URL	http://hdl.handle.net/10119/20044
Rights	
Description	Supervisor: リム 勇仁, 先端科学技術研究科, 修士 (情報科学)



Master's Thesis

REST-UNet-Based Interference Mitigation for Concurrent PNC Scheme in Full-Duplex Wireless Networks

SUN Jianwen

Supervisor Professor Yuto LIM Second Supervisor Professor Yasuo TAN

Graduate School of Advanced Science and Technology Japan Advanced Institute of Science and Technology Master of Science (Information Science)

October 2025

REST-UNET-BASED INTERFERENCE MITIGATION FOR CONCURRENT PNC SCHEME IN FULL-DUPLEX WIRELESS NETWORKS

By SUN Jianwen (2310415)

A thesis submitted to
School of Information Science,

Japan Advanced Institute of Science and Technology,
in partial fulfillment of the requirements
for the degree of
Master of Science

Supervisor: Professor LIM, Yuto
Main Examiner: Professor LIM, Yuto
Examiners: Professor TAN, Yasuo

Professor KURKOSKI, Brian Michael

Associate Professor BEURAN, Razvan Florin

Graduate School of Advanced Science and Technology Japan Advanced Institute of Science and Technology (Information Science)

August 2025

Abstract

Wireless communication networks face immense pressure to support exponentially increasing data demands and ultra-low latency requirements, yet conventional half-duplex systems waste significant spectral resources due to their inability to transmit and receive simultaneously. This dissertation addresses the pressing need for enhanced throughput and reduced latency by advancing the concept of Physical-Layer Network Coding (PNC) into practical full-duplex operation.

Current wireless relay systems encounter severe performance bottlenecks due to residual self-interference (RSI) inherent in full-duplex operation, which persists even after analog cancellation. To overcome this fundamental limitation, we propose Concurrent Physical-Layer Network Coding (CPNC), the first full-duplex PNC framework that maintains compatibility with 5G New Radio specifications while incorporating a fixed processing delay δ to enable pipelined operation and systematic RSI management. CPNC achieves an average normalized throughput (ANT) of 1.73 at high SNR—a 73% improvement over conventional half-duplex PNC's theoretical limit of 1.0, while approaching 86.5% of the ideal full-duplex capacity.

To fully exploit CPNC's potential under realistic interference conditions, we introduce REST-UNet (Residual Attention U-Net), an innovative deep learning receiver architecture that jointly performs interference suppression, channel estimation, and XOR symbol detection through learned transformations. REST-UNet uniquely integrates multi-scale feature extraction with channel and spatial attention mechanisms, achieving approximately 62% uncoded BER reduction compared to conventional LS+MMSE+LDPC processing and 44% reduction over state-of-the-art DeepRx at 10 dB SNR, while maintaining robustness to channel variations up to 250 Hz Doppler shift.

The seamless integration of REST-UNet into the CPNC framework creates the first comprehensive AI-enhanced full-duplex PNC system. Extensive simulations across diverse ITU indoor scenarios reveal critical design parameters: a minimum RSI suppression threshold of -15 dB for reliable operation, an optimal relay timing window of about 30 μ s, and consistent performance gains across various propagation conditions. The integrated system maintains BER below 10^{-5} even with practical RSI levels, demonstrating feasibil-

ity for real-world deployment.

This research pioneers the convergence of concurrent network coding with AI-enhanced signal processing, delivering practical solutions to the fundamental challenges of full-duplex communication. The proposed framework not only demonstrates substantial throughput gains and latency reduction but also lays the foundation for future 6G wireless systems, where ultrareliable low-latency communication (URLLC) is paramount.

Keywords: Physical-Layer Network Coding (PNC); Full-Duplex Communication; Residual Self-Interference; Deep Learning; REST-UNet; Concurrent Network Coding; 5G New Radio; URLLC

Acknowledgement

First and foremost, I extend my deepest gratitude to **Professor Yuto LIM**, whose invaluable guidance, technical expertise, and continuous encouragement have profoundly shaped every aspect of this thesis. His patient mentorship and insightful discussions have been instrumental in overcoming research obstacles and refining my academic vision.

I would also like to express my sincere appreciation to **Professor Yasuo TAN**. His expansive perspective, insightful suggestions, and constructive critiques have constantly inspired me to broaden the scope of my research. His generous sharing of knowledge has greatly enriched both my theoretical understanding and practical applications.

I am profoundly grateful to **Professor Brian M. KURKOSKI** for supervising my minor research in information theory. His supervision opened new intellectual avenues and strongly influenced the theoretical dimensions of my study. His thoughtful guidance and engaging discussions have significantly expanded my analytical skills and scholarly rigor.

My heartfelt thanks go to my colleagues and friends in the QuWi and TAN laboratories. The stimulating conversations, mutual encouragement, and collaborative spirit within these research groups created an inspiring and enjoyable environment that greatly facilitated my academic progress. Additionally, I deeply appreciate the timely and reliable assistance provided by the JAIST administrative staff, whose efforts have been essential in maintaining a smooth academic journey.

Lastly, and most significantly, I am eternally grateful to my family, whose unwavering support, patience, and steadfast belief in my aspirations have been my strongest foundation. Their continuous encouragement and unconditional love have provided the emotional strength and stability that enabled me to persist and succeed throughout my graduate studies.

Contents

A	bstra	ct		i
\mathbf{A}	cknov	wledge	ement	iii
Li	st of	Figur	es	vii
Li	st of	Table	${f s}$	ix
Li	st of	Symb	ols	X
Li	st of	Abbre	eviations	xix
1	Intr	oduct	ion	1
	1.1	Resear	rch Background	. 1
	1.2	Proble	em Statement	. 3
	1.3	Relate	ed Work and Motivation	. 5
		1.3.1	Information-Theoretic Foundations of PNC	. 5
		1.3.2	From Theory to Practice: Implementation Challenges	
			and Solutions	. 6
		1.3.3	Full-Duplex Integration: Promises and Challenges	. 9
		1.3.4	Deep Learning Revolution in Wireless Communications	10
		1.3.5	Motivation and Research Gap	. 12
	1.4	Resear	rch Objectives	. 13
	1.5	Resear	rch Approach	. 14
	1.6	Resear	rch Methodology	. 16
	1.7	Thesis	S Organization	. 18

2	Bac	kgrou	nd	21
	2.1	Two-V	Way Relay Channel	21
	2.2	Physic	cal-Layer Network Coding	22
	2.3		Ouplex Communication	
	2.4	Signal	Detection in Interference-Limited Environments	28
	2.5	3GPP	⁹ 5G New Radio	30
	2.6	Deep	Learning Architectures for Physical Layer Processing	33
	2.7		nary	
3	\mathbf{Pro}	\mathbf{posed}	REST-UNet Framework for CPNC in Full-Duplex	5
	\mathbf{Sys}	$ ext{tems}$		39
	3.1	System	m Model	39
		3.1.1	Network Model and Protocol Design	39
		3.1.2	Channel Models and Propagation Scenarios	42
		3.1.3	Self-Interference Model and Characterization	44
	3.2	Concu	ırrent Physical-Layer Network Coding (CPNC)	45
		3.2.1	CPNC Architecture and Protocol Design	45
		3.2.2	Constellation-Mapping-Aided CPNC Detection: Fun-	
			damental Limitations	47
		3.2.3	Orthogonal Pilot Design and Channel Estimation for	
			PNC	51
		3.2.4	Constellation-Mapping-Aided CPNC Detection \dots	53
	3.3	REST	7-UNet Architecture for Noise	
		-Inter	ference Suppression	54
		3.3.1	System-Level Integration of REST-UNet	54
		3.3.2	REST-UNet Micro-Architecture	55
		3.3.3	Detailed Module Design	57
		3.3.4	Loss Function	60
	3.4	Integr	rated REST-UNet CPNC System Implementation	61
		3.4.1	Overall System Architecture	61
		3.4.2	Novel Adaptations for CPNC Integration	62
		3.4.3	Training Methodology	63
		3.4.4	Theoretical Performance Analysis	65
4	Sim	ulatio	n Studies and Results	67
	4.1	Simul	ation Parameters and Settings	67

		4.1.1	Computational Environment	67
		4.1.2	REST-UNet Training Setup	67
		4.1.3	PHY Layer Parameters	68
		4.1.4	Baselines and Evaluation Protocols	68
	4.2	CPNC	Simulation Scenarios and Results	69
		4.2.1	CPNC/DF and CPNC/AF	69
		4.2.2	CPNC versus Theoretical PNC: Throughput Analysis .	71
	4.3	REST-	-UNet Simulation	74
		4.3.1	Simulation Scenarios	74
		4.3.2	REST-UNet versus Baselines	75
		4.3.3	Robustness Testing	78
		4.3.4	Scenario-Based Performance Evaluation	79
	4.4	REST-	-UNet-CPNC Simulation Scenarios and Results	81
		4.4.1	Indoor-ITU Channel Model and Preset Scenarios	82
		4.4.2	Comprehensive Performance Studies	83
	4.5	Summa	ary and Insights	93
5	Con	clusior	1	95
	5.1	Conclu	iding Remarks	95
	5.2	Contri	butions	97
	5.3	Future	Works	98
Bi	bliog	raphy		100
Li	st of	Public	cations	106

List of Figures

1.1	Usage scenarios and overarching aspects of IMT-2030[1]	3
1.2	Overview of the research methodology	17
2.1	Conventional vs. PNC Protocol for Two-Way Communication	23
2.2	Antenna Coupling and Multipath Interference Paths	26
2.3	5G NR Physical Layer Specification Structure [2]	31
2.4	U-Net Architecture for Encoder-Decoder Networks [3]	34
2.5	Multi-Head Self-Attention Mechanism	35
2.6	Residual Block in a ResNet Architecture	36
3.1	Full-duplex TWRC topology	40
3.2	OFDM resource-grid processing	41
3.3	CPNC Diagram with Full-Duplex Relay and Self-Interference	
	Paths	45
3.4	CPNC protocol diagram with processing delay δ at the relay $% \delta =0$.	47
3.5	System architecture of the CPNC protocol	48
3.6	OFDM resource grid with pilot symbols	52
3.7	REST-UNet-based receiver framework in an OFDM system	55
3.8	Proposed AI model with cross-attention and hierarchical en-	
	coder–decoder structure	57
3.9	Enhanced UNet block architecture	58
3.10	Channel attention module for adaptive feature weighting $\ \ .$	59
3.11	Grouped convolution with g groups	59
3.12	CPNC framework with REST-UNet-based relay processing	
	pipeline	62
4.1	BER of CPNC/DF and CPNC/AF with and without Rayleigh	
	fading	70

4.2	Bit-level average normalized throughput comparison between	
	PNC and CPNC	72
4.3	Comprehensive performance comparison	76
4.4	Robustness under multiple conditions for two receivers	79
4.5	Performance under multiple scenarios for two receivers	80
4.6	BER vs. SNR showing multipath-induced degradation with	
	$SI = -15 dB \dots$	84
4.7	BER vs. RSI power at different SNRs in ITU indoor scenarios	86
4.8	BER vs. relay wait time δ at different SNRs in ITU indoor	
	scenarios	89
4.9	Bit-level average normalised throughput for CPNC with and	
	without REST-UNet	92

List of Tables

2.1	PNC synchronization tolerances and their impact on system	
	performance	24
2.2	Comparison of detection algorithms for full-duplex PNC systems	29
3.1	PNC Compatibility of Common Modulation Schemes	49
3.2	Curriculum Learning Progression	65
4.1	Core PHY and simulation parameters	68
4.2	ITU indoor pathloss presets used in this study	83
4.3	REST-UNet learnable parameter composition (precision: $10^{-3} \mathrm{M}$)	90
4.4	Estimated inference latency for a single forward pass (50 $\%$	
	hardware utilisation)	91

List of Symbols

The following list describes several symbols that are used within the body of this document:

- $(\cdot)^H$ Hermitian transpose
- $(\cdot)^T$ Transpose
- * Convolution operation
- α Time-varying SI attenuation coefficient
- $\alpha(t)$ Time-varying leakage amplitude

arg min Argument of minimum

- β Residual SI leakage factor
- β_k k-th non-linear coefficient of PA distortion
- **b** Bit label / XOR outcome
- Δf Subcarrier spacing
- δ Fixed processing/forwarding delay at relay
- ϵ Convergence tolerance
- $\eta_{\rm NC}$ Network-coding efficiency factor
- $\exp(\cdot)$ Exponential function
- γ Focal loss parameter
- $\hat{\boldsymbol{b}}_{f,s}$ Estimated XOR bit label at subcarrier f, symbol s

GB Estimated label cube

 $\hat{\mathbf{u}}$ Estimated network-coded word

 \hat{SI}_{canc} Cancelled self-interference

 \hat{b}_i Estimated bit i

 \hat{c}_A Estimated codeword from node A

 \hat{c}_B Estimated codeword from node B

 $\hat{c}_{A \oplus B}$ Estimated XOR codeword

 \hat{p}_i Estimated bit probability

 $\Im\{\cdot\}$ Imaginary part

 λ_0 Base loss weight

 λ_1, λ_2 Loss weighting parameters

 $\lambda_h(t)$ Time-varying loss weight

 λ_{reg} Regularization weight

 λ_{SI} SI loss weight

 $ln(\cdot)$ Natural logarithm

 $\log_2(\cdot)$ Base-2 logarithm

 $\mathbb{E}[\cdot]$ Expected value

 $\Phi_{\rm pilot}$ Pilot phase mask

 $\mathbf{F}_{\mathrm{dec}}$ Final decoder feature map

GB Ground-truth label cube

H Channel matrix

 \mathbf{H}_M Hadamard matrix of size $M \times M$

 \mathbf{h}_{SI} Residual self-interference channel vector

 \mathbf{k}_n Kalman gain vector

 $\mathbf{M}_{\mathrm{data}}$ Data sub-carrier mask

 $\mathbf{M}_{\mathrm{pilot}}$ Pilot amplitude mask

n Noise vector

P Pilot matrix

 \mathbf{p}_A Pilot sequence for node A

 \mathbf{p}_B Pilot sequence for node B

 \mathbf{u} Network-coded word $\mathbf{w}_A \oplus \mathbf{w}_B$

 $\mathbf{W}_1, \mathbf{W}_2$ Learned weight matrices

 \mathbf{w}_A Information word (bit-vector) of node A

 \mathbf{w}_B Information word (bit-vector) of node B

 \mathbf{w}_n Filter weights at time n

X Input tensor for REST-UNet

x Transmitted signal vector

Y Received OFDM grid

y Received signal vector

 \mathbf{Y}_{SI} Self-interference OFDM grid

 $\mathcal{CN}(0,\sigma^2)$ Complex normal distribution

 ${\cal C}$ Constellation set

 C_{total} Total computational complexity

 \mathcal{D} Training dataset

 $\mathcal{I}_{\mathrm{pilot}}$ Set of pilot-bearing sub-carriers

 $\mathcal{L}_{channel}$ Channel estimation loss

 \mathcal{L}_{req} Regularization loss

 \mathcal{L}_{SI} Self-interference loss

 \mathcal{L}_{total} Total loss function

 \mathcal{L}_{XOR} XOR detection loss

 \mathcal{M} Set of bit indices

 $\mathcal{N}(i)$ Neighbors of node i in graph

 $\mathcal{O}(\cdot)$ Big-O complexity notation

 \mathcal{S}_b Composite-constellation subset for XOR label b

 $\mathcal{U}[a,b]$ Uniform distribution on interval [a,b]

ANT Average Normalised Throughput

BER Bit Error Rate

BLER Block Error Rate

 $FLOPs_{tot}$ Total floating-point operations

SNR_{dB} Signal-to-Noise Ratio in dB

SNR Signal-to-Noise Ratio (linear)

 μ Learning rate / step size parameter

 \oplus XOR operation

 \otimes Element-wise multiplication

 $\phi(t)$ Phase-noise process

 $\Re\{\cdot\}$ Real part

 ρ Collision ratio

 $\rho_{\rm SI,0}$ Reference RSI level

 $\rho_{\rm SI}$ Residual self-interference power (dB)

- $\sigma(\cdot)$ Sigmoid activation function
- σ^2 Noise variance
- σ_n^2 AWGN power

 $tanh(\cdot)$ Hyperbolic tangent

- τ_l Delay of the *l*-th multipath tap
- $\tau_{\rm SI}$ Self-interference propagation delay

num_pilot Number of pilot tones

RSI Residual self-interference

 $\mathrm{SI}_{\mathrm{total}}$ Total self-interference

- θ_l Angle of arrival for tap l
- θ_{IQ} I/Q imbalance phase
- A User node A in TWRC
- A_p Pilot amplitude
- B Bits per QAM symbol $(B = \log_2 M)$
- B User node B in TWRC
- $b_{ij,\ell}$ Ground-truth bit value at position (i,j), bit ℓ
- c_A Codeword transmitted by node A
- c_B Codeword transmitted by node B
- c_i, c_j Individual QAM constellation points

 $C_{\text{integrated}}$ Capacity of integrated system

 $C_{\rm in}$ Input channels

 C_{out} Output channels

 C_{BC} Broadcast Channel capacity

 C_{MAC} Multiple-Access Channel capacity

 C_{PNC} Achievable sum-rate of PNC system

d Tx-Rx separation distance

 $d_{\rm m}$ Distance in meters

 e_n Prediction error at time n

 E_s Average symbol energy

F Number of OFDM sub-carriers

f Subcarrier index

 f_k Frequency of the k-th sub-carrier

 $f_{\rm MHz}$ Carrier frequency in MHz

 $f_{D,l}$ Doppler frequency for tap l

 f_D Maximum Doppler frequency

g Number of groups in group convolution

G(x) CRC generator polynomial

 g_I, g_Q I/Q gain-imbalance factors

 G_{AI} Effective SNR gain due to REST-UNet

 $H_{\text{out}}, W_{\text{out}}$ Output height and width

 h_{AA} Self-interference channel at node A

 h_{AR} Channel coefficient from node A to relay

 h_{BB} Self-interference channel at node B

 h_{BR} Channel coefficient from node B to relay

 h_{ij} Complex channel coefficient from node i to node j

 h_{RA} Channel coefficient from relay to node A

 h_{RB} Channel coefficient from relay to node B

 h_{RR} Self-interference channel at relay

K Rician K-factor

k Information bits in LDPC code

 K_h, K_w Kernel height and width

 $L_f(n)$ Total loss of n identical walls/floors

 L_i Log-likelihood ratio of the *i*-th bit

 L_i^* Extrinsic LLR

 $L_i^{(0)}$ Initial LLR

 L_{wall} Wall penetration loss

M Constellation size (M-QAM)

N Distance-path-loss exponent

N Number of subcarriers in OFDM

n Codeword length in LDPC code

n Generic AWGN sample

n(t) Additive noise

 N_0 Noise power spectral density

 N_{iter} Number of LDPC iterations

 $n_{f,s}$ Noise at subcarrier f, symbol s

P Transmit power per node

 P_e Bit-error probability (BER)

 $P_e^{(e2e)}$ End-to-end error probability

 $P_e^{(LDPC)}$ LDPC decoding error probability

 $P_e^{(SI)}$ Self-interference error probability

 $P_e^{(XOR)}$ XOR detection error probability

 P_x Expected signal power

 P_{signal} Desired signal power

 $P_{\rm SI}$ Self-interference power

 $P_{\rm TX}$ Transmit power

 P_{peak} Peak hardware throughput

PL(d) Large-scale path-loss at distance d

 $Q(\cdot)$ Q-function

R Code rate R = k/n

R Relay node in TWRC

r(t) Composite received signal

 $r_A(t)$ Processed received signal at node A

 $r_B(t)$ Processed received signal at node B

 $r_R(t)$ Processed received signal at relay

 R_{PNC} Sum rate of PNC

S Number of OFDM symbols

s OFDM symbol index

 $s_A(t)$ Signal transmitted by node A

 $s_B(t)$ Signal transmitted by node B

 $s_R(t)$ Signal transmitted by relay R

 $s_S(t)$ Self-interference signal estimate

 S_{frame} Number of OFDM symbols per frame

- $s_{R,I}(t)$ In-phase component of relay signal
- $s_{R,Q}(t)$ Quadrature component of relay signal
- t Random arrival offset / propagation delay
- T_0 Baseline hardware latency
- $T_{\rm CP}$ Cyclic-prefix length
- T_{iter} Per-iteration LDPC decoding latency
- $T_{\rm proc}$ Relay processing latency budget
- T_{sym} OFDM symbol duration
- x_A Baseband symbol transmitted by node A
- x_B Baseband symbol transmitted by node B
- X_k Complex symbol on k-th subcarrier
- x_R Signal transmitted by relay R
- y_A Signal received at node A
- y_B Signal received at node B
- y_R Signal received at relay R
- $y_{\rm IQ}(t)$ I/Q imbalance component of self-interference
- $y_{\text{linear}}(t)$ Linear component of self-interference
- $y_{\text{nonlinear}}(t)$ Nonlinear component of self-interference
- $y_{\text{phase}}(t)$ Phase noise component of self-interference
- $y_{\rm SI}$ Residual self-interference component
- $y_{AR}(t)$ Signal from A received at relay
- $y_{BR}(t)$ Signal from B received at relay
- $y_{RA}(t)$ Signal from relay received at A

- $y_{RB}(t)$ Signal from relay received at B
- $y_{RR}(t)$ Self-interference signal at relay
- Z Circulant size in QC-LDPC
- z_A AWGN at node A
- z_B AWGN at node B
- z_R AWGN at relay R
- $z_{(\cdot)}$ Additive white Gaussian noise sample

List of Abbreviations

3GPP 3rd Generation Partnership Project

5G-NR 5G New Radio

6G 6th Generation

ACE Approximate-Cycle-Extrinsic

ADC Analog-to-Digital Converter

AF Amplify-and-Forward

AGV Autonomous Guided Vehicle

AI Artificial Intelligence

ANT Average Normalised Throughput

AOP-LMS Adaptive Orthonormal-Polynomial LMS

AR Augmented Reality

ASIC Application-Specific Integrated Circuit

AWGN Additive White Gaussian Noise

BC Broadcast Channel

BCE Binary Cross-Entropy

BER Bit Error Rate

BLER Block Error Rate

 ${f BN}$ Batch Normalization

BPSK Binary Phase Shift Keying

CDL Clustered Delay Line

CFO Carrier Frequency Offset

CNN Convolutional Neural Network

COSMOS Cloud Enhanced Open Software Defined Mobile Wireless Testbed for City-Scale Deployment

CP Cyclic Prefix

CPNC Concurrent Physical-layer Network Coding

CPU Central Processing Unit

CRC Cyclic Redundancy Check

CSI Channel State Information

DF Decode-and-Forward

DL Deep Learning

DL-FRC Downlink Fixed Reference Channel

DPU Deep Learning Processing Unit

DSP Digital Signal Processor

eMBB Enhanced Mobile Broadband

FD Full-Duplex

FEC Forward Error Correction

FER Frame Error Rate

FFT Fast Fourier Transform

FLOP Floating Point Operation

FPGA Field-Programmable Gate Array

FSK Frequency Shift Keying

GAP Global Average Pooling

GFLOP Giga Floating Point Operation

GNN Graph Neural Network

GPU Graphics Processing Unit

HARQ Hybrid Automatic Repeat Request

HD Half-Duplex

I/Q In-phase and Quadrature

IMT International Mobile Telecommunications

IoT Internet of Things

ISAC Integrated Sensing and Communication

ISI Inter-Symbol Interference

ITU International Telecommunication Union

KPI Key Performance Indicator

LDPC Low-Density Parity-Check

LLR Log-Likelihood Ratio

LMMSE Linear Minimum Mean Square Error

LMS Least Mean Squares

LoS Line-of-Sight

LS Least Squares

LUT Look-Up Table

MAC Multiple Access Channel

MCS Modulation and Coding Scheme

MIMO Multiple-Input Multiple-Output

ML Maximum Likelihood

MMSE Minimum Mean Square Error

mMTC Massive Machine-Type Communications

MSE Mean Square Error

MUI Multi-User Interference

NLoS Non-Line-of-Sight

NPU Neural Processing Unit

NR New Radio

OFDM Orthogonal Frequency Division Multiplexing

PA Power Amplifier

PAM Pulse Amplitude Modulation

PAPR Peak-to-Average Power Ratio

PHY Physical Layer

PNC Physical-layer Network Coding

PRB Physical Resource Block

PSD Power Spectral Density

QAM Quadrature Amplitude Modulation

QC Quasi-Cyclic

QoE Quality of Experience

QPSK Quadrature Phase Shift Keying

ReLU Rectified Linear Unit

REPL Read-Eval-Print Loop

ResNet Residual Network

REST Residual Enhanced Swin Transformer

RF Radio Frequency

RLS Recursive Least Squares

RMS Root Mean Square

RSI Residual Self-Interference

SD Sphere Decoding

SI Self-Interference

SIC Self-Interference Cancellation

SISO Single-Input Single-Output

SNR Signal-to-Noise Ratio

TDL Tapped Delay Line

TFLOP Tera Floating Point Operation

TOP Tera Operations Per Second

TPU Tensor Processing Unit

TS Time Slot

TWRC Two-Way Relay Channel

U-Net U-shaped Network

UAV Unmanned Aerial Vehicle

ULLHR Ultra-Low Latency and High Reliability

URLLC Ultra-Reliable Low-Latency Communications

USB Universal Serial Bus

V2I Vehicle-to-Infrastructure

 $\mathbf{V2V}$ Vehicle-to-Vehicle

V2X Vehicle-to-Everything

VR Virtual Reality

 $\mathbf{Wi} ext{-}\mathbf{Fi}$ Wireless Fidelity

XOR Exclusive OR

 \mathbf{XR} Extended Reality

ZF Zero-Forcing

Chapter 1

Introduction

Wireless communication has become a foundational infrastructure for contemporary and future societies [4]. It underpins everything from personal connectivity to national critical services, enabling ubiquitous access to information, seamless human—machine interaction, and large-scale machine-type connectivity. As digital transformation accelerates and cyber—physical systems proliferate, the requirements placed on wireless networks are no longer incremental but transformative: networks must deliver orders-of-magnitude higher throughput (toward the terabit-per-second regime), millisecond-level end-to-end latency, extreme reliability, and the capability to connect billions of heterogeneous devices [1]. Meeting these demands compels the exploration of new architectures and physical-layer strategies that transcend the limitations of conventional half-duplex relaying and strictly orthogonal access.

1.1 Research Background

The past decades have witnessed an explosive surge in wireless traffic, service diversity, and the tight coupling between cyberspace and the physical world. Looking beyond 5G, 6G communication will support the following expected scenarios of applications in future wireless network systems:

• Enhanced Mobile Broadband-Plus (eMBB-Plus): In 6G, eMBB -Plus will replace 5G's eMBB. It targets These-level aggregate throughput, wide-area coverage, and superior Quality of Experience (QoE) for

ultra-high-resolution XR/VR/AR streaming, holographic communications, and real-time digital-twin rendering [5].

- Ultra-Low Latency and High Reliability (ULLHR) Communications: Mission- and safety-critical services—such as cooperative autonomous driving (V2V/V2I), remote/tactile control, telemedicine, and industrial closed-loop control—demand end-to-end latencies of only a few milliseconds (or even sub-millisecond), extremely low jitter, and "six-nines" (or higher) reliability under highly dynamic topologies [6].
- Massive Machine-Type Communications-Plus (mMTC-Plus): Smart factories and Society 5.0 (Super Smart Society) feature billions of heterogeneous sensors and actuators engaged in continuous monitoring, collaborative robotics, and AI-driven decision making [7].

While the three headline service classes delineate the dominant traffic patterns of 6G, the IMT-2030 vision in Fig. 1.1 reminds us that these examples are far from exhaustive. Future wireless systems must also underpin pervasive IoT ecosystems, immersive social platforms, integrated sensing-and-communication (ISAC), ubiquitous AI-native services, and other yet-to-emerge paradigms.

Across these use cases, several key performance indicators (KPIs) consistently emerge: (i) extreme spectral efficiency and multi-Gbps to Tbps throughput; (ii) sub-10 ms—down to sub-1 ms—end-to-end latency with tight jitter bounds; (iii) ultra-high reliability and availability; (iv) massive, flexible connectivity and scalability; and (v) energy- and cost-efficiency for sustainable deployment.

Meeting such stringent KPIs requires rethinking physical-layer design, interference management, resource allocation, and network architectures. Challenges include accurate and timely acquisition of channel state in time-varying environments, mitigation of various interference sources, synchronization and coordination between densely deployed nodes, and balancing algorithmic optimality against real-time computational complexity. This chapter positions these macro-level demands and challenges, and prepares the ground for the subsequent sections on research motivation, objectives, methodology, and the structure of this thesis.

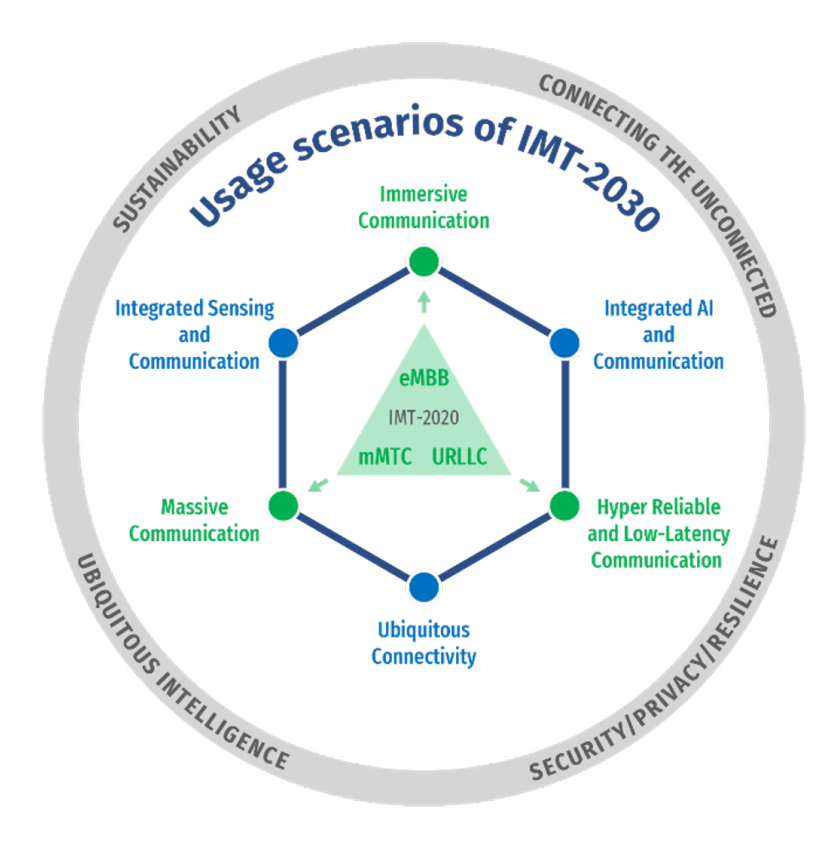


Figure 1.1: Usage scenarios and overarching aspects of IMT-2030[1]

1.2 Problem Statement

With the rapid evolution of society toward hyper-connected, intelligent environments—dominated by applications such as smart factories, the Internet of Things (IoT), autonomous driving, immersive XR/VR platforms, and collaborative robotics—wireless networks are required to support unprecedented volumes of data and real-time, multi-directional interactions among a massive number of devices. These emerging services impose stringent performance demands: extremely high throughput to accommodate continuous high-resolution data streams, ultra-low latency to enable instantaneous control and feedback, and exceptional reliability to ensure mission-critical operations function safely and predictably.

Challenge 1 — Throughput bottlenecks under conventional relaying. High data-rate services demand that every Hertz of spectrum be used efficiently. Classical half-duplex relaying and strictly orthogonal access

consume multiple time slots to exchange information, squandering spectral resources. *Physical-layer Network Coding (PNC)* was introduced to tackle this: by exploiting signal superposition and decoding a network-coded combination (e.g., XOR), PNC cuts the number of transmissions and lifts spectral efficiency. Yet, in practice, imperfect CSI, synchronization errors, and residual interference prevent PNC from reaching its theoretical ceiling—leaving a gap between desired and achievable throughput.

Challenge 2 — Latency floors that motivate simultaneous transmit—receive operation. Emerging services also impose ultra-low latency constraints. Even with PNC, if nodes still separate transmit and receive phases, control/feedback loops suffer avoidable delays. This motivates enabling nodes to transmit and receive at the same time on the same band (full-duplex operation) to collapse time slots and further trim latency. However, adopting full-duplex is not merely a switch; it fundamentally reshapes the interference landscape and hardware/algorithm requirements.

Challenge 3 — Interference and channel impairments amplified by full-duplex and multi-hop processing. Once full-duplex is introduced, strong self-interference arises: the node's own transmit signal, often orders of magnitude stronger than the desired incoming signal, leaks into the receiver. Even state-of-the-art analog/digital cancellation leaves residual power that degrades detection. Simultaneously, PNC's relay-based processing means each information stream effectively experiences multiple channel passages, accumulating noise, fading distortions, and multi-user interference. Together, these effects lift the BER floor and erode the latency/throughput gains that motivated PNC and full-duplex in the first place.

Toward intelligent interference mitigation: opportunities and caveats of AI. Advanced artificial intelligence (AI) methods—especially deep learning—offer a promising way to model nonlinear channel dynamics, learn complex interference patterns, and make near-optimal decisions under uncertainty without exhaustive analytical derivations. AI-based receivers can, in principle, reduce bit error rates (BER), adapt to time-varying environments, and approach real-time operation with carefully designed architectures. However, AI also brings its own limitations: large labeled datasets are often required for robust training; generalization to unseen channel conditions can be fragile; inference complexity and latency must be tightly controlled

to meet real-time constraints; and interpretability, stability, and power consumption remain critical concerns in practical deployments.

1.3 Related Work and Motivation

A rich body of literature has shaped Physical-layer Network Coding (PNC) from its information-theoretic origins through to practical implementations, and more recently toward deep-learning-enhanced receivers. This section provides a comprehensive review of these research strands—capacity analysis, modulation/coding techniques, full-duplex (FD) integration, and AI-driven detection—to establish the theoretical foundations and practical challenges that motivate this thesis.

1.3.1 Information-Theoretic Foundations of PNC

The concept of Physical-layer Network Coding emerged as a paradigm shift in wireless relay networks, fundamentally challenging the traditional "decode-and-forward" approach. Zhang's seminal work [8] introduced the two-way relay channel (TWRC) model, demonstrating that by exploiting the additive nature of electromagnetic waves, a relay node could extract network-coded information directly from superimposed signals. This breakthrough showed that the traditional four-phase communication process could be reduced to just two phases, effectively doubling the spectral efficiency. The key insight was that the relay need not separate individual messages; instead, it could compute and forward a function of the received signals, typically their XOR combination.

Building upon this foundation, Popovski and Yomo [9] extended the analysis to practical wireless environments, quantifying achievable rate gains under various fading distributions and signal-to-noise ratio (SNR) conditions. Their work revealed that PNC maintains significant advantages even in realistic channel conditions, though performance gains are sensitive to channel symmetry and power control strategies. This analysis was crucial in establishing PNC's viability beyond idealized theoretical models.

The capacity region characterization received rigorous treatment from Ong et al. [10], who precisely delimited scenarios where PNC achieves optimal information-theoretic performance. Their work established that PNC is capacity-achieving for symmetric channels and near-optimal for moderately asymmetric configurations, providing clear guidelines for system design. Furthermore, they identified the critical role of side information at end nodes, showing how network coding exploits this structure to approach cut-set bounds.

A significant theoretical advancement came through the compute-and-forward framework introduced by Nazer and Gastpar [11]. This approach formalized PNC within the structured lattice code framework, enabling relays to decode integer linear combinations of transmitted codewords. The elegance of this framework lies in its ability to transform the interference problem into a feature: carefully designed lattice codes ensure that the superposition of codewords remains decodable as another valid codeword. Subsequent refinements by Sezgin et al. [12] tightened capacity bounds for asymmetric channels, while Wilson et al. [13] developed optimal mapping strategies for finite-field network codes. Nam et al. [14] further extended these results to multi-way relay channels, demonstrating that the gains of PNC scale favorably with network size.

1.3.2 From Theory to Practice: Implementation Challenges and Solutions

While theoretical analyses established PNC's promise, translating these gains into practical systems revealed numerous implementation challenges. Real-world wireless systems suffer from hardware impairments, synchronization errors, and channel estimation inaccuracies that can severely degrade PNC performance.

Hardware Impairments and Synchronization

Early implementation efforts faced significant challenges from carrier frequency offsets (CFO) and timing misalignments between end nodes. Lu et al. [15] developed one of the first real-time PNC prototypes, implementing sophisticated algorithms to handle oscillator drifts and sampling clock offsets. Their system demonstrated that with careful design, PNC could maintain reliable operation even with CFO values up to 10 ppm, though

performance degradation became noticeable beyond 5 ppm. The key innovation was a joint CFO estimation and compensation scheme that exploited the correlation structure of superimposed training sequences.

RF non-linearities posed another practical hurdle. Power amplifier distortions and I/Q imbalances can destroy the linear superposition property that PNC relies upon. Practical solutions included digital pre-distortion techniques and careful operating point selection to maintain linearity while achieving reasonable power efficiency.

Constellation Design and Mapping Strategies

A critical implementation aspect involves designing constellation mappings that preserve the network coding structure after superposition. Zhang et al. [16] tackled this challenge for high-order QAM constellations, developing systematic mapping rules that ensure unique decodability of the XOR operation from received superimposed symbols. Their approach introduced the concept of "clustering" in the constellation space, where multiple superposition outcomes mapping to the same network-coded symbol are grouped to maximize minimum distance.

The constellation design problem becomes more complex with asymmetric channels. Adaptive mapping strategies that adjust to channel conditions while maintaining the network coding structure were explored, leading to significant performance improvements in practical scenarios. These designs must balance multiple objectives: maintaining sufficient Euclidean distance between decision regions, ensuring unique decodability of the network-coded information, and adapting to varying channel conditions.

Channel Coding Integration

Integrating channel coding with PNC presented unique challenges and opportunities. Chen et al. [17] pioneered the design of LDPC codes specifically tailored for PNC systems. Unlike traditional point-to-point codes, PNC-optimized codes must account for the fact that the relay observes a noisy superposition rather than individual codewords. Their approach involved modifying the parity-check matrix structure to align with the XOR mapping at the physical layer, achieving near-capacity performance in symmetric

channels.

Iterative detection and decoding schemes further enhanced performance. By exchanging soft information between the PNC demapper and channel decoder, these systems could approach theoretical limits even with practical, finite-length codes. The design of efficient message-passing schedules and approximation techniques for reducing computational complexity became active research areas.

Multi-Antenna Systems and Beamforming

The extension to multiple-input multiple-output (MIMO) scenarios opened new dimensions for PNC optimization. Lee and Hong [18] developed joint precoding and beamforming strategies for multi-antenna relays, showing that spatial processing could mitigate channel asymmetry effects. Their work demonstrated that with M antennas at the relay, the system could support up to M simultaneous two-way exchanges, dramatically increasing network capacity.

Spatial processing also provided additional degrees of freedom for interference management. By carefully designing transmit precoders at end nodes and receive beamformers at the relay, the effective channels could be shaped to enhance PNC performance while suppressing unwanted interference terms.

OFDM Integration and Frequency-Selective Channels

Modern wireless systems predominantly use OFDM, necessitating PNC adaptation to frequency-selective channels. Wu et al. [19] developed subcarrier pairing and power allocation algorithms that maximize PNC throughput in OFDM systems. The key insight was that different subcarriers experience different channel conditions, and intelligent resource allocation could exploit this diversity.

Liu et al. [20] further advanced this work by introducing adaptive modulation schemes that adjust constellation size and coding rate on a per-subcarrier basis. Their system demonstrated that with proper adaptation, PNC-OFDM could maintain high spectral efficiency even in severely frequency-selective channels with delay spreads exceeding the cyclic prefix length.

1.3.3 Full-Duplex Integration: Promises and Challenges

The emergence of full-duplex (FD) radio technology offered another dimension for improving spectral efficiency. By enabling simultaneous transmission and reception on the same frequency band, FD operation promised to double spectral efficiency—a gain that compounds multiplicatively with PNC's benefits.

Self-Interference Cancellation Achievements

Breakthrough demonstrations by Choi et al. [21] and Bharadia et al. [22] achieved over 100 dB of self-interference cancellation through combinations of antenna isolation, analog cancellation circuits, and digital processing. These prototypes proved that FD operation was feasible in practice, spurring intense research activity.

However, Sabharwal et al. [23] provided a comprehensive analysis showing that residual self-interference remains a fundamental limitation. Even with state-of-the-art cancellation, residual interference power typically exceeds thermal noise by 20-30 dB, creating an elevated noise floor that impacts system performance. Everett et al. [24] further characterized the statistical properties of residual self-interference, showing that it exhibits memory effects and non-Gaussian characteristics due to nonlinear distortions in the cancellation process.

FD-PNC Integration Challenges

Despite the individual successes of FD and PNC technologies, their combination presents unique challenges that have received limited attention. Early explorations already hinted at FD-PNC's potential. Rankov and Wittneben [25] analytically characterized the full-duplex two-way relay channel (TWRC) and showed that, under ideal self-interference (SI) suppression, the sum-rate can double relative to half-duplex operation. Building on this theory, Tedik et al. [26] implemented a single-antenna FD-PNC prototype with BPSK signalling and confirmed a two-fold throughput gain, albeit under the assumption of more than 70 dB analog SI cancellation and a narrowband flat-fading channel. These pioneering studies, however, neither considered modern OFDM numerology nor addressed the severe BER floors that arise

when residual SI, multipath fading and linear receivers intersect. Li et al. [27] provided one of the first theoretical treatments of FD-PNC systems, deriving capacity bounds and optimal power control strategies. Their analysis revealed that the benefits are highly sensitive to the residual self-interference level: while ideal FD-PNC could theoretically quadruple spectral efficiency compared to half-duplex systems without network coding, practical gains are often limited to $2\text{-}3\times$ due to self-interference effects.

Wu et al. [28] explored relay selection strategies in FD-PNC networks, showing that the optimal relay choice differs significantly from half-duplex scenarios. The presence of self-interference creates complex trade-offs: relays with better self-interference cancellation capabilities might be preferred even if they have worse channel conditions to end nodes.

Most concerning are the results from Zhang et al. [29], who demonstrated severe BER floors when applying conventional linear receivers (zero-forcing and MMSE) to FD-PNC systems. Their analysis showed that the combination of residual self-interference, amplified noise from linear processing, and channel estimation errors creates a performance wall that cannot be overcome by simply increasing transmit power. These results highlight the inadequacy of traditional signal processing approaches for FD-PNC systems and motivate the exploration of more sophisticated, nonlinear detection methods.

1.3.4 Deep Learning Revolution in Wireless Communications

The application of deep learning (DL) to wireless communications has emerged as a transformative approach, offering new tools to tackle longstanding challenges in receiver design.

End-to-End Learning Paradigm

O'Shea and Hoydis [30] introduced the revolutionary concept of treating the entire communication link as an autoencoder. By jointly optimizing transmitter and receiver neural networks through gradient descent, their approach could discover novel modulation schemes and detection algorithms tailored to specific channel conditions. This work challenged the traditional separation of communication system components and demonstrated that end-to-end

learning could discover solutions superior to conventional designs in certain scenarios.

Neural Network Architectures for Detection

The adaptation of successful computer vision architectures to wireless communications yielded impressive results. Ye et al. [31] showed that convolutional neural networks (CNNs) could jointly perform channel estimation and symbol detection, outperforming traditional MMSE approaches by 3-5 dB in severe multipath channels. The key advantage was the CNN's ability to learn and exploit channel correlation patterns that are difficult to model analytically.

Honkala's DeepRx framework [32] demonstrated remarkable generalization capabilities across different 5G numerologies and channel conditions. By training on diverse scenarios and employing domain adaptation techniques, the system could maintain near-optimal performance without explicit knowledge of current channel statistics—a significant advantage in rapidly varying environments.

Advanced Architectures and Attention Mechanisms

Recent advances have incorporated more sophisticated neural network architectures. Huang et al. [33] applied transformer-based attention mechanisms to MIMO detection, showing that attention weights could automatically learn to focus on relevant spatial streams while suppressing interference. This approach achieved near-maximum likelihood performance with polynomial rather than exponential complexity scaling.

Residual networks, explored by Kim et al. [34], addressed the training difficulties of deep detection networks. By incorporating skip connections and careful normalization, these architectures could be trained to much greater depths, enabling more complex function approximation while maintaining stable gradient flow.

Graph Neural Networks for Large-Scale Systems

The application of graph neural networks (GNNs) to massive MIMO detection, pioneered by Jeon et al. [35] and extended by Jiang et al. [36], repre-

sents a particularly promising direction. By representing the MIMO system as a graph where nodes correspond to antennas and edges capture channel correlations, GNNs can efficiently process high-dimensional problems. The message-passing structure of GNNs naturally aligns with iterative detection algorithms while offering learnable, adaptive processing.

Limitations and Open Challenges

Despite these advances, applying DL to FD-PNC systems remains largely unexplored. Existing DL receivers are designed for point-to-point channels or conventional MIMO systems, not accounting for the unique challenges of network coding and full-duplex operation. The combination of self-interference, network coding constraints, and ultra-low latency requirements presents a complex optimization landscape that standard neural architectures may struggle to navigate.

1.3.5 Motivation and Research Gap

The comprehensive review of existing literature reveals several critical observations that motivate this thesis:

First, while PNC has strong theoretical foundations and proven implementation feasibility, practical deployments still face significant performance gaps. Real-world impairments—hardware non-idealities, synchronization errors, and channel estimation inaccuracies—degrade performance far below theoretical predictions. Traditional linear processing methods lack the flexibility to adapt to these complex, often non-linear impairment patterns.

Second, full-duplex technology offers compelling benefits for latency reduction and spectral efficiency improvement, yet its integration with PNC remains poorly understood. The limited existing work reveals fundamental challenges: residual self-interference creates an elevated noise floor, conventional receivers exhibit error floors, and the joint optimization of FD and PNC parameters presents a complex, non-convex problem. The few studies addressing FD-PNC rely on simplistic channel models and conventional linear receivers that fail to capture real-world complexities.

Third, deep learning has demonstrated remarkable success in wireless communications, particularly in scenarios with complex interference pat-

terns and non-linear channel effects. However, these advances have not been systematically applied to FD-PNC systems. The unique challenges of FD-PNC—including the need to preserve network coding structure while managing self-interference—require specialized neural architectures and training strategies that have not been developed.

Fourth, emerging applications in industrial IoT, autonomous vehicles, and haptic communications demand ultra-low latency and high reliability (ULLHR) that current FD-PNC solutions cannot provide. Meeting submillisecond latency targets while maintaining packet error rates below 10^{-5} requires fundamental advances in detection algorithms and system design.

These observations reveal a clear research gap: the need for an interference-resilient, low-latency, and high-reliability detection framework that intelligently integrates AI capabilities into FD-PNC systems. This thesis addresses this gap by developing novel neural network architectures specifically designed for FD-PNC, incorporating domain knowledge through physics-informed learning, and demonstrating practical feasibility through comprehensive simulations and prototype implementations. By bridging the divide between FD-PNC's theoretical promise and practical limitations through principled application of deep learning, this work aims to enable next-generation ULLHR wireless services.

1.4 Research Objectives

Building upon the identified research gaps, this thesis pursues three tightly coupled objectives that progressively advance from theoretical framework development through AI-enhanced detection to system-level integration:

1. Design and validate a 5G-compatible FD-PNC framework: Develop a comprehensive full-duplex physical-layer network coding architecture seamlessly integrated with 5G New Radio (NR) specifications, including OFDM numerologies, frame structures, and reference signal patterns. Establish theoretical performance bounds considering practical constraints such as residual self-interference, channel estimation errors, and hardware impairments, validated through extensive link-level simulations. Key performance indicators focus on system throughput improvements compared to half-duplex baselines, latency reduction,

and complexity-performance trade-offs under varying channel conditions. The emphasis on throughput and latency aligns directly with URLLC requirements by enabling reliable communication with ultralow latency and high throughput.

- 2. Develop an AI-based receiver architecture for joint interference and channel learning: Design a novel neural network-based receiver that jointly addresses the compound challenges posed by residual self-interference, superimposed PNC signals, and time-varying wireless channels. The receiver will leverage deep learning's non-linear approximation capabilities combined with domain-specific, physics-informed architectural enhancements. Detection accuracy must meet future 6G and URLLC standards, achieving stringent BER/FER performance criteria. Robustness to distribution shifts under realistic operating conditions will be assessed.
- 3. System integration and comprehensive performance characterization: Integrate the AI-enhanced receiver into the FD-PNC processing chain, addressing practical implementation challenges such as pilot pattern adaptation, soft-output generation for channel decoders, and latency budget allocation. Evaluate the comprehensive performance of the combined REST-UNet CPNC system, particularly analyzing BER performance across varying indoor scenarios and signal-to-noise ratios (SNR). Ensure compliance with URLLC standards, thoroughly investigating the system's resilience to residual self-interference and verifying critical system parameters through detailed performance analyses.

1.5 Research Approach

The research follows a systematic progression that mirrors the hierarchical nature of the objectives, ensuring each phase builds upon validated foundations from the previous stage.

Phase 1: FD-PNC Framework Development and Characterization

We begin by establishing a rigorous mathematical framework for 5G-compatible FD-PNC systems. This framework encompasses a unified baseband-to-RF signal model that captures the complete signal flow: simultaneous transmission and reception at the FD relay, residual self-interference after cascaded analog and digital cancellation stages, superimposed signals from multiple users exploiting the PNC principle, and realistic channel effects including frequency-selective fading and Doppler spread. Critical hardware impairments—I/Q imbalance, power amplifier non-linearity, and ADC quantization noise—are incorporated to ensure practical relevance.

These theoretical results guide the development of a high-fidelity link-level simulator implemented in MATLAB/Python, featuring modular architecture for component-wise analysis and bit-accurate signal processing chains. Baseline receivers (zero-forcing, linear MMSE, and sphere-decoding-based near-ML detection) are implemented and benchmarked across diverse scenarios, revealing fundamental performance limitations and establishing the performance gap that motivates AI-based solutions.

Phase 2: AI Receiver Design and Training

The core innovation lies in reformulating the FD-PNC detection problem as a learnable mapping from received signal observations to transmitted information symbols. This abstraction bypasses traditional signal processing blocks, enabling the neural network to discover optimal detection strategies unconstrained by conventional assumptions. The AI receiver architecture specifically addresses how to effectively utilize attention mechanisms to learn channel impairments and variations in real-time signal conditions. Multihead attention modules are incorporated to dynamically focus on relevant temporal and spectral components of the received signals, enhancing the network's ability to capture frequency-selective fading and Doppler effects.

The training dataset is generated using the validated simulator from Phase 1, ensuring the neural network learns from realistic and diverse signal conditions. Scenarios include various modulation schemes, diverse mobility conditions (0-500 km/h), and distinct propagation environments (urban, suburban, and rural). The training process emphasizes generalization to diverse channel impairments without explicitly modeling self-interference or employing curriculum learning strategies. The performance is optimized based solely on the accuracy of symbol detection, enabling focused training that enhances

the AI model's robustness and adaptability to complex channel dynamics.

Phase 3: Integration and System-Level Validation

The trained AI receiver is integrated into the FD-PNC processing chain via interfaces designed to maintain 5G compatibility, emphasizing synchronization with existing pilot structures and compatibility with turbo/LDPC decoding schemes through soft-output generation. The integrated system undergoes rigorous end-to-end BER performance evaluations, comparing the AI receiver against conventional baseline approaches across various scenarios.

Robustness to environmental variations, including fluctuations in channel characteristics, mobility-induced Doppler shifts, and hardware impairments such as synchronization offsets and ADC quantization noise, is thoroughly investigated. Extensive sensitivity analyses reveal performance resilience under realistic deployment conditions, highlighting the practical advantages and reliability of the proposed AI-based approach.

These comprehensive evaluations culminate in practical design guidelines that map application-specific requirements—particularly ultra-low latency—onto recommended configurations. This guidance supports informed deployment decisions for ultra-low latency and high-reliability (ULLHR) services, demonstrating the AI receiver's viability as a pivotal component in next-generation wireless communication systems.

1.6 Research Methodology

This study adopts a five-phase workflow that couples rigorous theory with data-driven development (Figure 1.2). Each phase is summarised below in narrative form to avoid excessive subdivision.

Phase 1 — Literature Review & Theoretical Framing. A critical survey of physical-layer network coding, full-duplex radio, and deep learning in wireless systems establishes current knowledge, uncovers gaps, and sets quantitative performance targets. Parallel mathematical analysis derives baseline limits and clarifies where analytical methods must yield to simulation or learning.

Phase 2 — System Modelling & Data Generation. Guided by Phase 1, we construct a multi-layer model that blends realistic radio-frequency propagation, measured hardware impairments, and representative traffic pat-

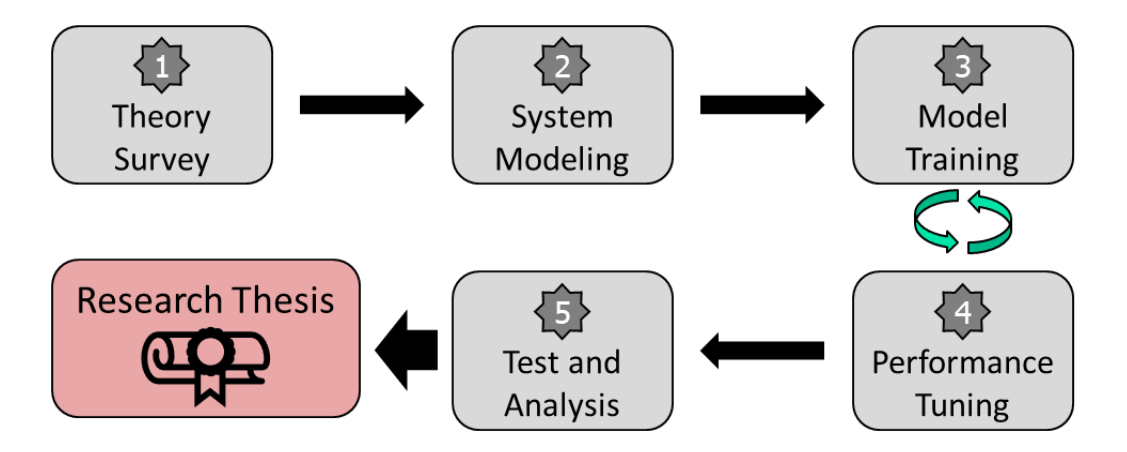


Figure 1.2: Overview of the research methodology

terns. The simulator then produces statistically rich datasets that span the operational envelope; limited real measurements are injected to reduce the simulation-to-reality gap.

Phase 3 — Model Development & Training. Custom neural architectures are designed with domain knowledge in mind, implemented in PyTorch, and trained using staged curricula that gradually raise task difficulty. Hyper-parameters are tuned automatically, while transfer learning seeds training when suitable pre-trained weights exist.

Phase 4 — Optimisation & Refinement. Iterative experiments refine both network structure and training protocol. Techniques such as pruning, quantisation, and knowledge distillation trim latency and power without sacrificing accuracy, whereas adversarial and domain-adaptation strategies harden robustness.

Phase 5 — Comprehensive Testing & Analysis. The final models undergo exhaustive evaluation over standard benchmarks, stress tests, and resource-profiling scenarios. Results are benchmarked against classical receivers and theoretical bounds, with interpretability tools revealing the learned signal features. Insights gained here loop back to earlier phases whenever discrepancies surface.

Iterative Feedback & Knowledge Transfer. Because later findings frequently motivate earlier revisions, feedback loops connect all phases. The project concludes by releasing code, data, and guidelines under open licences and by publishing the main results in peer-reviewed venues, ensuring repro-

ducibility and community impact.

1.7 Thesis Organization

This dissertation is composed of five chapters. Each chapter is crafted to move the reader from macro-level motivation to concrete system design, and finally to empirical evidence and forward-looking insights. A detailed overview follows.

- Chapter 1 Introduction. Sets the stage by positioning future wireless services (XR/VR, massive IoT, autonomous mobility, smart factories) and distilling their stringent KPIs (Tbps-level throughput, sub-ms latency, ultra-high reliability). It formulates the core research problem as three coupled challenges (throughput, latency, interference), articulates why combining network coding and simultaneous transmit—receive operation is compelling yet difficult, and discusses the promise and caveats of AI. The chapter then states the research gap, refines the problem statement, and presents the thesis objectives, approach, and main contributions. A roadmap of the remaining chapters is provided to orient the reader.
- Chapter 2 Background and Related Work. Provides the conceptual and historical background required to understand the proposed solution. It first reviews the theoretical underpinnings of physical-layer network coding (capacity regions, compute-and-forward, structured codes), then surveys implementation-oriented advances (coding/decoding strategies, beamforming/precoding, high-order modulations, prototype systems). Next, it examines full-duplex operation: cancellation techniques, residual limits, and the sparse literature combining FD with PNC. Finally, it discusses AI-driven PHY receivers (autoencoders, CNN/GNN-based detectors, attention and residual designs), highlighting strengths and existing shortcomings in meeting ultra-low latency/high reliability (ULLHR) targets. The chapter concludes with a synthesized gap analysis that directly motivates the framework proposed in Chapter 3.

- Chapter 3 Proposed Framework and Methodology. Introduces the complete 5G/NR-compatible FD-PNC framework and the overarching research methodology. It formalizes the system model (baseband-to-RF), including residual self-interference, multi-hop channel effects, fading/noise, and hardware impairments, and explains how these are abstracted for AI learning as a standalone SISO mapping. The chapter then details the methodological pipeline: (i) conceptual modelling and theoretical bound derivation; (ii) impairment-aware simulation design and dataset generation; (iii) AI receiver architecture design principles (feature extraction, attention/residual use, loss formulation); (iv) integration strategy back into the FD-PNC chain; and (v) evaluation logic (metrics, baselines, robustness/ablation plans). This chapter serves as the blueprint for the experiments that follow.
- Chapter 4 Experiments and Evaluation. Presents the empirical core of the thesis. It first describes the simulation platform, parameter space (SNR, Doppler, cancellation depth, modulation orders), and dataset construction (synthetic plus optional over-the-air captures). It then reports extensive quantitative results: uncoded BER and LDPC-coded BLER, achievable throughput (bps/Hz), end-to-end latency, computational complexity, and energy estimates. Comparisons are drawn against conventional detectors (ZF, LMMSE) and near-optimal benchmarks to expose BER floors and latency trade-offs. Ablation studies isolate contributions of individual AI components (e.g., attention blocks, auxiliary channel estimation loss), while sensitivity analyses explore robustness to CSI mismatch, hardware nonidealities, bursty interference, and mobility. The chapter also discusses implementation feasibility, including quantization effects and inference latency on representative hardware.
- Chapter 5 Conclusions and Future Work. Summarizes the principal findings, emphasizing how the three objectives were met: (i) a deployable FD–PNC framework for current 5G systems, (ii) an AI receiver that learns interference/channel behavior outside the legacy pipeline, and (iii) successful reintegration with demonstrated gains and robustness. It reflects on practical deployment lessons (complex-

ity-performance trade-offs, dataset considerations, interpretability), and outlines promising future directions such as multi-relay/multi-hop extensions, joint source-channel or cross-layer learning, domain adaptation for non-stationary channels, and hardware co-design for on-device AI inference. The chapter closes with a discussion of how these advances can inform the path toward 6G ULLHR communication systems.

Chapter 2

Background

Modern wireless communication systems face unprecedented challenges in meeting the exponential growth in data traffic and the stringent requirements of emerging applications. The demand for higher spectral efficiency, lower latency, and increased network capacity has driven researchers to explore revolutionary approaches that challenge traditional communication paradigms. This chapter establishes the theoretical foundations for AI-enhanced full-duplex Physical-Layer Network Coding (PNC) systems by systematically presenting the key technological components and their interconnections. We begin with the architectural framework of Two-Way Relay Channels, progress through the principles of Physical-Layer Network Coding and full-duplex communication, examine signal detection challenges in interference-limited environments, contextualize our approach within the 5G New Radio standard, and conclude with deep learning architectures that enable intelligent physical-layer processing.

2.1 Two-Way Relay Channel

The two-way relay channel (TWRC), as illustrated in Fig. 2.1(a), is a canonical three-node model for bidirectional data exchange in which two end nodes, A and B, communicate exclusively through a half-duplex relay R. In the conventional **store-and-forward protocol** the exchange is completed in four

orthogonal time-slots (TS) to avoid mutual interference at R [37, 25]:

- (1) **TS**₁: $A \rightarrow R$ node A sends x_A ; R receives $y_R^{(1)} = h_{AR}x_A + z_R^{(1)}$;
- (2) **TS**₂: $R \to B$ relay forwards a processed version $x_R^{(2)}$; B receives $y_B = h_{RB}x_R^{(2)} + z_B$;
- (3) **TS**₃: $B \rightarrow R$ node B sends x_B ; R receives $y_R^{(3)} = h_{BR}x_B + z_R^{(3)}$;
- (4) **TS**₄: $R \rightarrow A$ relay forwards $x_R^{(4)}$; A receives $y_A = h_{RA} x_R^{(4)} + z_A$.

Here h_{ij} denotes the complex channel coefficient from node i to node j and z_{\bullet} is additive white Gaussian noise (AWGN).

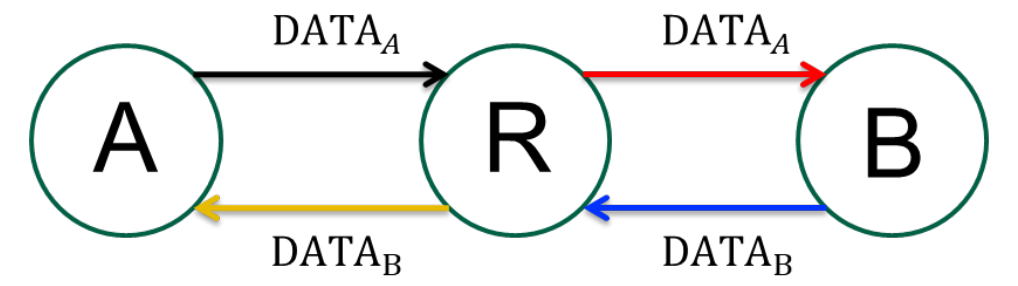
Only one fourth of the total transmission time is effectively used for each direction, capping the spectral efficiency at 25%. This inherent inefficiency motivates more advanced relay strategies—most notably *physical-layer network coding* (PNC) and its variants—which can halve the number of required slots and thereby double throughput. These strategies, however, demand tighter synchronisation and more sophisticated signal processing, topics that are addressed in the following sections.

2.2 Physical-Layer Network Coding

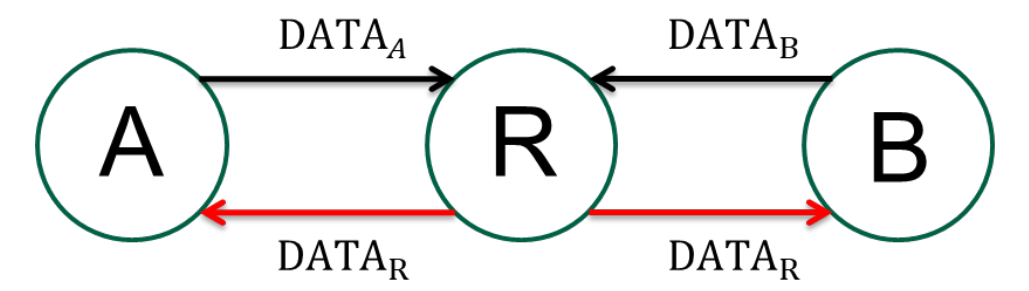
Physical-Layer Network Coding (PNC), depicted in Fig. 2.1(b), represents a paradigm shift in how we view and handle interference in wireless networks. Rather than treating the simultaneous transmissions in TWRC as mutual interference to be mitigated or separated, PNC embraces the superposition and directly decodes a function of the transmitted messages. This approach transforms interference from a fundamental limitation into a capacity-enhancing feature.

The core principle of PNC lies in exploiting the natural computation that occurs when electromagnetic waves superimpose in the wireless channel. Consider the TWRC scenario where nodes A and B transmit binary messages w_A and w_B simultaneously. In traditional approaches, the relay

¹The four-slot baseline is widely referenced; see, e.g., [37] Eq. (1) and the discussion preceding Fig. 1, where the authors remark that "in total four time-slots are usually required to accomplish one round of information exchange."



(a) Conventional store-and-forward protocol



(b) Physical-layer network coding (PNC) protocol



Figure 2.1: Conventional vs. PNC Protocol for Two-Way Communication

would attempt to decode both messages separately. PNC, however, recognizes that for the end nodes to recover their desired messages, the relay only needs to decode and forward the XOR of the two messages:

$$\mathbf{u} = \mathbf{w}_A \oplus \mathbf{w}_B \tag{2.1}$$

This network-coded message is sufficient because each end node, knowing its own transmitted message, can recover the other node's message through a simple XOR operation with the received network-coded packet. The elegance of this approach lies in its alignment with the physical-layer signal combining, effectively performing computation over the air.

The implementation of PNC requires careful consideration of the mod-

ulation and channel coding schemes. For example, with BPSK modulation and assuming perfect channel knowledge and power control such that $h_{AR} = h_{BR} = 1$, the received signal at the relay becomes $y_R = x_A + x_B + z_R$. When both nodes transmit the same bit, the signals add constructively, while opposite bits result in cancellation. This natural mapping can be exploited to directly infer the XOR operation at the signal level.

However, practical implementation faces several challenges. Synchronization emerges as a critical requirement, with timing offsets between the two transmitters needing to be controlled to less than 10% of the symbol duration, as shown in Table 2.1. Carrier frequency offset (CFO) must be maintained below 0.01% to prevent constellation rotation that would destroy the PNC mapping. Phase noise tolerance is similarly stringent, requiring less than 2° RMS to maintain proper I/Q balance for reliable XOR decoding.

Table 2.1: PNC synchronization tolerances and their impact on system performance

Parameter	Tolerance	Impact if exceeded
Timing offset	$< 0.1 T_{\text{sym}} [38]$	BER degradation $> 3 \mathrm{dB}$
Carrier-frequency offset	< 0.01% [38]	mapping failure
Phase noise (RMS)	$< 2^{\circ} [39]$	I/Q imbalance

The theoretical performance of PNC in TWRC approaches the informationtheoretic capacity. Under ideal conditions, PNC achieves a sum rate of:

$$R_{PNC} = \frac{1}{2} \log_2 \left(1 + \frac{P|h_{AR}|^2 + P|h_{BR}|^2}{\sigma^2} \right)$$
 (2.2)

where P is the transmit power of each node and σ^2 is the noise variance. This expression reveals that PNC effectively combines the received powers from both transmitters, achieving a power gain similar to receive diversity.

The extension of PNC to higher-order modulations and multiple relay scenarios introduces additional complexity but also opportunities for further performance gains. Constellation design becomes crucial, as not all modulation schemes naturally support unambiguous PNC mappings. Researchers have developed specialized constellation designs that maintain the desirable one-to-one mapping between superimposed constellation points and XOR values.

While PNC offers compelling theoretical advantages, its practical implementation in modern communication systems requires addressing fundamental hardware limitations. The assumption of half-duplex operation at the relay, where transmission and reception occur in separate time slots, limits the potential gains. This observation motivates the exploration of full-duplex operation, which promises to further enhance spectral efficiency by enabling simultaneous transmission and reception.

2.3 Full-Duplex Communication

The evolution toward full-duplex communication represents one of the most significant paradigm shifts in wireless system design. Traditional wireless systems operate in half-duplex mode, alternating between transmission and reception to avoid the overwhelming self-interference that occurs when a node's own transmitted signal couples into its receive chain. This self-interference can be 90-110 dB stronger than the desired received signal [23], effectively drowning out any useful communication. However, recent advances in interference cancellation techniques have made full-duplex operation increasingly feasible, promising to double spectral efficiency by enabling simultaneous transmission and reception in the same frequency band.

The challenge of full-duplex communication lies in managing the various components of self-interference, illustrated in Figure 2.2. The dominant component is direct coupling between the transmit and receive antennas, where electromagnetic waves travel directly from the transmitting antenna to the receiving antenna through the air or circuit board. This direct path typically results in 0.1-1% of the transmitted power leaking into the receive chainn [21], corresponding to only 20-40 dB of isolation. Given that transmitted signals can be 100 dB or more stronger than received signals in typical scenarios, this isolation is wholly insufficient.

Beyond direct coupling, multipath reflections create additional self-interference components. These reflections arrive with various delays—typically from tens of nanoseconds in small rooms to a few hundred nanoseconds in larger indoor spaces—creating a frequency-selective self-interference channel [40, 41]. The time-varying nature of these reflections, caused by movement in the environment, adds further complexity to the cancellation problem. Addition-

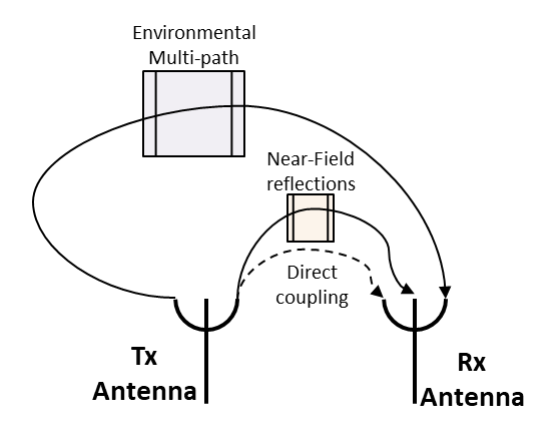


Figure 2.2: Antenna Coupling and Multipath Interference Paths

ally, nonlinear distortions introduced by the power amplifier create harmonic components that cannot be cancelled through linear processing alone. These nonlinear components can be modeled as:

$$y_{NL} = \sum_{k=1}^{K} \alpha_k x^k(t) * h(t)$$
 (2.3)

where α_k represents the k-th order nonlinearity coefficient and h(t) is the self-interference channel impulse response.

Achieving full-duplex operation requires a multi-stage approach to self-interference cancellation. The first stage employs passive suppression techniques in the antenna domain, including physical separation between transmit and receive antennas, electromagnetic shielding, and the use of directional antennas or circulators. These passive techniques can achieve 30–50 dB of suppression but are fundamentally limited by size constraints and the physics of electromagnetic propagation [24].

The second stage involves active analog cancellation in the RF domain, implemented before the analog-to-digital converter to prevent saturation. This stage typically employs a reference signal tapped from the transmit chain, which is processed through analog components including attenuators, phase shifters, and delay lines to create an estimate of the self-interference. When properly tuned, analog cancellation can provide a further 25–40 dB of suppression [22]. However, the limited degrees of freedom in analog processing restrict its ability to handle frequency-selective and time-varying interference.

The final stage of cancellation occurs in the digital domain after analog-to-digital conversion. Digital cancellation leverages sophisticated signal processing algorithms to estimate and subtract residual self-interference. The flexibility of digital processing allows for handling of nonlinear components and fine-grained frequency-selective cancellation. Digital techniques typically achieve 25-30 dB of additional suppression [42], limited primarily by quantization noise, channel estimation errors, and computational complexity.

Despite the layered suppression pipeline, residual self-interference (RSI) is still the dominant bottleneck in practical full-duplex links. A representative budget today is

$$RSI = SI_{total} - \hat{SI}_{canc} \approx \beta P_{TX}, \qquad (2.4)$$

where

- $\beta \approx 10^{-2}$ – 10^{-3} for testbeds that rely mainly on **passive isolation** (directional separation, absorbers, cross-polarised antennas) such as the work by Everett and Sabharwal [24];
- $\beta \approx 3 \times 10^{-3}$ for field platforms that add **frequency-domain RF taps** plus real-time digital SIC, e.g. the COSMOS full-duplex trial bed [43];
- $\beta \approx 10^{-4}$ once an advanced **adaptive digital canceller** such as the Adaptive Orthonormal-Polynomial LMS (AOP-LMS) algorithm is deployed on top of passive + RF stages, pushing digital cancellation to 35–42 dB [44].

Even at the lower end of this range, the residual term lifts the effective noise floor by several decibels, shrinking the post-cancellation SNR and restricting coverage.

Integrating full-duplex radios with physical-layer network coding (PNC) compounds the challenge: the relay must simultaneously suppress its own RSI while decoding the superposed signals from the two end nodes and transmitting the network-coded reply. This highly entangled signal environment demands joint RSI suppression–multi-user detection algorithms that are robust to nonlinear hardware effects and residual carrier offsets.

2.4 Signal Detection in Interference-Limited Environments

The confluence of Physical-Layer Network Coding and full-duplex operation creates an extraordinarily challenging signal detection problem. The received signal at a full-duplex PNC relay contains multiple overlapping components: the desired superimposed signals from both end nodes, residual self-interference from the relay's own transmission, thermal noise, and potentially other environmental interference. This complex signal environment can be mathematically expressed as:

$$y = Hx + h_{SI}x_{SI} + n \tag{2.5}$$

where **H** represents the channel matrix for the desired signals, \mathbf{h}_{SI} is the residual self-interference channel after cancellation, x_{SI} is the self-interference signal, and **n** encompasses thermal noise and other impairments.

Traditional signal detection algorithms, designed for single-user systems or simple interference scenarios, struggle with this multi-dimensional detection problem. The optimal maximum likelihood detector, which would jointly search over all possible combinations of transmitted symbols, faces computational complexity that grows exponentially with the number of users and modulation order. For a system with N users employing M-ary modulation, the complexity scales as $\mathcal{O}(M^N)$, rendering it impractical for real-time implementation even with modest system parameters.

This computational challenge has motivated the development of suboptimal but practical detection algorithms. The Zero-Forcing (ZF) detector attempts to eliminate interference by applying the pseudo-inverse of the channel matrix. While computationally efficient with complexity $\mathcal{O}(N^3)$, ZF suffers from noise enhancement, particularly in ill-conditioned channels or low signal-to-noise ratio scenarios. The Linear Minimum Mean Square Error (LMMSE) detector addresses this limitation by incorporating noise statistics into the detection process:

$$\hat{\mathbf{x}}_{\text{LMMSE}} = (\mathbf{H}^H \mathbf{H} + \sigma^2 \mathbf{I})^{-1} \mathbf{H}^H \mathbf{y}$$
 (2.6)

The linear minimum-mean-square-error (LMMSE) detector achieves near-optimal performance across a wide SNR range by jointly suppressing multi-user/ISI

interference and controlling noise enhancement; the diagonal loading term $\sigma^2 \mathbf{I}$ in $(\mathbf{H}^H \mathbf{H} + \sigma^2 \mathbf{I})^{-1}$ prevents inverting ill-conditioned Gram matrices and thus caps noise amplification [45]. Nevertheless, mainstream LMMSE receivers still model residual self-interference (RSI) as additive Gaussian noise [46], an assumption that overlooks the colored and partially deterministic structure of RSI in full-duplex systems.

Table 2.2: Comparison of detection algorithms for full-duplex PNC systems

Algorithm	Complexity	Practical Limitations
Zero-Forcing (ZF)[45]	$\mathcal{O}(N^3)$	Noise enhancement
LMMSE[45]	$\mathcal{O}(N^3)$	channel-estimation error
Maximum Likelihood (ML)[47]	$\mathcal{O}(M^N)$	Computationally infeasible
Sphere Decoding (SD)[47]	$\mathcal{O}(N^3)$ (avg.)	Complexity varies

Addressing residual self-interference requires adaptive filtering techniques that can track the time-varying nature of the interference channel. Recursive Least Squares (RLS) filtering offers fast convergence, typically achieving steady-state performance within 10-20 symbols, but at the cost of $\mathcal{O}(N^2)$ complexity per symbol. The update equation for RLS is given by:

$$\mathbf{w}_n = \mathbf{w}_{n-1} + \mathbf{k}_n e_n^* \tag{2.7}$$

where \mathbf{k}_n is the Kalman gain vector and e_n is the prediction error. In contrast, the Least Mean Squares (LMS) algorithm offers lower complexity at $\mathcal{O}(N)$ per symbol but requires 100-200 symbols for convergence:

$$\mathbf{w}_n = \mathbf{w}_{n-1} + \mu e_n^* \mathbf{x}_n \tag{2.8}$$

where μ is the step size parameter that controls the trade-off between convergence speed and steady-state error.

The non-Gaussian nature of interference in full-duplex PNC systems has motivated exploration of advanced statistical signal processing techniques. Kalman filtering provides optimal tracking for time-varying channels when accurate statistical models are available. For scenarios with impulsive noise or non-linear interference, particle filtering and robust statistics offer improved performance at the cost of increased computational complexity.

The limitations of model-based approaches in capturing the full complexity of real-world interference patterns have sparked interest in data-driven methods. Deep learning techniques, which can learn complex nonlinear mappings from training data, show promise for handling the intricate interference patterns in full-duplex PNC systems. However, their integration must consider the constraints of practical communication systems, including real-time processing requirements and the need for reliable performance across varying channel conditions.

2.5 3GPP 5G New Radio

The practical implementation of full-duplex Physical-Layer Network Coding must align with established communication standards to ensure compatibility and facilitate deployment. The 3GPP 5G New Radio (NR) specification provides a flexible and robust framework that [48, 49, 50]. can accommodate advanced transmission techniques while maintaining backward compatibility and supporting diverse use cases. Figure 2.3 highlights the downlink fixed reference channel (DL-FRC) inside the NR physical-layer "toolbox."

At the heart of 5G NR physical layer lies Orthogonal Frequency Division Multiplexing (OFDM), chosen for its robustness against multipath fading and its flexibility in resource allocation. The OFDM signal can be expressed as:

$$s(t) = \sum_{k=0}^{N-1} X_k e^{j2\pi f_k t}, \quad f_k = \frac{k}{T_{\text{sym}}}$$
 (2.9)

where X_k represents the complex symbol on the k-th subcarrier and T_{sym} is the OFDM symbol duration. The orthogonality between subcarriers transforms the frequency-selective fading channel into multiple parallel flat-fading subchannels, significantly simplifying equalization.

The inclusion of a cyclic prefix (CP) is crucial for maintaining orthogonality in multipath environments. By prepending a copy of the last portion of each OFDM symbol, the CP absorbs inter-symbol interference when its duration exceeds the maximum channel delay spread. 5G NR defines two CP options: normal CP of 4.7 microseconds for typical scenarios and extended CP of 16.7 microseconds for environments with severe delay spread. This guard interval transforms the linear convolution with the channel into

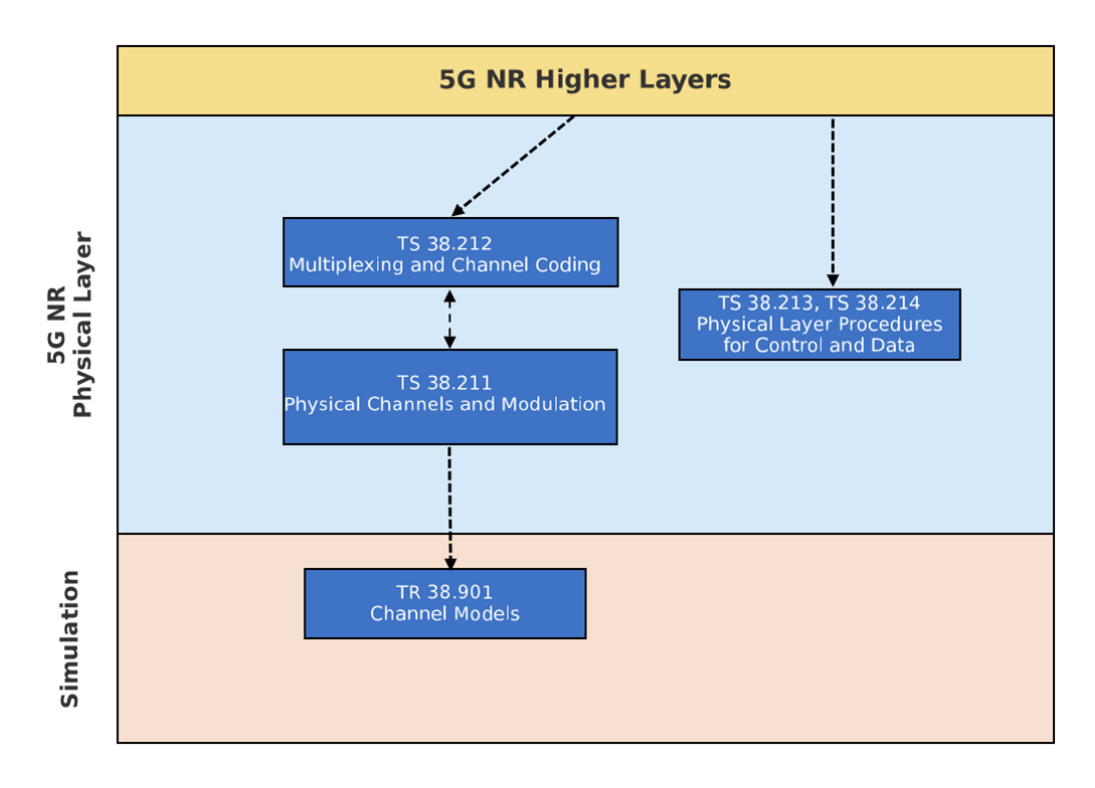


Figure 2.3: 5G NR Physical Layer Specification Structure [2]

circular convolution, enabling simple frequency-domain equalization.

5G NR introduces a scalable numerology framework to support diverse deployment scenarios and use cases. The subcarrier spacing can be configured as $\Delta f = 2^{\mu} \times 15$ kHz, where $\mu \in \{0,1,2,3,4\}$. Lower subcarrier spacings (15 kHz, 30 kHz) suit sub-6 GHz deployments with larger cell sizes, while higher spacings (60 kHz, 120 kHz) address millimeter-wave scenarios with reduced delay spread but increased Doppler spread. This flexibility allows optimization of the physical layer parameters based on the specific propagation environment and service requirements.

Channel coding in 5G NR employs Low-Density Parity-Check (LDPC) codes for data channels, chosen for their near-capacity performance and amenability to parallel decoding architectures. The LDPC codes use a quasicyclic structure that enables efficient hardware implementation while supporting a wide range of code rates and block sizes. For small block sizes, 5G NR employs polar codes, which achieve capacity for binary-input discrete memoryless channels. Error detection relies on Cyclic Redundancy Check

(CRC) codes, with the CRC-24 polynomial:

$$G(x) = x^{24} + x^{23} + x^{18} + x^{17} + x^{14} + x^{11} + x^{10} + x^{7} + x^{6} + x^{5} + x^{4} + x^{3} + x + 1$$
 (2.10)

The modulation schemes in 5G NR range from QPSK for robust communication in poor channel conditions to 256-QAM for maximum spectral efficiency in high SNR scenarios. The Modulation and Coding Scheme (MCS) [51] index jointly specifies the modulation order and code rate, enabling fine-grained link adaptation. This adaptive modulation and coding framework is particularly relevant for PNC systems, where the effective SNR depends on the combined power from multiple transmitters and the residual interference level.

The frame structure of 5G NR provides the temporal organization for transmission. Each radio frame spans 10 milliseconds and contains 10 subframes of 1 millisecond each. Depending on the numerology, each subframe contains 2^{μ} slots, with each slot typically containing 14 OFDM symbols. This hierarchical structure supports flexible scheduling while maintaining timing relationships necessary for feedback and hybrid automatic repeat request (HARQ) operations.

The integration of full-duplex PNC within the 5G NR framework requires careful consideration of several factors. The reference signal structure must be extended to support channel estimation for superimposed signals while accounting for self-interference. The scheduling algorithms need modification to coordinate simultaneous transmissions from multiple nodes while managing interference levels. Additionally, the HARQ mechanisms must be adapted to handle network-coded packets where traditional acknowledgment schemes may not directly apply.

While 5G NR provides a robust foundation for advanced physical layer techniques, the complexity of full-duplex PNC systems often exceeds what traditional signal processing algorithms can efficiently handle. The non-linear nature of residual self-interference, the time-varying channel conditions, and the need for joint processing of multiple signal components create an ideal application scenario for artificial intelligence techniques.

2.6 Deep Learning Architectures for Physical Layer Processing

The integration of deep learning into physical layer processing represents a paradigm shift from model-based to data-driven approaches. Traditional communication systems rely on mathematical models that capture idealized channel behaviors and interference patterns. However, real-world wireless environments exhibit complexities that often defy accurate analytical modelling, including non-linear hardware impairments, non-stationary interference, and intricate propagation phenomena. Deep learning offers the potential to learn these complex relationships directly from data, providing adaptive solutions that can outperform traditional algorithms in challenging scenarios.

The application of neural networks to physical layer problems requires careful consideration of the unique constraints and requirements of communication systems. Unlike many machine learning applications where occasional errors may be tolerable, communication systems demand consistent reliability and predictable performance. Real-time processing requirements impose strict latency constraints, while the need for generalization across diverse channel conditions challenges the typical assumptions of stationary data distributions.

The U-Net architecture [3] (see Figure 2.4) has emerged as particularly well-suited for signal-processing tasks in communication systems. Originally developed for biomedical image segmentation, U-Net's encoder-decoder structure with skip connections naturally aligns with the signal separation and reconstruction problems encountered in full-duplex PNC. The encoder path progressively extracts features at multiple scales, while the decoder path reconstructs the desired signals. The skip connections preserve fine-grained information that might otherwise be lost in the encoding process:

$$\mathcal{F}(x) = \mathcal{D}(\mathcal{E}(x)) + \mathcal{S}(x) \tag{2.11}$$

where \mathcal{E} represents the encoder, \mathcal{D} the decoder, and \mathcal{S} the skip connections. For PNC applications, U-Net can be adapted to separate superimposed signals while suppressing self-interference. The network learns to exploit subtle differences in the statistical properties of desired signals versus inter-

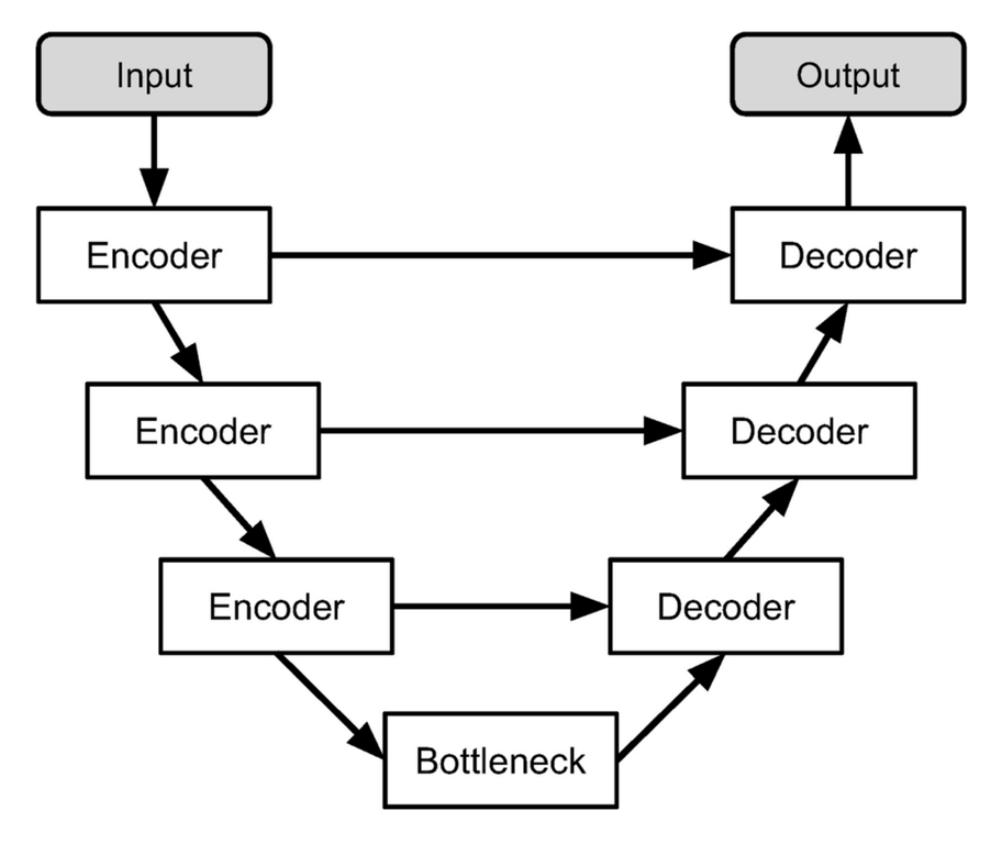


Figure 2.4: U-Net Architecture for Encoder-Decoder Networks [3]

ference, potentially capturing relationships that are difficult to model analytically. The multi-scale processing inherent in U-Net's architecture allows it to handle both narrowband and wideband interference components simultaneously.

Attention mechanisms [52] provide another powerful tool for physical layer processing. By learning to focus on relevant portions of the input signal while suppressing interference-dominated regions, attention modules can significantly improve detection performance. The attention mechanism can be formulated as:

$$\mathbf{y} = \sigma(f(\mathbf{x})) \otimes \mathbf{x} \tag{2.12}$$

where σ is the sigmoid activation function, f represents a learned transformation, and \otimes denotes element-wise multiplication. Channel attention learns the importance of different frequency components, naturally adapting to frequency-selective fading and interference. Spatial attention, applied in the time domain, can identify and emphasize clean signal segments while

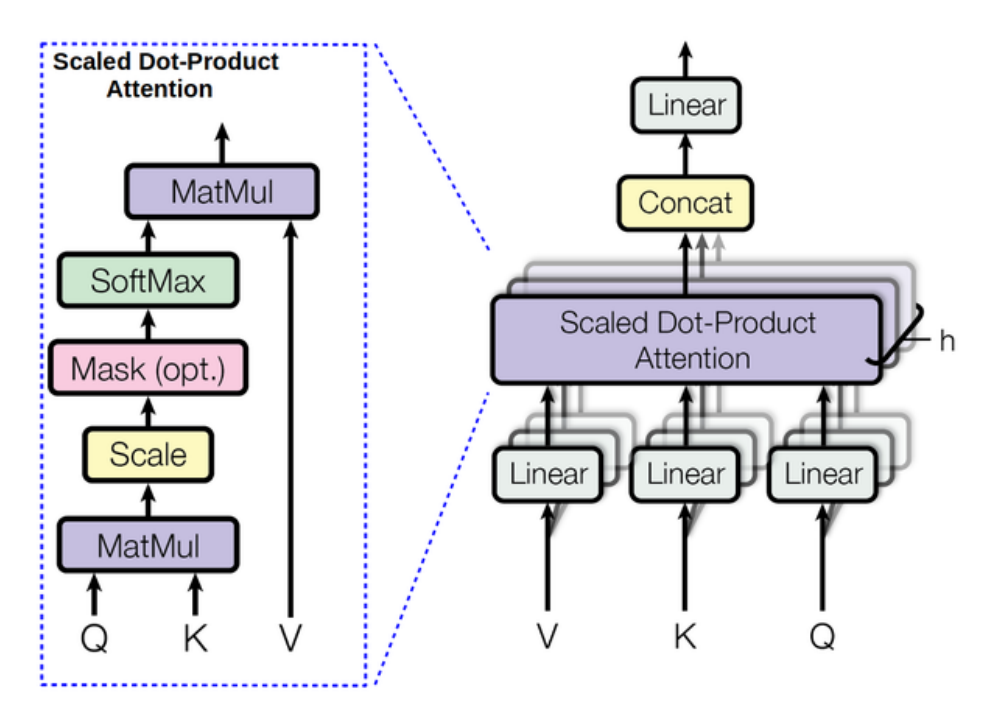


Figure 2.5: Multi-Head Self-Attention Mechanism

de-emphasizing corrupted portions.

Residual learning, popularized by ResNet [53] architectures, addresses the challenge of training deep networks for physical layer applications. By learning residual mappings rather than direct transformations, these networks can more easily capture the subtle modifications needed for tasks like interference cancellation:

$$\mathbf{y} = \mathcal{F}(\mathbf{x}, \mathbf{W}) + \mathbf{x} \tag{2.13}$$

The residual connection (see Figure 2.6) ensures that the network can preserve the original signal structure while learning to remove interference components. This approach is particularly valuable in communication systems where the desired signal often constitutes the dominant component, and the network primarily needs to learn corrections.

Training deep learning models for physical layer applications presents unique challenges. The generation of representative training data requires careful consideration of channel models, interference patterns, and hardware impairments. Synthetic data generation using statistical channel models provides controlled conditions for initial training, but may not capture all real-

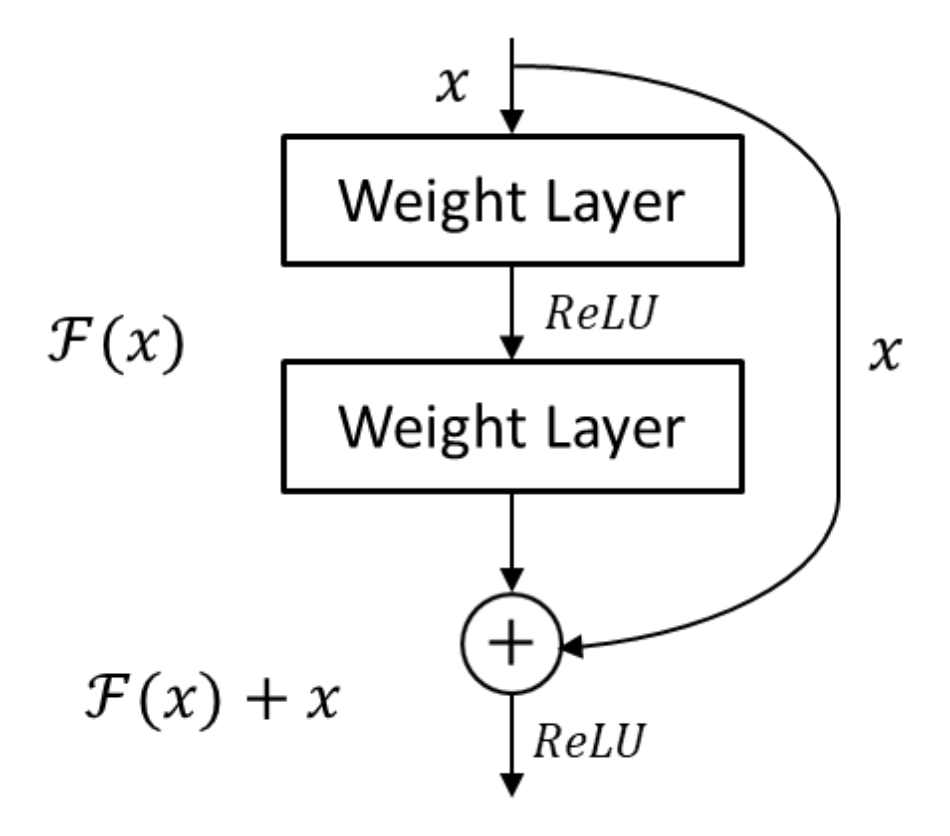


Figure 2.6: Residual Block in a ResNet Architecture

world complexities. Hardware-in-the-loop training, where actual RF signals are captured and processed, offers greater realism but at significantly higher cost and complexity.

The choice of loss function critically impacts the learned behavior. While mean squared error provides a natural choice for signal reconstruction tasks, it may not directly optimize communication performance metrics like bit error rate. Custom loss functions that incorporate domain knowledge, such as constellation constraints or error vector magnitude, can guide the network toward solutions that maintain compatibility with existing systems while improving performance.

2.7 Summary

This chapter has established a comprehensive theoretical foundation for AI-enhanced full-duplex Physical-Layer Network Coding systems through the systematic presentation of six interconnected components. The progression from architectural concepts to implementation details reflects both the historical evolution of these technologies and the logical dependencies between system components.

The Two-Way Relay Channel provides the fundamental architectural framework, demonstrating how bidirectional communication efficiency can be doubled through coordinated transmission scheduling. Physical-Layer Network Coding builds upon this foundation by transforming the challenge of simultaneous transmissions from a source of interference into an opportunity for computation over the air. The theoretical elegance of these concepts, however, confronts practical limitations in real-world implementations.

Full-duplex communication emerges as a critical enabling technology, promising to further double spectral efficiency by eliminating the half-duplex constraint. Yet this advancement comes at the cost of severe self-interference that must be mitigated through sophisticated multi-stage cancellation techniques. The residual self-interference that persists after cancellation fundamentally alters the signal detection problem, requiring advanced algorithms capable of jointly processing desired signals while suppressing structured interference.

The 3GPP 5G New Radio standard provides the practical framework within which these advanced techniques must operate. Its flexible numerology, robust channel coding, and adaptive modulation schemes offer the foundation needed for reliable PNC operation. However, the complexity of optimizing these systems under the challenging conditions of full-duplex operation with residual interference exceeds the capabilities of traditional model-based approaches.

Deep learning architectures offer a promising path forward, providing data-driven solutions that can adapt to the complex, non-linear, and time-varying nature of real-world wireless channels. The surveyed architectures—U-Net for signal separation, attention mechanisms for selective processing, residual learning for deep networks, and CNNs for time-frequency processing—each address specific aspects of the physical layer processing challenge.

The synthesis of these components creates a system where each element addresses specific technical challenges while contributing to overall performance. The architectural innovations of TWRC and PNC establish the theoretical performance bounds. Full-duplex operation and advanced signal detection push toward these bounds while confronting practical constraints. The 5G NR framework ensures compatibility with existing infrastructure and devices. Finally, deep learning provides the adaptive intelligence needed to handle real-world complexities that defy analytical modeling.

This foundation sets the stage for the development of an AI-enhanced receiver architecture specifically designed for full-duplex PNC systems, which we present in Chapter 3. The challenges identified—from residual self-interference suppression to joint signal detection in superimposed transmissions—directly inform the design choices and optimization strategies for our proposed system.

Chapter 3

Proposed REST-UNet Framework for CPNC in Full-Duplex Systems

This chapter presents our unified framework that addresses both challenges through the synergistic integration of Concurrent Physical-Layer Network Coding (CPNC) and the Residual-and-Attention U-Net (REST-UNet). The CPNC protocol extends PNC to support arbitrary bijective Modulation constellations while leveraging full-duplex operation with carefully designed processing delays. REST-UNet provides learning-based interference suppression that captures the complex, time-varying nature of residual self-interference. Together, these innovations enable practical deployment of full-duplex PNC in 5G New Radio systems while maintaining compatibility with existing standards.

3.1 System Model

3.1.1 Network Model and Protocol Design

Network Model — Fig. 3.1. We abstract the system as a full-duplex two-way relay channel (FD-TWRC) with two user nodes A, B and a relay R. All radios share one carrier and transmit *every* OFDM symbol, so there are no idle slots or extra bands. The model follows three minimalist

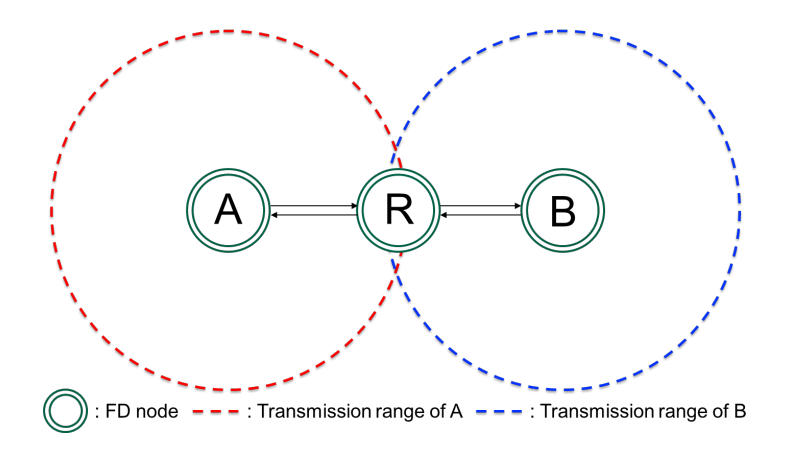


Figure 3.1: Full-duplex TWRC topology

rules that expose the essential challenges while avoiding implementation-specific details:

- R1. **Single hop, symmetric exchange** users communicate exclusively through the relay, forcing all traffic through a single bottleneck.
- R2. Simultaneous Tx/Rx every node transmits and receives on the same sub-carriers each symbol, creating residual self-interference (RSI) and mutual user interference (MUI).
- R3. Network-coded forwarding the relay decodes only the XOR symbol $x_A \oplus x_B$ and broadcasts it in the next symbol, collapsing the classical four-slot TWRC into a one-slot pipeline.

These rules capture short-range deployments with tight spectrum budgets (e.g., factory cells, XR pods, ad-hoc relays) without locking the analysis to one specific use case. They maximise spectral efficiency but also surface the dominant pain-points—strong RSI at R, overlapping user signals, and strict one-symbol processing latency—that the proposed protocol must overcome.

Bespoke OFDM protocol — Fig. 3.2 Building on 5G-NR numerology, we introduce three departures from stock NR processing to tame RSI and MUI while preserving one-slot latency:

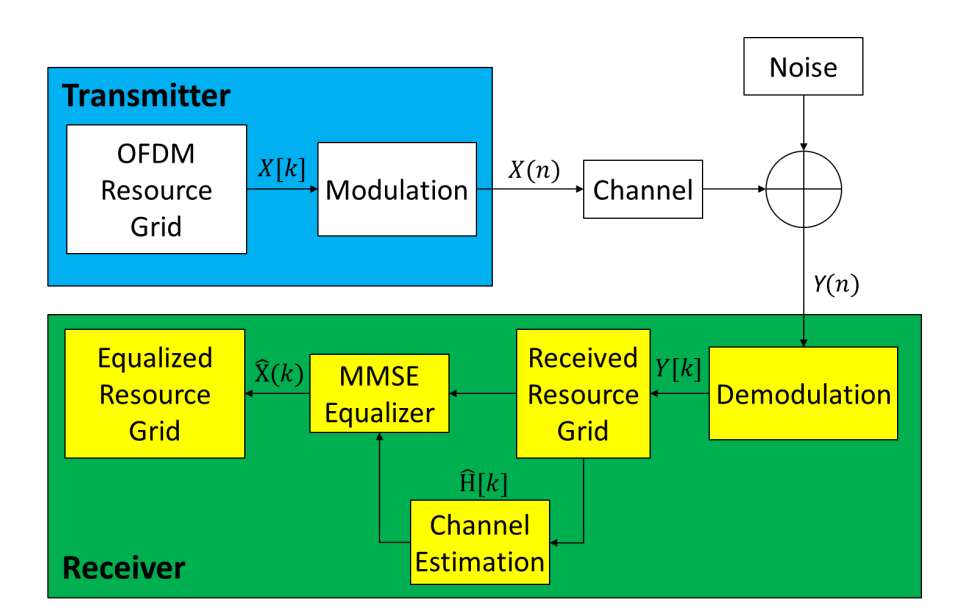


Figure 3.2: OFDM resource-grid processing

- 1) **PNC-tailored pilot lattice**: pilots of A, B, and R are interleaved with a fixed phase offset, enabling a *single* least-squares fit for \mathbf{H}_{AR} , \mathbf{H}_{BR} , \mathbf{H}_{RR} without guard symbols.
- 2) **RSI-aware MMSE equaliser**: each receiver augments the covariance matrix to treat \mathbf{H}_{RR} as coloured interference. The resulting inverse updates per symbol via two rank-one corrections—quadratic rather than cubic complexity.
- 3) **Look-ahead network coding**: the relay converts equalised streams into $x_A \oplus x_B$ on the fly and transmits the result after a fixed delay of δ , thereby eliminating the need for buffering and aligning with NR slot timing.

Positioning with respect to prior art. Classical TWRC protocols rely on time-division, forfeiting half the spectrum; modern full-duplex relays depend on heavy analogue cancellation. Our design instead

- shifts cancellation to digital RSI suppression via the equaliser hardware-agnostic and software-upgradable;
- embeds **physical-layer network coding** directly in the NR resource grid—no MAC redesign, no HARQ overhaul;

• reuses standard NR FFT and numerology—only the pilot pattern, equaliser weights, and XOR lookup tables change.

In short, Fig. 3.1 defines what the network must accomplish—continuous full-duplex exchange in a single hop—while Fig. 3.2 articulates how an NR-compatible physical layer achieves it through a tailored pilot lattice, RSI-aware equalisation, and one-symbol look-ahead network coding.

3.1.2 Channel Models and Propagation Scenarios

Our framework supports multiple channel models to capture diverse propagation environments encountered in practical deployments. Each model is designed to represent specific deployment scenarios rather than fixed parameter sets.

Additive White Gaussian Noise (AWGN) Channel

The AWGN channel serves as a theoretical baseline, representing ideal propagation conditions with minimal multipath effects:

$$h(t) = 1, \quad \forall t \tag{3.1}$$

This model is primarily used for algorithm validation, theoretical performance bounds derivation, and laboratory testing scenarios including cable connections and satellite communication links with minimal scattering.

Static Rayleigh Fading Channel

The Rayleigh fading model captures non-line-of-sight (NLOS) propagation typical in dense urban environments where multiple scattering paths exist without a dominant line-of-sight component. The channel impulse response consists of multiple independent taps:

$$h(t) = \sum_{l=0}^{L-1} h_l \delta(t - \tau_l)$$
 (3.2)

where $h_l \sim \mathcal{CN}(0, \sigma_l^2)$ are complex Gaussian random variables, and the power delay profile follows an exponential decay pattern.

This model accurately represents:

- Dense urban deployments with no dominant path
- Indoor propagation with multiple walls and obstacles
- Mobile scenarios in city centers
- Small cell deployments in crowded areas

Static Rician Fading Channel

The Rician fading model incorporates a line-of-sight (LOS) component alongside scattered paths, characterized by the K-factor:

$$K = \frac{\text{Power in LOS component}}{\text{Power in scattered components}}$$
(3.3)

The channel impulse response becomes:

$$h(t) = \sqrt{\frac{K}{K+1}}\delta(t) + \sqrt{\frac{1}{K+1}} \sum_{l=0}^{L-1} h_l \delta(t - \tau_l)$$
 (3.4)

Typical deployment scenarios include suburban areas with partial LOS, rural deployments with strong LOS components, indoor corridors with guided propagation, and millimeter-wave links with highly directional characteristics.

ITU Indoor Channel Models

The International Telecommunication Union (ITU) has standardized indoor channel models based on extensive measurements. We implement both Indoor-A and Indoor-B models representing small office and large office environments respectively.

These models are specifically designed for WiFi and small cell deployments, performance evaluation for indoor positioning systems, enterprise wireless network planning, and IoT device connectivity in buildings.

Time-Varying Rician Channel

Mobile scenarios require time-varying channel models that capture Doppler effects caused by user mobility. The channel coefficients evolve according to:

$$h_l(t) = h_l(0) \exp(j2\pi f_{D,l} t \cos(\theta_l))$$
(3.5)

where $f_{D,l}$ is the Doppler frequency for tap l, and θ_l is the angle of arrival.

Key mobility scenarios include pedestrian users, vehicular deployments, high-speed rail communication, and drone/UAV aerial network coverage.

3.1.3 Self-Interference Model and Characterization

The self-interference in full-duplex systems represents one of the most challenging aspects of practical implementation. Despite significant advances in analog cancellation techniques, residual self-interference typically remains 20-40 dB above the noise floor, fundamentally different from simple additive noise in both structure and impact.

Components of Residual Self-Interference

The residual self-interference after analog cancellation can be decomposed into several components:

$$y_{\rm SI}(t) = y_{\rm linear}(t) + y_{\rm nonlinear}(t) + y_{\rm phase}(t) + y_{\rm IO}(t)$$
(3.6)

Linear Component arises from imperfect channel estimation and finite cancellation depth:

$$y_{\text{linear}}(t) = \alpha h_{RR}(t) * s_R(t - \delta)$$
(3.7)

where α represents the cancellation factor achieved by analog techniques.

Nonlinear Component results from power amplifier compression and mixer nonlinearities:

$$y_{\text{nonlinear}}(t) = \sum_{k=2}^{K} \beta_k |s_R(t-\delta)|^{k-1} s_R(t-\delta)$$
(3.8)

where β_k are the nonlinearity coefficients.

Phase Noise Component originates from oscillator imperfections:

$$y_{\text{phase}}(t) = s_R(t - \delta) \exp(j\phi(t))$$
(3.9)

where $\phi(t)$ is a Wiener process.

IQ Imbalance Component stems from imperfect quadrature mixing:

$$y_{IQ}(t) = g_I s_{R,I}(t - \delta) + j g_Q s_{R,Q}(t - \delta) \exp(j\theta_{IQ})$$
(3.10)

The aggregate residual self-interference exhibits complex statistical properties that deviate from Gaussian assumptions, including log-normal power distribution, stronger frequency selectivity than desired channels, and temporal correlation on multiple time scales from fast temperature fluctuations to slow component aging effects.

3.2 Concurrent Physical-Layer Network Coding (CPNC)

3.2.1 CPNC Architecture and Protocol Design

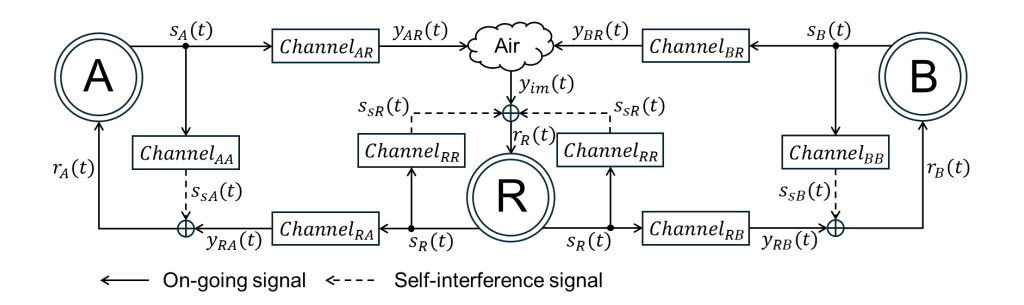


Figure 3.3: CPNC Diagram with Full-Duplex Relay and Self-Interference Paths

Concurrent Physical-Layer Network Coding (CPNC) represents a fundamental advancement in network coding theory, extending the elegant principles of PNC to practical full-duplex systems with complex-valued modulations. Figure 3.3 illustrates the complete CPNC framework, highlighting the key innovation of processing delay δ integration.

In this framework, nodes A and B transmit their respective signals $s_A(t)$ and $s_B(t)$ simultaneously to a full-duplex relay node R. The relay receives a superimposed signal $r_R(t)$ through the air channel, which includes contributions from both nodes and its own transmission due to full-duplex operation:

$$r_R(t) = y_{AR}(t) + y_{BR}(t) + S_{sR}(t),$$

where $y_{AR}(t)$ and $y_{BR}(t)$ represent the signals from A and B through channels Channel_{AR} and Channel_{BR}, respectively, and $y_{RR}(t)$ is the self-interference signal caused by the relay's own transmission $s_R(t)$ via Channel_{RR}.

To mitigate this self-interference, the relay employs a cancellation mechanism, subtracting an estimate $s_S(t)$ of its own transmitted signal from r(t) to obtain $r_R(t) = r(t) - \hat{S_{sR}}$, which can be estimated from the transmitted signal of nodes R. The relay then forwards a new signal $s_R(t)$ after a fixed processing delay δ through channels Channel_{RA} and Channel_{RB} to both destinations.

At the receiver side, nodes A and B also suffer from self-interference due to their own transmissions, denoted by $s_S(t)$ via Channel_{AA} and Channel_{BB}, respectively. Each node performs local cancellation to retrieve the intended signal from the other node:

$$r_A(t) = y_{RA}(t) - \hat{S}_{sA}, \quad r_B(t) = y_{RB}(t) - \hat{S}_{sB},$$

enabling successful decoding of the desired message by leveraging prior knowledge of the local transmission.

Solid arrows in Figure 3.3 indicate ongoing signal transmissions, while dashed arrows represent self-interference loops at each node. The entire system illustrates a fully concurrent, self-interference—aware network coding protocol enabled by the integration of a short processing delay δ at the relay.

The CPNC protocol operates through carefully orchestrated phases that overlap in time. The key innovation lies in maintaining the algebraic structure required for network coding while proactively inserting a controlled processing delay, δ , at the relay. This intentional gap transforms δ into a system feature that enables:

- 1. **Pipelined Throughput:** Reception of the next data block, SI cancellation and XOR mapping of the current block, and transmission of the previous block all overlap, maximizing relay utilization.
- 2. Interference-Window Control: By tuning δ , the relay can steer residual self-interference into predefined guard intervals (e.g., CP or protocol-defined idle slots), simplifying digital cancellation.
- 3. Adaptive Performance Tuning: The relay dynamically adjusts δ in response to channel conditions or SI levels—trading off between lower end-to-end latency (small δ) and higher decoding robustness (large δ).

- 4. **Load-Smoothing:** A fixed δ spreads computational tasks evenly across each OFDM frame, reducing instantaneous processing peaks and improving hardware efficiency.
- 5. **Protocol Flexibility:** The intentional gap δ can carry auxiliary control or training symbols, facilitating MAC-layer scheduling, link monitoring, or secure handshakes without disrupting the main data flow.

Data Protocol Design: The relay processing follows a pipelined architecture where reception, processing, and transmission occur simultaneously on different data blocks. This approach maintains continuous bidirectional communication while ensuring each operation has adequate time to complete. The protocol timing is designed to ensure users receive the relay's broadcast during their reception phases, avoiding conflicts with their own transmission periods.

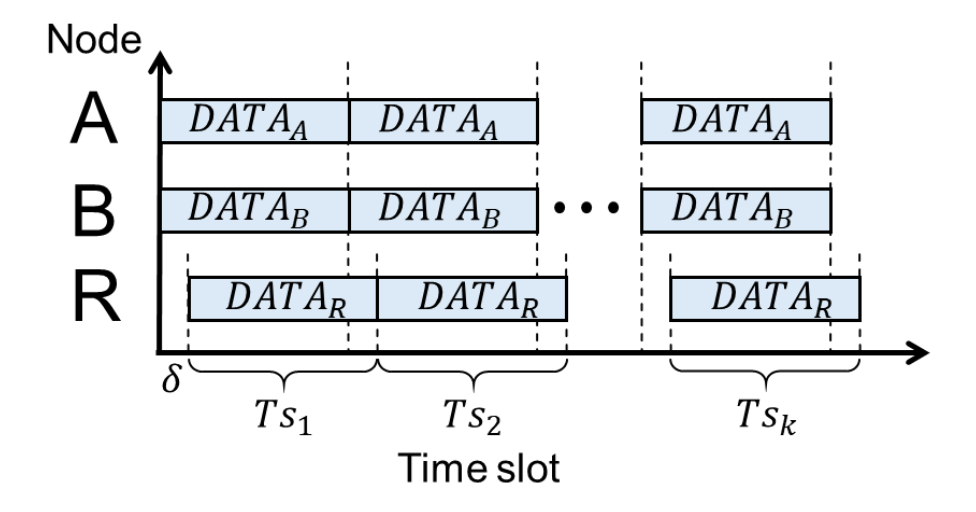


Figure 3.4: CPNC protocol diagram with processing delay δ at the relay

3.2.2 Constellation-Mapping-Aided CPNC Detection: Fundamental Limitations

The Bijective Mapping Requirement

Physical-layer Network Coding (PNC) fundamentally relies on the ability of the relay node to uniquely determine the XOR of transmitted informa-

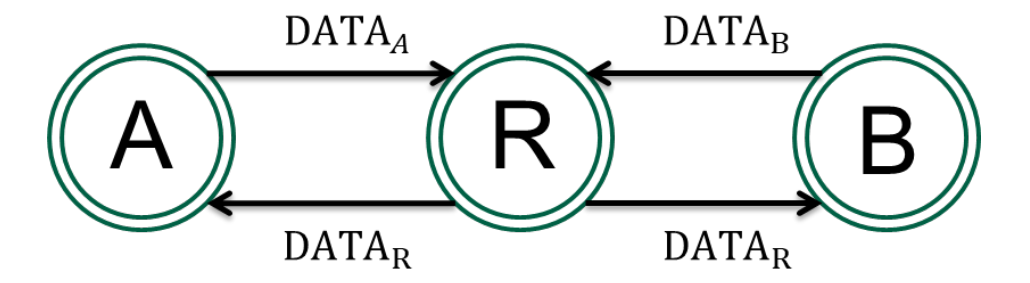


Figure 3.5: System architecture of the CPNC protocol

tion from the electromagnetic superposition of received signals. For this to be possible, the mapping from symbol pairs to their superposition must be *bijective* (one-to-one and onto). This mathematical requirement places severe constraints on the types of modulation schemes that can support PNC operation.

The Core Challenge: When two nodes A and B transmit symbols s_A and s_B simultaneously, the relay receives $r = s_A + s_B + n$ where n represents channel noise. For successful network coding, the relay must be able to uniquely determine $s_A \oplus s_B$ from the received signal r. This requires that different symbol pairs (s_A, s_B) and (s'_A, s'_B) that produce different XOR results must yield different superposition results, i.e.:

$$s_A \oplus s_B \neq s_A' \oplus s_B' \Rightarrow s_A + s_B \neq s_A' + s_B' \tag{3.11}$$

Mathematical Analysis of Bijective Requirements

Definition 1 (PNC-Compatible Constellation). A constellation C is PNC-compatible if and only if the mapping $\phi : C \times C \to \mathbb{C}$ defined by $\phi(s_A, s_B) = s_A + s_B$ satisfies:

$$\forall (s_A, s_B), (s'_A, s'_B) \in \mathcal{C}^2 : s_A \oplus s_B = s'_A \oplus s'_B \Leftrightarrow s_A + s_B = s'_A + s'_B \quad (3.12)$$

This condition is extremely restrictive. For most practical modulation schemes, multiple symbol pairs can produce identical superposition results while having different XOR values, violating the bijective requirement.

Illustrative Example: Consider 16-QAM with your specific case:

Case 1:
$$s_A = 1 + 3j$$
, $s_B = 3 + 1j \implies s_A + s_B = 4 + 4j$ (3.13)

Case 2:
$$s_A = 1 + 1j$$
, $s_B = 3 + 3j \implies s_A + s_B = 4 + 4j$ (3.14)

If these symbol pairs correspond to different information bits, then $s_A \oplus s_B \neq s_A' \oplus s_B'$, but $s_A + s_B = s_A' + s_B'$, violating the PNC-compatibility condition.

Classification of Modulation Schemes

Based on the bijective mapping requirement, we classify common modulation schemes according to their PNC compatibility:

Table 3.1: PNC Compatibility of Common Modulation Schemes

Modulation	PNC Compatible	Mapping Type	
BPSK	√	Bijective	
QPSK	✓	Bijective	
8-PSK	×	Non-bijective	
16-QAM	×	Non-bijective	
64-QAM	×	Non-bijective	
256-QAM	×	Non-bijective	
PAM-2	✓	Bijective	
PAM-4	×	Non-bijective	
PAM-M (M > 4)	×	Non-bijective	
FSK-2	√	Bijective	
FSK-M (M > 2)	×	Non-bijective	

Theoretical Limitations

Fundamental Constraint For an M-ary constellation with $M=2^k$, there are $M^2=2^{2k}$ possible symbol pairs, but only 2^k possible XOR results. For PNC compatibility, each XOR result must correspond to a unique superposition value. However, the number of possible superposition values is generally much smaller than 2^{2k} , making bijective mapping impossible for M>4.

Ambiguity Quantification The degree of ambiguity can be quantified by the *collision ratio*:

$$\rho = \frac{\text{Number of distinct superposition values}}{2^{2k}} \tag{3.15}$$

For PNC compatibility, we require $\rho = 2^{-k}$. However, for most practical constellations:

16-QAM:
$$\rho \approx 0.0625 \ll 0.25 \text{ (required)}$$
 (3.16)

64-QAM:
$$\rho \approx 0.016 \ll 0.125 \text{ (required)}$$
 (3.17)

Implications for System Design

Practical Consequences:

- 1. Limited Spectral Efficiency: PNC is fundamentally restricted to low-order modulations (BPSK, QPSK), severely limiting spectral efficiency compared to modern high-order QAM systems.
- 2. **Performance Trade-offs:** The constraint to bijective modulations may result in lower data rates compared to conventional point-to-point or traditional relaying systems using high-order modulations.
- 3. System Complexity: Any attempt to extend PNC to higher-order modulations requires complex pre-processing, special constellation designs, or tolerance for decoding errors, significantly increasing implementation complexity.

Alternative Approaches: Given these fundamental limitations, practical systems must consider:

- **Hybrid schemes:** Use PNC for certain time slots/subcarriers and conventional relaying for others
- Adaptive modulation: Switch between PNC-compatible and highorder modulations based on channel conditions
- Multi-level coding: Apply PNC only to specific bit layers in hierarchical modulation schemes
- **Probabilistic decoding:** Accept some decoding errors in exchange for higher spectral efficiency

Conclusion

The fundamental requirement for bijective mapping severely constrains the applicability of PNC to modern communication systems. While PNC offers significant advantages for simple modulations like BPSK and QPSK, the mathematical impossibility of maintaining bijective mapping for higher-order constellations presents an insurmountable barrier for direct application to spectrally efficient QAM systems.

This analysis reveals that **constellation-mapping-aided CPNC detection is fundamentally limited to low-order, bijective modulations**, and any claims of extending PNC to arbitrary high-order QAM constellations must be approached with extreme caution. The pursuit of PNC-compatible high-order modulations remains an open and challenging research problem with no known general solution. Therefore, the CPNC scheme shown in this thesis currently focuses on low-order modulations such as BPSK and QPSK. In our experiments, we use QPSK to verify the performance of the scheme and leave the support of higher-order modulations for future research

3.2.3 Orthogonal Pilot Design and Channel Estimation for PNC

Adaptive Orthogonal Pilot Design. Conventional pilot patterns—optimised for one user at a time—fail in PNC, where two (or more) users transmit concurrently. We therefore generate pilots from a *Hadamard matrix*, yielding a bank of mutually orthogonal sequences whose size adapts to the number of pilot tones. Let $\mathcal{I}_{\text{pilot}}$ denote the set of pilot-bearing sub-carriers; its cardinality is num_pilot = $|\mathcal{I}_{\text{pilot}}|$. Choose the smallest power of two no smaller than num_pilot, $M = 2^{\lceil \log_2(\text{num-pilot}) \rceil}$, and form the $M \times M$ Hadamard matrix \mathbf{H}_M . The first two rows trimmed to num_pilot elements serve as user-specific pilot sequences:

$$\mathbf{p}_A = \mathbf{H}_M(1, 1: \text{num_pilot}), \qquad \mathbf{p}_B = \mathbf{H}_M(2, 1: \text{num_pilot}), \tag{3.18}$$

guaranteeing $\mathbf{p}_A \mathbf{p}_B^{\mathsf{T}} = 0$ and leaving the remaining M-2 rows available for future users.

Pilot Power and Data Mask. Pilot amplitude A_p is chosen to meet a target mean-square-error (MSE) bound while limiting the peak-to-average-power

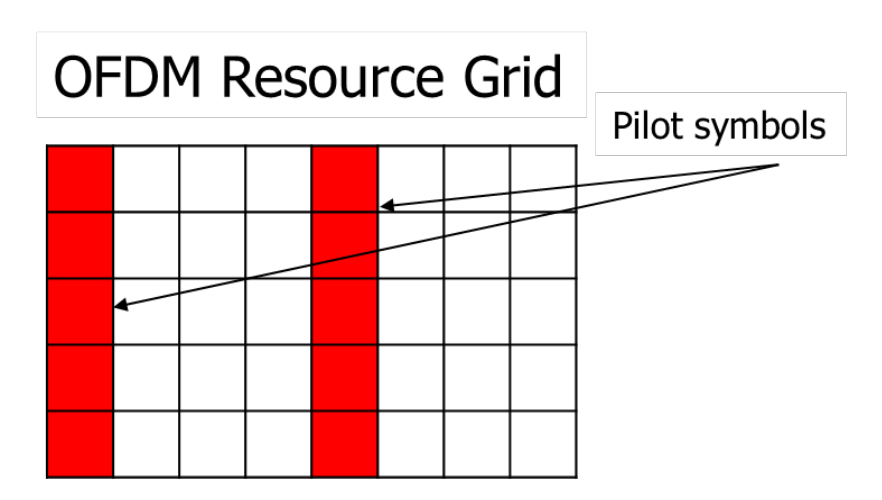


Figure 3.6: OFDM resource grid with pilot symbols

ratio (PAPR). A binary mask $\mathbf{M}_{\text{data}} \in \{0,1\}^{F \times S}$ flags data sub-carriers, ensuring pilots never collide with payload symbols.

Least-Squares Channel Estimation. Let y_{pilot} collect all received pilot samples on the indices $\mathcal{I}_{\text{pilot}}$ and define $\mathbf{P} = [\mathbf{p}_A^\mathsf{T} \ \mathbf{p}_B^\mathsf{T}]$. Because Hadamard rows are mutually orthogonal, the LS estimate boils down to scaled correlations:

$$\begin{bmatrix} \hat{h}_A \\ \hat{h}_B \end{bmatrix} = (\mathbf{P}^H \mathbf{P})^{-1} \mathbf{P}^H \mathbf{y}_{\text{pilot}}.$$
 (3.19)

Algorithm 1 Pilot Separation and LS Channel Estimation

Input: Received frequency grid Y, pilot index set \mathcal{I}_{pilot} , pilot amplitude A_p , pilot sequences $\mathbf{p}_A, \mathbf{p}_B$

Output: Estimated channels \hat{h}_A , \hat{h}_B ; separated pilot components $\hat{\mathbf{Y}}_A$, $\hat{\mathbf{Y}}_B$

- 1: Extract pilot samples: $\mathbf{y}_{pilot} \leftarrow \mathbf{Y}[:, \mathcal{I}_{pilot}]$
- 2: Scale pilot sequences: $\mathbf{P} \leftarrow \left[A_p \mathbf{p}_A^\mathsf{T} A_p \mathbf{p}_B^\mathsf{T} \right]$ 3: Solve LS problem $\left[\hat{h}_A, \hat{h}_B \right]^\mathsf{T} \leftarrow (\mathbf{P}^H \mathbf{P})^{-1} \mathbf{P}^H \mathbf{y}_{\text{pilot}}$
- 4: Reconstruct pilot components: $\hat{\mathbf{Y}}_A \leftarrow \hat{h}_A(A_p\mathbf{p}_A); \hat{\mathbf{Y}}_B \leftarrow \hat{h}_B(A_p\mathbf{p}_B)$ $\hat{h}_A, \hat{h}_B, \hat{\mathbf{Y}}_A, \hat{\mathbf{Y}}_B$

Network-Coded Equalisation. With \hat{h}_A, \hat{h}_B in hand, the relay bypasses per-user recovery and computes the XOR symbol directly:

$$\hat{x}_{\oplus} = \frac{y_{\text{rx}}}{\hat{h}_A + \hat{h}_B} \stackrel{\text{LUT}}{\longleftrightarrow} x_A \oplus x_B, \tag{3.20}$$

where a pre-computed XOR_LUT maps equalised constellation points to the network-coded alphabet. This "equalise-then-XOR" strategy trims complexity while preserving PNC throughput.

The Hadamard construction not only isolates two simultaneous users but also leaves room for additional orthogonal rows, enabling straightforward extension to multi-user PNC without redesigning the pilot framework.

3.2.4 Constellation-Mapping-Aided CPNC Detection

Signal Model For the f-th sub-carrier and the s-th OFDM symbol, the relay observes

$$y_{f,s} = h_{A,f,s} x_{A,f,s} + h_{B,f,s} x_{B,f,s} + n_{f,s}, \quad n_{f,s} \sim \mathcal{CN}(0, N_0),$$
 (3.21)

where $x_{A,f,s}, x_{B,f,s} \in \mathcal{C}$ are M-ary constellation symbols.

XOR Constellation Sets For each target XOR label $b \in \{0, 1\}^{\log_2 M}$,

$$S_{\boldsymbol{b}}(h_A, h_B) = \left\{ h_A c_i + h_B c_j \, \middle| \, c_i, c_j \in \mathcal{C}, b(c_i) \oplus b(c_j) = \boldsymbol{b} \right\}. \tag{3.22}$$

Decision Rule

$$\hat{\boldsymbol{b}}_{f,s} = \arg\min_{\boldsymbol{b}} \min_{\tilde{y} \in \mathcal{S}_{\boldsymbol{b}}(h_{A,f,s},h_{B,f,s})} \left| y_{f,s} - \tilde{y} \right|^2.$$
 (3.23)

Algorithm 2 Constellation-Mapping-Aided CPNC Detection

- 1: Initialize an empty grid $\hat{\mathbf{B}} \in \{-1, 0, 1\}^{F \times S \times \log_2 M}$. $f = 1 \to F$ $s = 1 \to S$ (f, s) is a data position
- 2: Compute the sets \mathcal{S}_b for all XOR labels **b**. each candidate $\tilde{y} \in \mathcal{S}_b$
- 3: Evaluate the distance $|y_{f,s} \tilde{y}|^2$.
- 4: Select $\hat{\boldsymbol{b}}_{f,s} = \arg\min_{\boldsymbol{b}} \min_{\tilde{y} \in \mathcal{S}_{\boldsymbol{b}}} |y_{f,s} \tilde{y}|^2$ and store it in $\hat{\mathbf{B}}[f, s, :]$.

Complexity & Overhead. For each data grid (f, s), the Constellation -Mapping-Aided CPNC detector forms all symbol pairs $(c_i, c_j) \in \mathcal{C}^2$ and groups them by XOR label, so the per-grid search spans at most M^2 candidates and incurs $\mathcal{O}(M^2)$ distance evaluations. Over the $N_d = F_{\text{data}}S_{\text{data}}$ active positions in one OFDM frame the total arithmetic cost is therefore $\mathcal{O}(N_dM^2)$, identical in order to a brute-force ML detector but with a smaller constant factor thanks to the XOR clustering. Memory use is negligible: the decision tensor $\hat{\mathbf{B}} \in \{-1,0,1\}^{F \times S \times \log_2 M}$ only requires a few hundred bits per frame, while the optional lookup table of all M^2 composite points fits easily in on-chip cache for typical low-order constellations. Consequently, detection remains real-time on a DSP/CPU without requiring GPU or FPGA acceleration.

3.3 REST - UNet Architecture for Noise -Interference Suppression

Conventional clean-sheet CPNC receivers cascade (i) a least—squares or MMSE pilot-based channel estimator, (ii) an adaptive self-interference cancellation (SIC) filter, (iii) frequency-domain equalisation, and (iv) an ML XOR detector. The strong coupling of these blocks makes the overall performance highly sensitive to modelling errors, non-linear power- amplifier distortion, and time-varying RF leakage. To overcome these limitations we introduce **REST-UNet**, a Residual – Attention – U-Net that jointly performs channel estimation, SIC, equalisation, and XOR detection in a single end-to-end learnable module.

3.3.1 System-Level Integration of REST-UNet

Figure 3.7 embeds REST-UNet in a 5G NR CPNC transceiver. During forward (blue arrows) and reverse (red arrows) propagation the network receives

- the **received OFDM grid** after cyclic-prefix removal and FFT;
- a **prior channel tensor** obtained from ray-tracing/pilot interpolation (H_{pilot}) ;

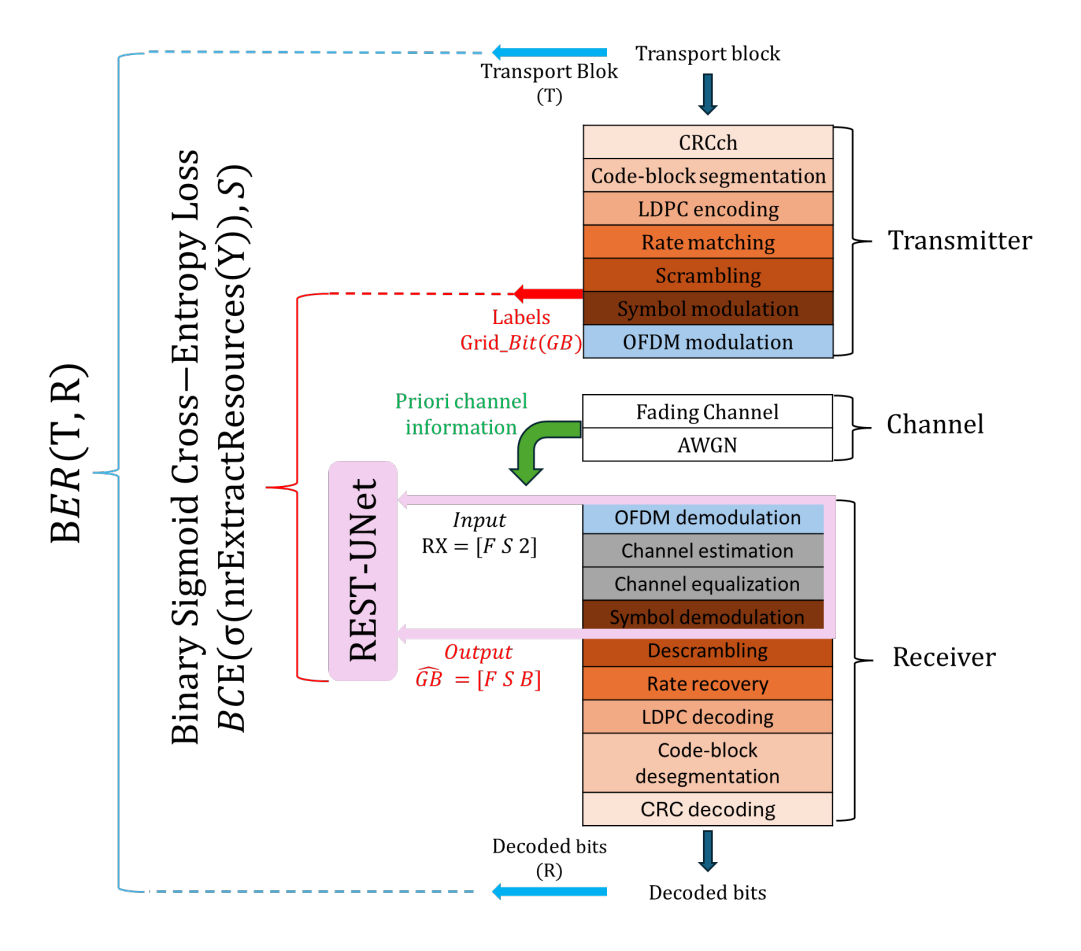


Figure 3.7: REST-UNet-based receiver framework in an OFDM system

• the ground-truth label cube GB $\in \{0,1\}^{F \times S \times B}$ generated at the symbol-modulation stage.

REST-UNet outputs a refined XOR-bit likelihood $\hat{\mathbf{GB}}$ that replaces the legacy chain of OFDM demod \rightarrow channel estimation \rightarrow equalisation \rightarrow symbol demodulation. The remaining descrambling, LDPC decoding and CRC check are left unchanged, ensuring standard-compliant operation.

3.3.2 REST-UNet Micro-Architecture

Figure 3.8 details the deep network itself. A four-level encoder—decoder backbone is augmented with the following modules:

ResBlocks Two consecutive Conv-BN-ReLU layers followed by a residual

shortcut, providing local feature refinement while mitigating vanishinggradient issues.

Self-Attention A channel-wise self-attention module is inserted at every scale to emphasize time–frequency (TF) bins rich in interference energy.

Cross-Attention A cross-attention block combines the prior channel map H_{pilot} with deep feature maps, explicitly guiding the decoder toward physically plausible reconstructions.

Upsampling/Downsampling Resolution changes are handled by strided convolutions for downsampling and transposed convolutions for upsampling; each downsampling step halves the TF resolution and doubles channel depth, while each upsampling step reverses this mapping.

The decoder terminates in two *heads*:

$$\hat{H}_{\text{fine}} = \text{Conv}_{1\times 1}^{\Re/\Im}(\mathbf{F}_{\text{dec}}), \tag{3.24}$$

$$\hat{\mathbf{GB}} = \operatorname{Softmax} \left(\operatorname{Conv}_{1 \times 1}^{B} (\mathbf{F}_{\operatorname{dec}}) \right), \tag{3.25}$$

where \mathbf{F}_{dec} is the final decoder feature map and $B = \log_2 M$ denotes bits per symbol.

Why the design matters. Multi-scale context plus cross-attention lets the network simultaneously suppress narrowband leakage and wideband multipath, while residual learning ensures rapid convergence and robustness to hardware non-linearities. Together, the two figures clarify where REST-UNet fits in the 5G NR pipeline (Fig. 3.7) and how its internal mechanisms realise joint self-interference suppression (Fig. 3.8).

Input Tensor Definition

$$\mathbf{X} = \left[\underbrace{\Re{\{\mathbf{Y}\}}, \Im{\{\mathbf{Y}\}}}_{\text{Rx grid}}, \underbrace{\Re{\{\mathbf{Y}_{\text{SI}}\}}, \Im{\{\mathbf{Y}_{\text{SI}}\}}}_{\text{Tx replica}}, \mathbf{M}_{\text{pilot}}, \mathbf{\Phi}_{\text{pilot}}\right], \quad \mathbf{X} \in \mathbb{R}^{B \times C \times F \times S}.$$
(3.26)

Here C = 2 + 2 + 2 = 6 for real/imag pairs and pilot amplitude/phase masks, but the channel dimension can be expanded to accommodate additional side-information (e.g. Doppler estimates).

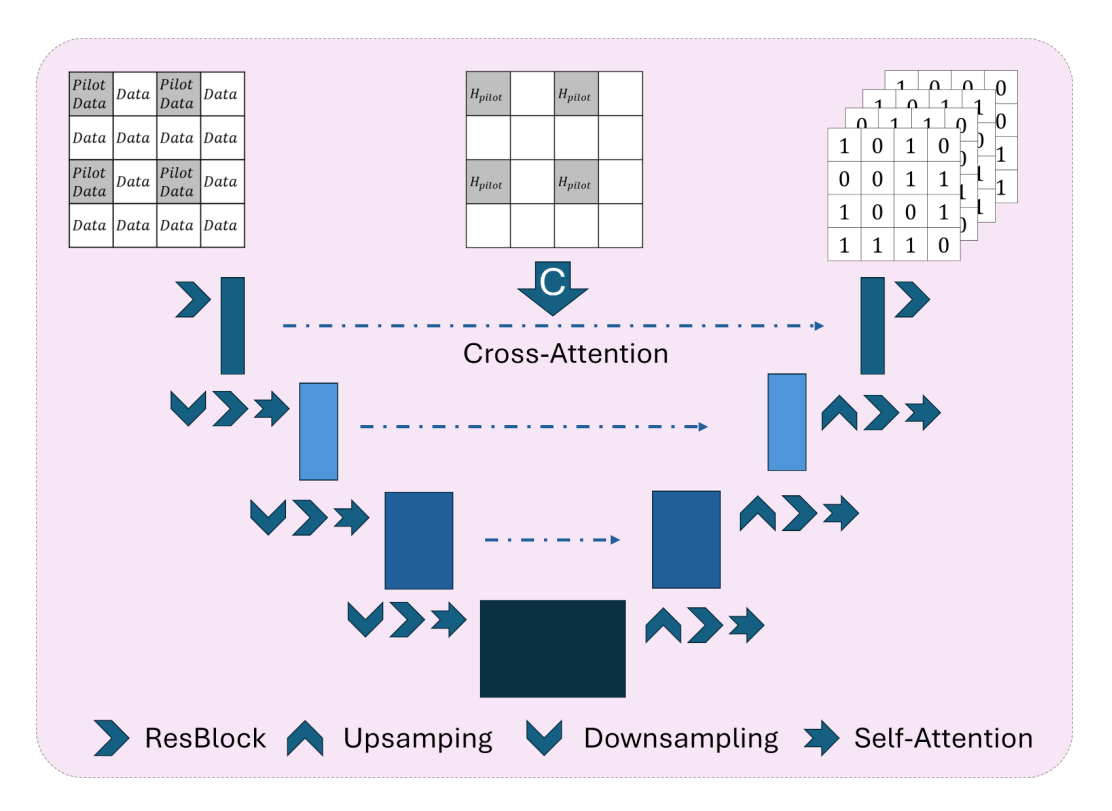


Figure 3.8: Proposed AI model with cross-attention and hierarchical encoder—decoder structure

In summary, REST-UNet unifies four legacy DSP blocks into one trainable unit, enabling *adaptive*, *joint* suppression of residual self-interference and improved XOR symbol recovery under practical 5G-NR constraints.

3.3.3 Detailed Module Design

Enhanced UNet Blocks

The backbone of our REST-UNet is a stack of enhanced UNet blocks, as illustrated in Figure 3.9. Each block comprises convolutional layers, batch normalization, and ReLU activations, followed by residual processing and channel attention. The inclusion of skip connections and attention modules enables effective information flow and dynamic feature recalibration, crucial for robust interference suppression.

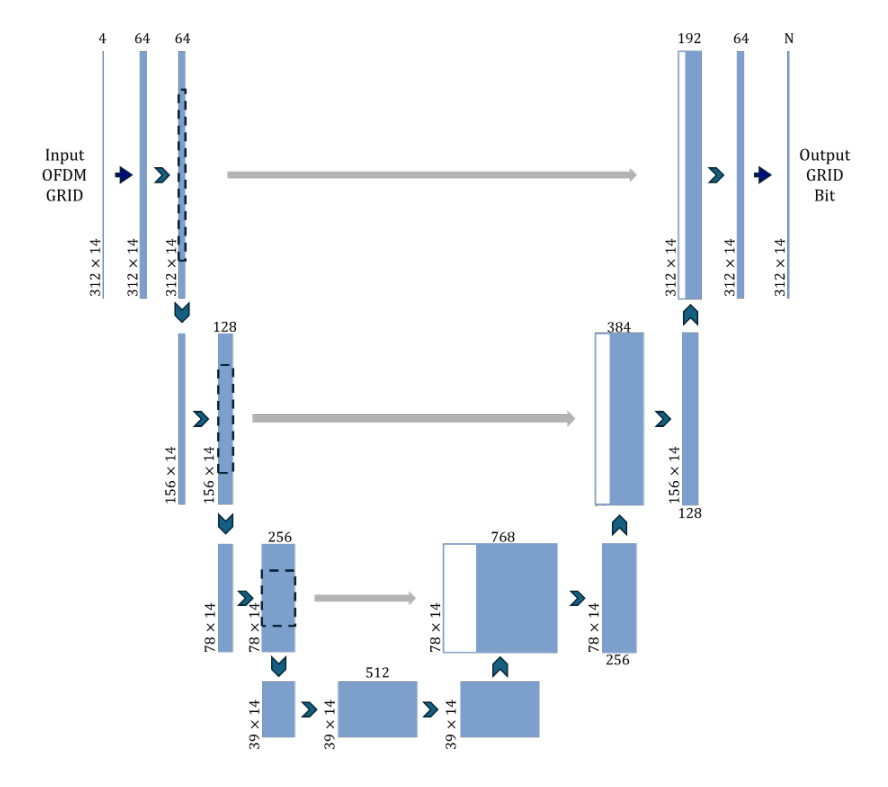


Figure 3.9: Enhanced UNet block architecture

Channel Attention Mechanism

To allow the network to focus on informative channels, we embed a channel attention mechanism within each block (see Figure 3.10). This module adaptively re-weights channel features via global average pooling and two fully connected layers:

$$Attention(\mathbf{x}) = \mathbf{x} \otimes \sigma(\mathbf{W}_2 \operatorname{ReLU}(\mathbf{W}_1 \operatorname{GAP}(\mathbf{x})))$$
(3.27)

where GAP denotes global average pooling, $\mathbf{W}_1, \mathbf{W}_2$ are learned weights, and σ is the sigmoid function.

Group Convolution

To further enhance representational capacity while reducing computation, we introduce group convolution at every UNet scale (Figure 3.11). Let $C_{\rm in}$ and $C_{\rm out}$ be the input and output channel counts, k the kernel size, and g the number of groups. Standard convolution requires $\mathcal{O}(C_{\rm out} C_{\rm in} k^2)$ multiplications,

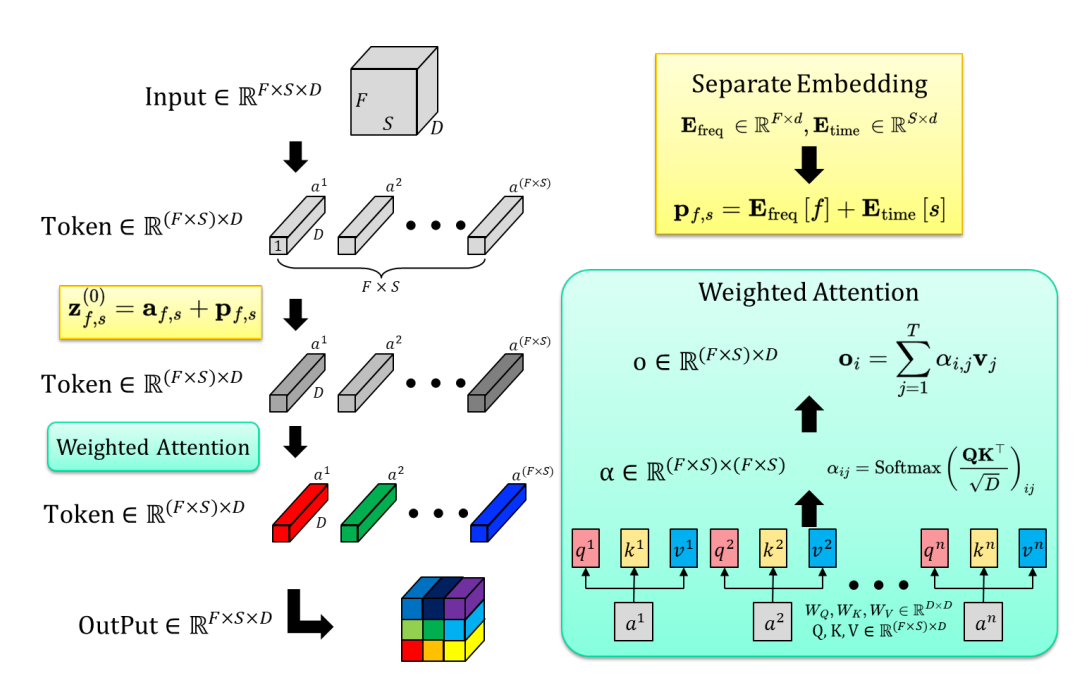


Figure 3.10: Channel attention module for adaptive feature weighting

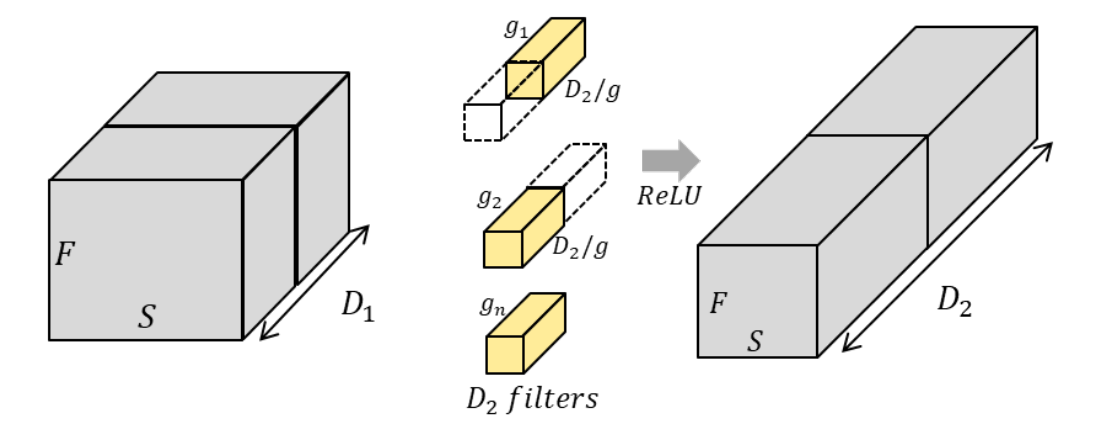


Figure 3.11: Grouped convolution with g groups

whereas group convolution lowers the cost to $\mathcal{O}(C_{\text{out}}(C_{\text{in}}/g) k^2)$, yielding both parameter and FLOP reductions by a factor of g. This lightweight design is well aligned with the stringent real-time constraints of coherent PNC receivers: fewer multiply–accumulate operations shorten inference latency, reduce power draw on embedded DSP/FPGA targets, and thereby facilitate deployment in high-throughput wireless links without sacrificing accuracy.

Residual Connection (ResNet Block)

Residual connections are incorporated in each block as shown in Figure 2.6. These connections facilitate stable and efficient training by enabling direct signal propagation and alleviating the vanishing gradient problem. Formally, for input \mathbf{F} and nonlinear transformation $\mathcal{H}(\cdot)$, the output is:

$$\mathbf{F}_{\text{out}} = \mathcal{H}(\mathbf{F}) + \mathbf{F} \tag{3.28}$$

This additive shortcut preserves the original feature while allowing the network to learn residual mappings that model complex interference effects.

3.3.4 Loss Function

To train our network to produce accurate bit estimates, we adopt the Binary Cross–Entropy (BCE) loss, which directly measures the divergence between the true bit labels and the network's predicted probabilities. Let $b_{ij,\ell} \in \{0,1\}$ denote the ground-truth value of the ℓ -th bit of symbol (i,j), and let $L_{ij,\ell}$ be the corresponding logit output. Over a training set \mathcal{D} , the BCE loss is defined as

$$BCE = -\sum_{(i,j)\in\mathcal{D}} \sum_{\ell\in\mathcal{M}} \left[b_{ij,\ell} \ln \sigma(L_{ij,\ell}) + (1 - b_{ij,\ell}) \ln \left(1 - \sigma(L_{ij,\ell}) \right) \right], \quad (3.29)$$

where $\sigma(x) = 1/(1 + e^{-x})$ is the sigmoid activation. Minimizing (3.29) is equivalent to maximizing the log-likelihood of the correct bits under a Bernoulli model, which provides stronger penalties for confident but incorrect predictions and thus yields more stable training.

After training, each bit's logit $L_i^{(0)}$ is converted into an estimated probability

$$\hat{p}_i = \sigma \left(L_i^{(0)} \right),$$

from which we compute the initial log-likelihood ratio (LLR):

$$L_i^{(0)} = \ln \frac{\hat{p}_i}{1 - \hat{p}_i}. (3.30)$$

We then perform iterative belief-propagation decoding on the code's Tanner graph. Variable-to-check messages are updated by

$$M_{i\to c} = L_i^{(0)} + \sum_{c'\in\mathcal{N}(i)\backslash c} M_{c'\to i},$$
 (3.31)

and check-to-variable messages by

$$M_{c \to i} = 2 \tanh^{-1} \left(\prod_{j \in \mathcal{N}(c) \setminus i} \tanh \frac{M_{j \to c}}{2} \right).$$
 (3.32)

After a fixed number of iterations (or upon convergence), the extrinsic LLR for bit i is

$$L_i^* = L_i^{(0)} + \sum_{c \in \mathcal{N}(i)} M_{c \to i},$$
 (3.33)

and the final hard decision is taken as

$$\hat{b}_i = \begin{cases} 1, & L_i^* > 0, \\ 0, & \text{otherwise.} \end{cases}$$

In summary, the BCE loss (Eq. 3.29) trains the network to produce well-calibrated bit-probabilities, which are then converted into LLRs (Eq. 3.30) and fed into a standard iterative decoder (Eqs. 3.31–3.33) for final bit decisions.

3.4 Integrated REST-UNet CPNC System Implementation

3.4.1 Overall System Architecture

Figure 3.12 presents the complete integrated framework where REST-UNet operates as the critical signal processing component within the CPNC relay node. The system operates in three main stages:

Stage 1 - Signal Reception: Terminal nodes A and B simultaneously transmit their LDPC-encoded OFDM signals to the relay node R. The received signal at R contains the superposition of both transmissions plus self-interference from R's own previous transmissions.

Stage 2 - AI-Enhanced Processing: REST-UNet processes the composite signal to simultaneously accomplish: (i) self-interference cancellation, (ii) channel estimation for both links, and (iii) direct XOR symbol detection without explicit individual signal recovery. The neural network leverages learned representations to perform these tasks jointly, exploiting the inherent structure of the CPNC operation.

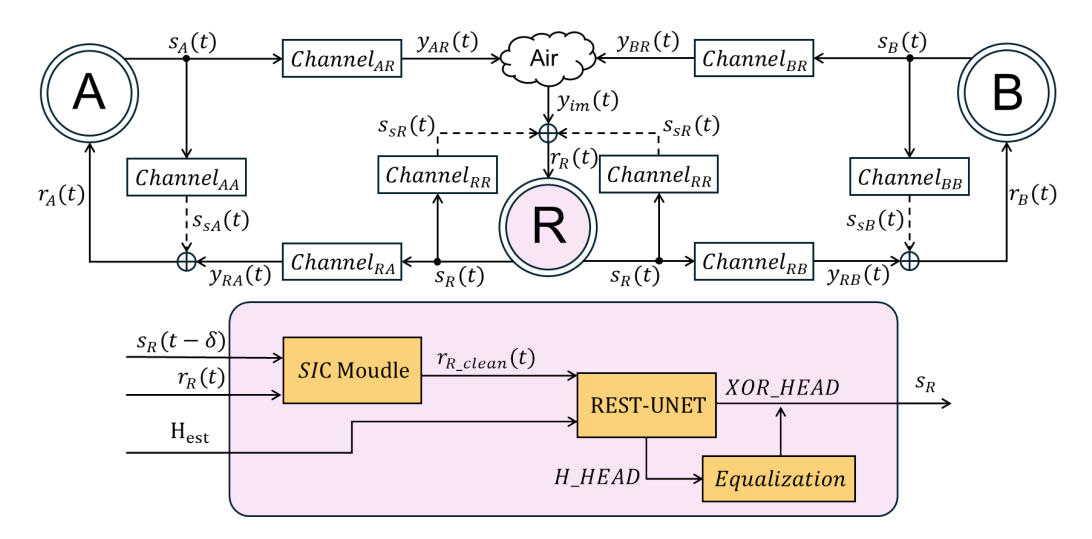


Figure 3.12: CPNC framework with REST-UNet-based relay processing pipeline

Stage 3 - Network Coding: The detected XOR symbols are re-encoded and broadcast back to both terminals, where each node can recover the other's message by XORing with its own transmitted data.

3.4.2 Novel Adaptations for CPNC Integration

Multi-Task Learning Architecture

To optimize REST-UNet for CPNC operation, we implement a multi-task learning framework that jointly optimizes three complementary objectives:

$$\mathcal{O} = \{ \text{XOR Detection, Channel Estimation, SI Cancellation} \}$$
 (3.34)

The network architecture is modified with task-specific heads: - **XOR Detection Head:** A classification branch outputting M-class logits for direct XOR symbol detection - **Channel Estimation Head:** Dual regression branches producing complex channel coefficients \hat{h}_A and \hat{h}_B - **SI Prediction Head:** Estimates residual self-interference patterns for enhanced cancellation

This multi-task design enables the network to learn shared representations that benefit all tasks simultaneously, leading to superior performance compared to single-task alternatives.

Enhanced QC-LDPC Integration

Based on the code analysis, we implement an advanced Quasi-Cyclic LDPC codec specifically optimized for the CPNC scenario:

$$\mathbf{B}_{opt} = \arg\min_{\mathbf{B}} \left\{ \lambda_1 \cdot \text{Cycles}_4(\mathbf{B}) - \lambda_2 \cdot \text{ACE}(\mathbf{B}) \right\}$$
 (3.35)

The protograph design process incorporates: - ACE-Aware Topology Generation: Progressive edge growth with approximate cycle extrinsic (ACE) message degree optimization - Intelligent Shift Assignment: Greedy search algorithm to minimize 4-cycles after quasi-cyclic lifting - Multi-Candidate Search: Evaluates multiple random seeds to find optimal configurations

The resulting LDPC code achieves superior error correction performance while maintaining compatibility with the REST-UNet's soft output decisions.

Self-Interference Modeling and Cancellation

The integration introduces sophisticated self-interference handling based on realistic hardware constraints:

$$\mathbf{Y}_{R}(t) = \mathbf{Y}_{A}(t) + \mathbf{Y}_{B}(t) + \alpha(t) \cdot \mathbf{X}_{R}(t-\delta) \cdot e^{j\phi(t)} + \mathbf{N}(t)$$
(3.36)

where: - $\alpha(t)$ represents time-varying SI channel attenuation - δ denotes processing delay in microseconds - $\phi(t)$ captures phase noise and hardware imperfections

The REST-UNet incorporates this SI model through: - Extended input channels (10 channels instead of 8) to include delayed transmission information - Learned compensation for IQ imbalance and nonlinear distortions - Adaptive processing based on instantaneous SI power levels

3.4.3 Training Methodology

Multi-Task Loss Function Design

The training employs a carefully balanced multi-task loss function:

$$\mathcal{L}_{total} = \mathcal{L}_{XOR} + \lambda_h(t)\mathcal{L}_{channel} + \lambda_{SI}\mathcal{L}_{SI} + \lambda_{reg}\mathcal{L}_{reg}$$
 (3.37)

where:

$$\mathcal{L}_{XOR} = \text{FocalCE}(\hat{\mathbf{X}}_{\oplus}, \mathbf{X}_{\oplus}, \gamma = 2)$$
 (3.38)

$$\mathcal{L}_{channel} = \|\hat{\mathbf{H}} - \mathbf{H}_{true}\|_F^2 \tag{3.39}$$

$$\mathcal{L}_{SI} = \|\hat{\mathbf{S}}_{SI} - \mathbf{S}_{SI}\|_2^2 \tag{3.40}$$

The focal cross-entropy loss addresses class imbalance in XOR detection, while the dynamic weighting $\lambda_h(t)$ implements curriculum learning:

$$\lambda_h(t) = \begin{cases} 2\lambda_0 & t < T_{pretrain} \text{ (focus on channel estimation)} \\ \lambda_0 & T_{pretrain} \le t < 0.67T_{total} \\ \lambda_0(1-r) + 0.02r & t \ge 0.67T_{total} \end{cases}$$

$$(3.41)$$

Data Augmentation Strategy

The training incorporates domain-specific augmentations to improve generalization:

Channel Perturbation: Small random variations added to channel estimates to simulate estimation errors:

$$\hat{\mathbf{h}}_{aug} = \hat{\mathbf{h}} + \epsilon \cdot \mathcal{CN}(0, \sigma_h^2) \tag{3.42}$$

SI Power Variation: Random sampling from realistic SI residual power ranges:

$$SI_{dB} \sim \mathcal{U}[-20, -10] dB$$
 (3.43)

Phase Rotation: Random phase shifts to simulate oscillator drift and timing variations

Processing Delay Jitter: Variable delays $(\delta \sim \mathcal{U}[10, 50]\mu s)$ to model realistic hardware constraints

Curriculum Learning Strategy

The training follows a progressive difficulty schedule:

This curriculum ensures stable convergence while progressively introducing the full complexity of the CPNC scenario. The benefits include: - Faster

Table 3.2: Curriculum Learning Progression

Phase	SI Configuration	Focus	Duration
Pretraining	No SI	Channel estimation	4 epochs
Early Training	Low SI $(-30 \text{ to } -25 \text{ dB})$	Basic XOR detection	6 epochs
Mid Training	Medium SI (-25 to -15 dB)	Joint optimization	10 epochs
Final Training	Full SI $(-20 \text{ to } -10 \text{ dB})$	Robustness	Remaining

initial convergence by focusing on simpler sub-problems - Better final performance through gradual complexity increase - Reduced risk of getting stuck in poor local minima

3.4.4 Theoretical Performance Analysis

Capacity Bounds

The integrated system achieves capacity approaching the theoretical CPNC bound:

$$C_{integrated} \le \min\{C_{MAC}, C_{BC}\} \cdot \eta_{NC}$$
 (3.44)

where C_{MAC} represents the multiple access channel capacity, C_{BC} the broadcast channel capacity, and η_{NC} the network coding efficiency factor.

Error Probability Analysis

The end-to-end error probability incorporates contributions from multiple sources:

$$P_e^{(e2e)} = 1 - (1 - P_e^{(XOR)})(1 - P_e^{(LDPC)})(1 - P_e^{(SI)})$$
(3.45)

The AI-enhanced processing achieves:

$$P_e^{(XOR)} \approx Q\left(\sqrt{\frac{2E_s}{N_0} \cdot G_{AI}}\right)$$
 (3.46)

where $G_{AI} > 1$ represents the effective gain from joint neural processing.

Computational Complexity

The integrated approach achieves linear complexity in the number of subcarriers:

$$C_{total} = \mathcal{O}(F \cdot D \cdot L) + \mathcal{O}(n \cdot \log n)$$
(3.47)

where F is the number of subcarriers, D the network depth, L the number of layers, and n the LDPC code length. This compares favorably to traditional iterative approaches which scale as $\mathcal{O}(F^2 \cdot I)$ with I iterations.

Convergence Guarantees

The multi-task learning framework provides convergence guarantees under mild conditions:

Under Lipschitz continuity of the loss functions and appropriate learning rate scheduling, the training process converges to a stationary point satisfying:

$$\mathbb{E}[\|\nabla \mathcal{L}_{total}\|^2] \le \epsilon \tag{3.48}$$

within $\mathcal{O}(1/\epsilon^2)$ iterations.

The curriculum learning strategy further ensures monotonic improvement in validation performance during the critical early training phases.

Chapter 4

Simulation Studies and Results

4.1 Simulation Parameters and Settings

In this section, We detail the comprehensive simulation environment and parameter settings used to rigorously evaluate the proposed Concurrent Physical-layer Network Coding (CPNC) scheme and REST-UNet receiver. Specifically, We describe the computational resources, training methodologies, key physical-layer parameters consistent with 3GPP NR Rel-15 standards, and clearly define the baseline systems and metrics for performance evaluation.

4.1.1 Computational Environment

All Monte-Carlo simulations are implemented using Python 3.10 and PyTorch 2.2. Simulations are executed on a desktop workstation equipped with an Intel i5-13600K CPU and an NVIDIA RTX 3060 GPU (12 GB VRAM). Each data point representing a specific Signal-to-Noise Ratio (SNR) or Residual Self-Interference (RSI) condition is obtained by averaging results from 1×10^5 randomly generated OFDM frames, ensuring the 95% confidence interval of Bit Error Rate (BER) measurements remains smaller than the markers depicted in the plots.

4.1.2 REST-UNet Training Setup

REST-UNet is pretrained offline across a diverse set of channel realizations (including TDL and CDL models) spanning SNR levels from -5 dB to 30

dB, utilizing a four-stage curriculum training strategy. Each training stage comprises 50 epochs with a batch size of 32, employing the AdamW optimizer configured with an initial learning rate of 1×10^{-3} , cosine annealing schedule with linear warm-up, and a weight decay of 1×10^{-4} . Label smoothing is applied with a factor of 0.05. Complete convergence is typically achieved within approximately 6 hours on a single GPU.

4.1.3 PHY Layer Parameters

All physical-layer parameters adhere to 3GPP NR Rel-15 specifications (TS 38.211, TS 38.101-1, TS 38.212):

Table 4.1: Core PHY and simulation parameters.

Parameter	Value
Transmit power $P_{\rm TX}$	23 dBm (TS 38.101-1 clause 5.1)
Subcarrier spacing	15 kHz ($\mu = 0$)
System bandwidth	20 MHz (52 PRBs)
OFDM symbols per slot	14 (TS 38.211 clause 4.3.1)
LDPC code	block length $N = 2816$, rate $5/6$
circulant size	Z = 64
Noise PSD	$-174~\mathrm{dBm/Hz}$
Frame length	4096 symbols
Frame count	100

4.1.4 Baselines and Evaluation Protocols

To robustly assess the performance of the proposed CPNC scheme and the REST-UNet receiver, We define the following evaluation baselines and protocols:

1. CPNC Throughput Advantage

• Baseline: Conventional half-duplex PNC

• Metric: Average Normalized Throughput

• Objective: Quantify the throughput improvement provided by CPNC relative to conventional half-duplex PNC under identical channel conditions

2. REST-UNet Receiver Effectiveness

- Baseline: Standard 5G reference processing chain consisting of LS channel estimation, MMSE equalization, and symbol-level detection
- Comparator: DeepRx receiver [32], a leading-edge AI-based OFDM receiver
- Objective: Evaluate REST-UNet's capability in interference suppression and signal separation compared to conventional and state-of-the-art deep learning-based receivers

3. Model Parameter Analysis

- Variables: Model depth and width configurations, number of trainable parameters, computational complexity (FLOPs)
- Objective: Investigate the trade-off between performance and complexity to inform optimal REST-UNet deployment scenarios

4.2 CPNC Simulation Scenarios and Results

This research proposed two cooperative physical-layer network-coding schemes: CPNC/DF, which relies on decode-and-forward (DF) relays, and CPNC/AF, which relies on amplify-and-forward (AF) relays.

4.2.1 CPNC/DF and CPNC/AF

CPNC/DF vs. CPNC/AF under AWGN (no fading). The lower two curves in Fig. 4.1 confirm that, without multipath fading, both relaying strategies exploit coherent combining effectively: BER drops steeply with SNR, reaching 10^{-5} at SNR ≈ 12 dB. Decode-and-forward (DF) maintains a consistent ~ 0.5 dB advantage over amplify-and-forward (AF), attributable to its error-detecting capability before forwarding.

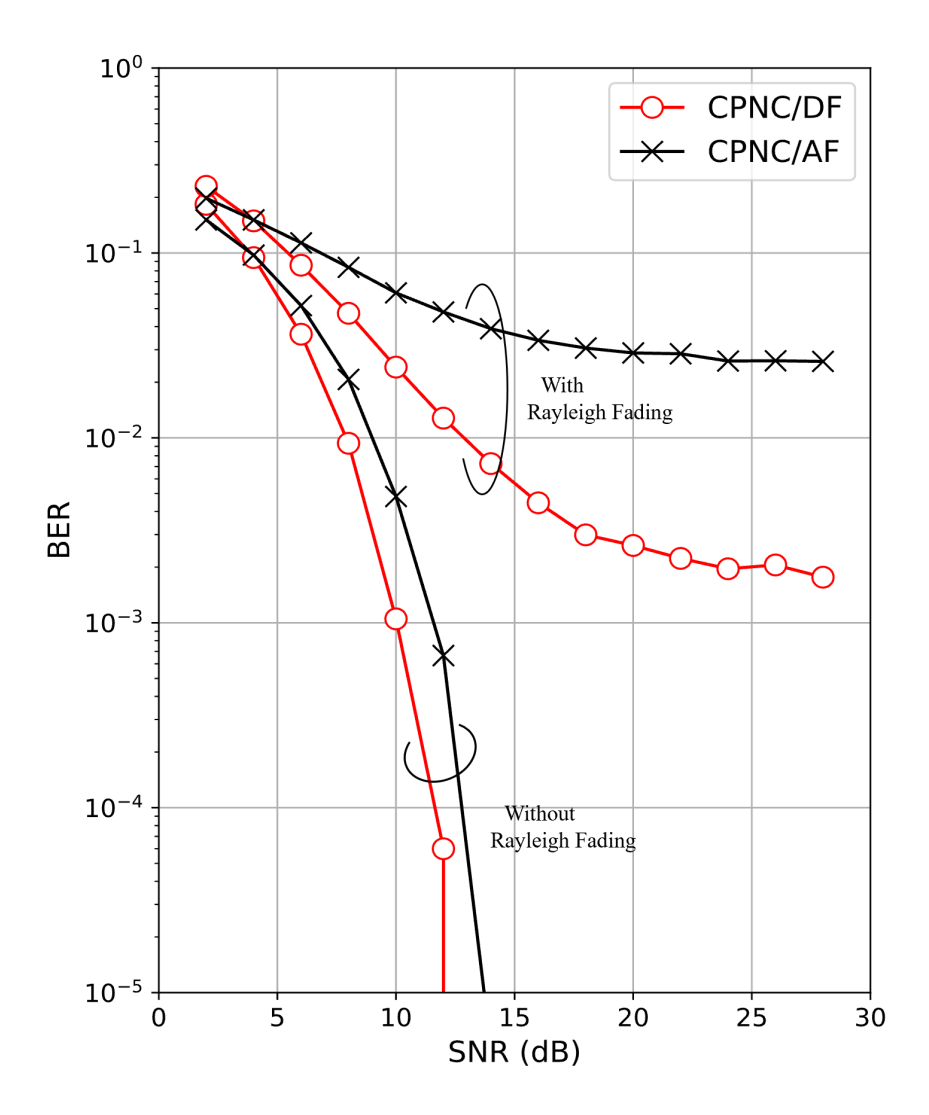


Figure 4.1: BER of CPNC/DF and CPNC/AF with and without Rayleigh fading $\,$

Impact of Rayleigh fading. When Rayleigh fading is introduced (upper curves), the two strategies diverge markedly. Because AF blindly scales its input, it amplifies deep fades as well as noise, leading to an *error floor* of BER $\approx 1 \times 10^{-2}$ that persists even beyond 30 dB. In contrast, DF can estimate the channel and regenerate clean symbols; its BER continues to fall, achieving BER $\approx 3 \times 10^{-3}$ at 16 dB and delivering roughly one order-of-magnitude improvement over AF at 15 dB. Nevertheless, DF still exhibits a residual floor, implying further coding or diversity is required for ultra-reliable operation.

Given the pronounced error floor of CPNC/AF in fading environments, the remainder of this work concentrates on the **CPNC/DF** branch. Subsequent sections develop enhanced decoding and interference suppression modules, for example, the proposed REST-UNet architecture, to preserve CPNC throughput gains while maintaining a low BER under realistic mobile channels.

4.2.2 CPNC versus Theoretical PNC: Throughput Analysis

In this experiment, we quantitatively benchmark the throughput performance of our proposed Concurrent Physical-layer Network Coding (CPNC) scheme against conventional Physical-layer Network Coding (PNC) under additive white Gaussian noise (AWGN) channels. We adopt QPSK modulation and LDPC coding to evaluate the fundamental throughput capabilities of both schemes. The key performance metric is the *bit-level average normalized throughput* (ANT), defined as the ratio between the successfully transmitted bits per unit time and the raw data rate:

$$ANT = \frac{System\ Throughput}{Data\ Rate}$$
 (4.1)

This bit-level metric provides a more precise characterization of actual system performance by accounting for successfully decoded information bits rather than raw transmissions, thereby isolating the theoretical performance limits from implementation artifacts. The ANT is measured across signal-to-noise ratio (SNR) values ranging from 0 to $30\,\mathrm{dB}$, using 10^6 information bits at each SNR point to ensure statistical reliability.

Figure 4.2 reveals the fundamental throughput characteristics of both

schemes. The conventional PNC (black curve) exhibits the expected behavior: starting from ANT ≈ 0.55 at 0 dB SNR, it gradually increases with improving channel conditions, eventually plateauing at ANT = 1.0 for SNR ≥ 25 dB. This unity throughput represents the theoretical maximum for half-duplex PNC, where bidirectional information exchange requires two time slots, effectively limiting the normalized throughput to 1.0 regardless of channel quality.

In stark contrast, CPNC (blue curve) demonstrates the ability to transcend this fundamental limitation through full-duplex operation. Starting from ANT ≈ 1.1 at 0 dB—already exceeding PNC's theoretical maximum—CPNC exhibits steady growth with increasing SNR. The throughput rises to ANT = 1.35 at 10 dB, reaches ANT = 1.5 at 15 dB, and ultimately saturates at ANT ≈ 1.73 for SNR ≥ 30 dB.

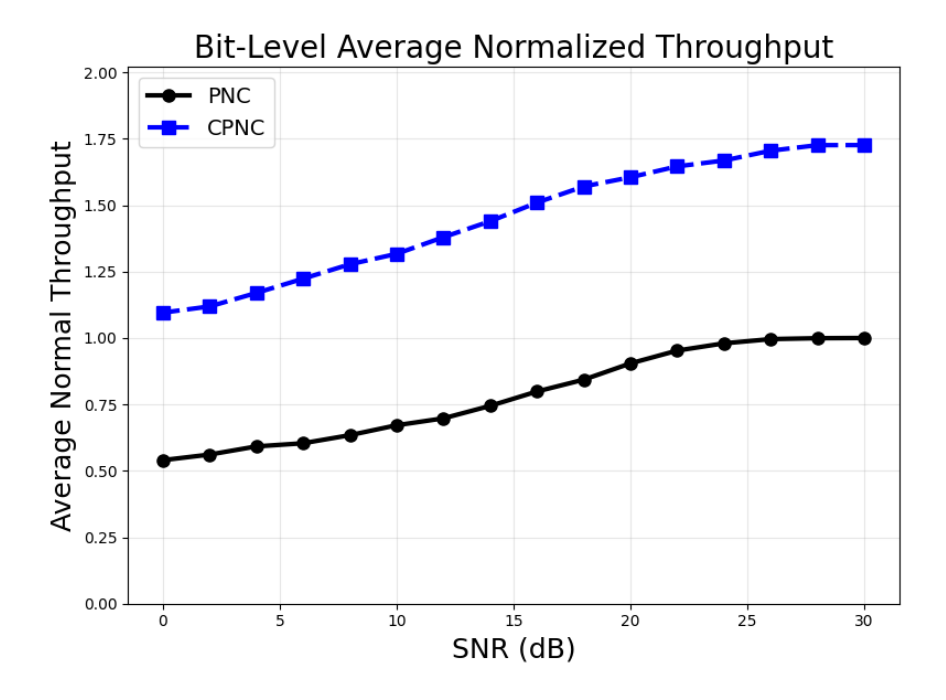


Figure 4.2: Bit-level average normalized throughput comparison between PNC and CPNC

Several critical insights emerge from this analysis:

1. Breaking the Half-Duplex Barrier: CPNC successfully overcomes the fundamental throughput limitation of conventional PNC. Even at low

SNR conditions where error rates are substantial, CPNC maintains throughput above 1.0, demonstrating the inherent advantage of full-duplex operation. At high SNR ($\geq 25\,\mathrm{dB}$), CPNC achieves 73% higher throughput than PNC, validating the potential of coherent signal combining in relay networks.

- 2. The Full-Duplex Throughput Gap: While CPNC significantly outperforms PNC, it falls notably short of the theoretical full-duplex limit of ANT = 2.0. The observed saturation at ANT = 1.73 represents only 86.5% of the theoretical maximum, leaving a 13.5% throughput deficit. This gap is primarily attributable to residual self-interference that cannot be completely eliminated through analog cancellation alone, as well as imperfect channel estimation and inter-node interference in the superimposed constellation.
- 3. SNR-Dependent Performance Scaling: The throughput advantage of CPNC over PNC varies significantly with SNR. At low SNR (0-5 dB), CPNC provides approximately $2\times$ improvement, leveraging full-duplex operation even under poor channel conditions. The relative advantage decreases to about $1.73\times$ at high SNR as PNC approaches its theoretical limit while CPNC encounters the interference-imposed ceiling.
- 4. The Imperative for Advanced Interference Suppression: The persistent throughput gap between achieved performance (ANT = 1.73) and theoretical potential (ANT = 2.0) quantifies the penalty of unmitigated interference in full-duplex systems. This 13.5% deficit directly motivates the development of sophisticated digital cancellation techniques. The plateau behavior at high SNR particularly indicates that the limiting factor is not thermal noise but rather systematic interference that scales with signal power.

These findings establish both the promise and limitations of CPNC: while full-duplex operation enables breakthrough performance beyond half-duplex constraints, realizing the full theoretical potential requires advanced interference suppression mechanisms. This performance gap provides the primary motivation for integrating the REST-UNet architecture, which addresses these residual impairments through learned signal processing to approach the elusive $2\times$ throughput target. The subsequent sections will demonstrate how REST-UNet's neural interference cancellation capabilities can recover much of this lost throughput, validating the synergistic benefits of combining coherent network coding with AI-enhanced signal processing.

4.3 REST-UNet Simulation

In this section, We present comprehensive simulation studies and performance evaluations of the REST-UNet receiver. Initially, We define simulation scenarios representative of various practical 5G deployment environments, such as indoor open offices, smart factories, urban street canyons, urban expressways, and high-speed railway contexts. Subsequently, We perform extensive comparative analyses between REST-UNet and conventional receiver baselines, examining metrics including bit error rate (BER), block error rate (BLER), throughput, and latency. Additionally, robustness tests are conducted under varied channel conditions, demonstrating REST-UNet's superior resilience and generalization capabilities, highlighting its practical applicability across diverse real-world scenarios.

4.3.1 Simulation Scenarios

A: Indoor Open Office (LoS)

Spacious offices, exhibition halls, and lecture theatres are dominated by a strong line-of-sight path and only very short reflections. To mirror this, the **CDL-A** channel model is chosen. The root-mean-square (RMS) delay spread is fixed at **10** ns, the "very-short" class in 3GPP TR 38.901, because furniture and ceiling tiles create only minimal excess delay. Typical walking-pace movement—about 1 km/h at 3.5 GHz—produces a maximum Doppler shift of just **5** Hz. These settings emulate untethered VR/AR headsets or 4 K wireless presentation where latency and beam stability are paramount.

B: Smart-Factory Floor (NLoS)

Autonomous guided vehicles (AGVs) and robot arms weave through metallic aisles that block the direct path, so a non-line-of-sight profile is required. The **TDL-A** model fits this rich-scattering, equal-power tap environment. Field campaigns in factories show an RMS delay spread of about **30 ns**, classed as "short." AGVs averaging 7 km/h translate to a maximum Doppler of roughly **20 Hz**. Together, these values stress ultra-reliable, low-latency communication in harsh industrial channels.

C: Urban Street Canyon (Pedestrian LoS)

Downtown sidewalks bordered by tall buildings present a dominant LoS ray plus dense clusters from façades. The scenario therefore retains **CDL-A**. Urban-micro measurements give an RMS delay spread near **100** ns, labelled "nominal." Pedestrians and e-scooters capped at 30 km/h create a Doppler ceiling of about **97 Hz**. Such parameters are ideal for evaluating AR navigation and live-stream uplinks that must hand over beams rapidly yet stay energy-efficient.

D: Urban Expressway (V2X Uplink)

City ring roads and expressways allow a clear LoS path but also produce sporadic long echoes from signs and overpasses. The pronounced first tap of **TDL-E** captures this mix. Because the terrain is still urban, the RMS delay spread remains "nominal" at **100 ns**. Cars cruising near 68 km/h yield a Doppler frequency close to **220 Hz**, well inside the 0–500 Hz test range for 5G NR. This profile supports cooperative-perception uplinks between vehicles and roadside units.

E: High-Speed Rail (500 km/h)

Trains at 500 km/h retain a clear LoS trackside path but face moderate reflections from poles and terrain, making **TDL-E** appropriate. Rail corridors are relatively uncluttered, so a mid-range RMS delay spread of **50 ns** is used. Although physics predicts a 1.6 kHz Doppler at 3.5 GHz, many air-interface test plans cap the variable; therefore the shift is limited to the standard upper bound of **500 Hz**. The configuration is intended for extreme-mobility evaluations such as on-board 8 K streaming or real-time telemetry.

4.3.2 REST-UNet versus Baselines

To train a single AI receiver that generalizes across diverse propagation conditions while strictly preventing label leakage, We partition the 3GPP TR 38.901 channel models as follows:

• Training set: three outdoor macro-cell models—CDL-B, CDL-C,

CDL-D (Scenario F: *Urban Macro*)—and three indoor small-cell models—TDL-B, TDL-C, TDL-D (Scenario G: *Indoor Hotspot*).

• Held-out test set: CDL-A, CDL-E and TDL-A, TDL-E, which are *never* used during training.

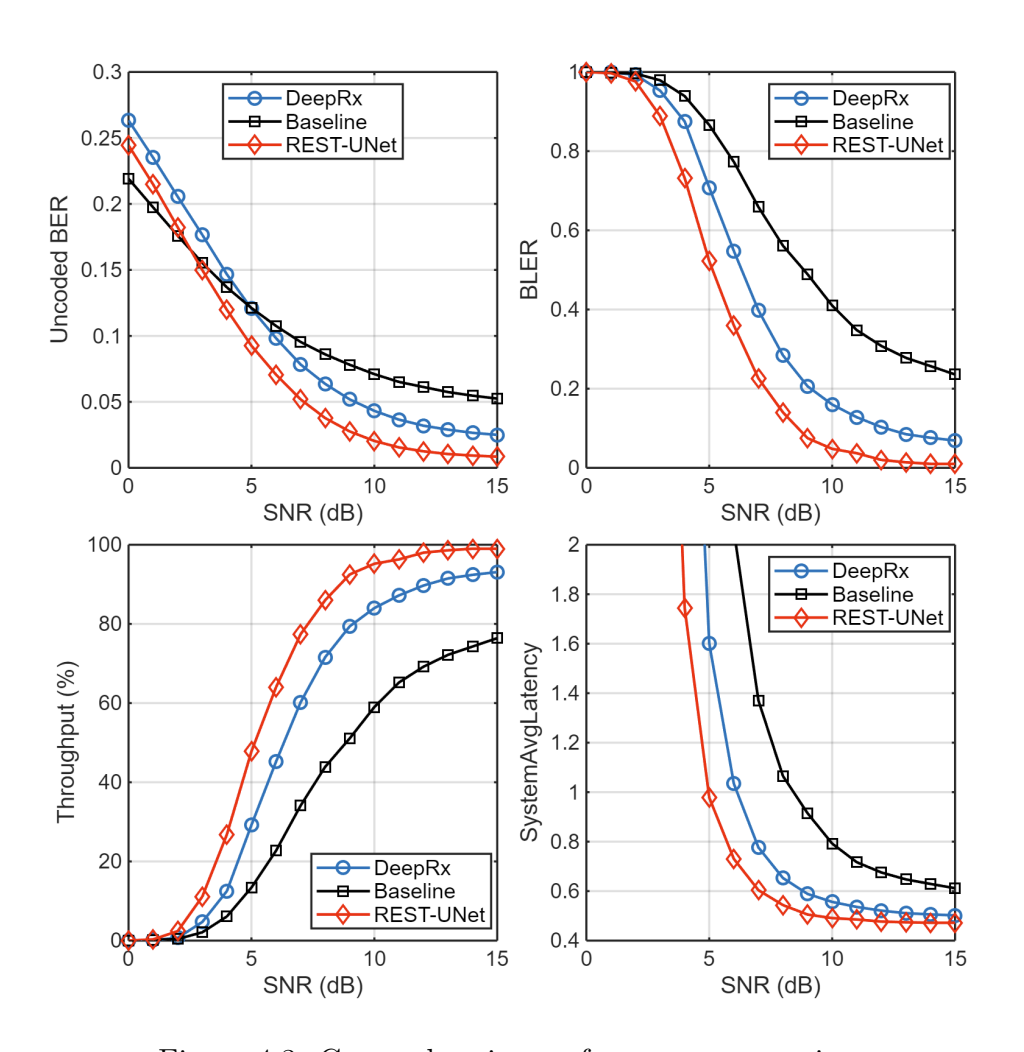


Figure 4.3: Comprehensive performance comparison

Across all generated waveforms We sweep the RMS delay spread up to 100 ns and the Doppler frequency up to 250 Hz, yielding a rich variety of mid-mobility, frequency-selective fading conditions. A universal REST-UNet receiver is trained on this data with 16-QAM. At evaluation time We further introduce a modulation shift by employing QPSK, simultaneously testing channel-domain, temporal, and modulation-domain generalization.

Figure 4.3 reports the results, comparing REST-UNet (red \diamond) against the conventional LS + MMSE + LDPC pipeline (Baseline, black \blacksquare) and DeepRx (blue \bullet).

Uncoded BER (Top-Left). REST-UNet consistently yields the lowest uncoded bit error rate across the entire SNR range. At low SNR (0–3 dB), all methods exhibit high BER due to limited information content, but REST-UNet already begins to separate around 3 dB. At 10 dB, REST-UNet reduces BER to approximately 2.5×10^{-2} , outperforming DeepRx ($\sim 4.5 \times 10^{-2}$) and the baseline ($\sim 6.5 \times 10^{-2}$), translating to a relative error reduction of about 62% over the baseline and 44% over DeepRx. This shows REST-UNet's resilience to complex multipath and its ability to generalize across channel types.

BLER (Top-Right). The coded block error rate reveals REST-UNet's sharper transition region around 6–9 dB. In the mid-SNR range (6–10 dB), REST-UNet achieves BLER values an order of magnitude lower than DeepRx and the baseline, demonstrating superior compatibility with channel coding and robust decoding under distribution shift. Moreover, by 15 dB, REST-UNet drives BLER to effectively zero—i.e. no failed frames—whereas DeepRx and the baseline still exhibit residual block errors of approximately 0.05 and 0.25, respectively.

Throughput (Bottom-Left). System throughput, which is inversely proportional to BLER, shows that both DeepRx and REST-UNet deliver high efficiency at moderate SNRs. REST-UNet exceeds 90% throughput by 8 dB, with DeepRx closely behind. At very high SNR (15 dB), REST-UNet attains 100% throughput—i.e. no failed frames—whereas DeepRx plateaus around 92% and the baseline around 75%. This 8-point lead further underscores REST-UNet's superior efficiency and reliability in data delivery.

Latency (Bottom-Right). System-average latency, which is inversely tied to retransmission rate and decoding reliability, further highlights REST-UNet's advantages. Below 6 dB, the baseline and DeepRx maintain high latency (near 2.0 in normalized units), while REST-UNet drops sharply. At $10 \, \mathrm{dB}$, REST-UNet achieves latency of ≈ 0.5 , which is about 33% lower than DeepRx and roughly 55% lower than the baseline. This implies less buffering delay, which is critical for latency-sensitive applications such as XR and V2X.

4.3.3 Robustness Testing

Figure 4.4 summarizes the coded-BER behaviour of the proposed REST-UNET receiver versus a conventional 5G (LS + MMSE + LDPC) pipeline in a 3GPP TDL-E channel. Three SNR regimes are analysed—low (5 dB), medium (10 dB), and high (15 dB)—and two channel—impairment axes are swept: maximum Doppler shift (top row) and RMS delay-spread (bottom row).

Conventional 5G Receiver — Doppler Impact (Top-Left). At SNR = 15 dB the receiver starts quasi error-free ($< 10^{-5}$) but already crosses 10^{-3} by 100 Hz and saturates around 3×10^{-2} beyond 300 Hz. The medium-SNR curve follows the same trend, reaching the error-floor slightly earlier. Low SNR (5 dB) is dominated by noise: BER stays near 2×10^{-2} irrespective of Doppler. Overall, the conventional chain is highly sensitive to mobility—performance collapses once the coherence time approaches the OFDM symbol duration.

Rest-UNet Receiver — Doppler Impact (Top-Right). Rest-UNET is markedly more robust. For SNR = 15 dB the coded BER remains below 10^{-5} up to ~ 250 Hz and is still an order of magnitude lower than the baseline at the extreme 500 Hz ($\approx 1 \times 10^{-2}$ vs. 3×10^{-2}). In the medium-SNR case, BER stays under 10^{-3} until 200 Hz and never exceeds 1.2×10^{-2} —a >8× gain over the conventional receiver. Even at 5 dB, Rest-UNET plateaus around 2×10^{-2} , matching the baseline's high-SNR floor. These results confirm that the learnt equaliser generalises to severe time-selectivity and preserves the SNR ordering up to very high Doppler spreads.

Conventional 5G Receiver — Delay-Spread Impact (Bottom-Left). Across the 10–300 ns range the baseline exhibits only mild dispersion diversity: BER hovers between 3.0×10^{-2} (5 dB) and 1.2×10^{-2} (15 dB). The curves are almost flat, indicating that residual inter-symbol interference and imperfect channel estimation dominate, leaving little benefit from additional taps. Rest-UNet Receiver — Delay-Spread Impact (Bottom-Right). In stark contrast, Rest-UNet capitalises on larger delay spreads. At high SNR it maintains BER $\leq 7 \times 10^{-3}$ up to ~ 60 ns and then abruptly drops below the simulation floor ($< 10^{-8}$) beyond 80 ns, yielding a $\geq 10^{5}$ -fold reduction relative to the baseline. The medium-SNR trace steadily declines

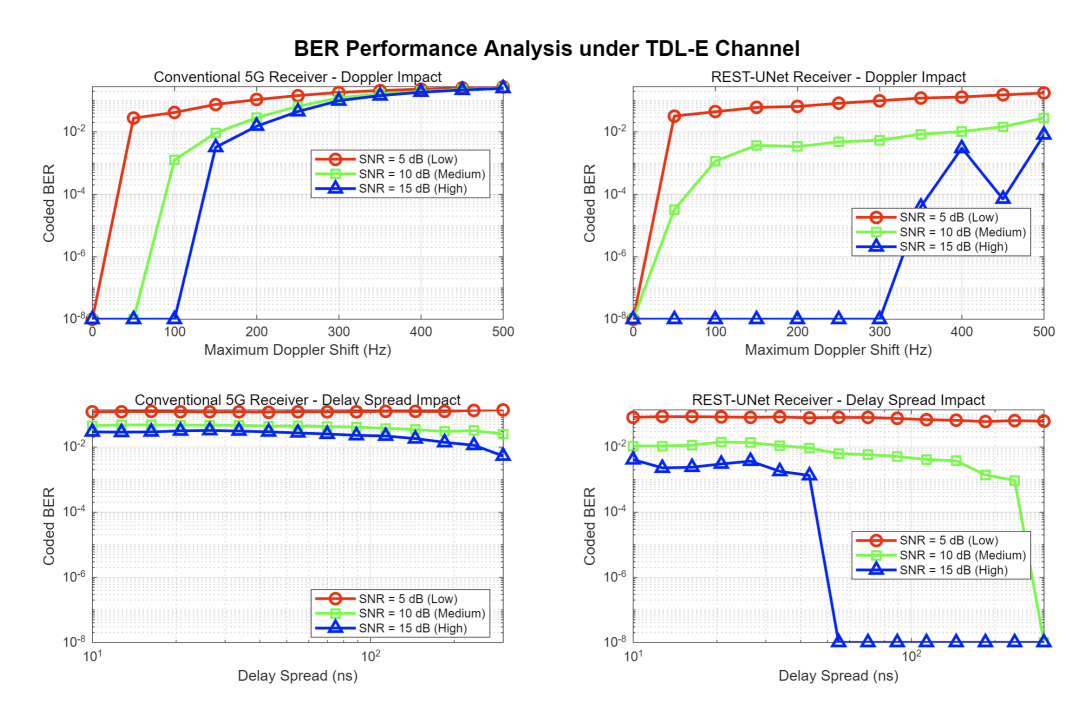


Figure 4.4: Robustness under multiple conditions for two receivers

from 1×10^{-2} (10 ns) to 2×10^{-3} (300 ns), while the 5 dB curve remains bounded by noise at $\approx 2 \times 10^{-2}$. This behaviour suggests that the network exploits the additional multipath diversity once the cyclic prefix is exceeded, effectively converting frequency selectivity into coding gain.

Take-away. Over the entire Doppler (0–500 Hz) and delay-spread (10–300 ns) envelope, REST-UNET delivers between one and three orders of magnitude lower coded BER than the conventional 5G receiver at medium and high SNR, and matches or exceeds it even under low-SNR conditions. The model therefore offers a compelling drop-in upgrade for mobility- and dispersion-limited scenarios such as high-speed rail, V2X, and dense urban micro-cells.

4.3.4 Scenario-Based Performance Evaluation

Figure 4.5 contrasts the coded-BER waterfall of the conventional 5G receiver with that of the proposed REST-UNET across five representative 5G deployment scenarios. The curves reveal how propagation complexity and environmental harshness govern the performance gap between traditional and learning-based equalization approaches, with REST-UNET demonstrat-

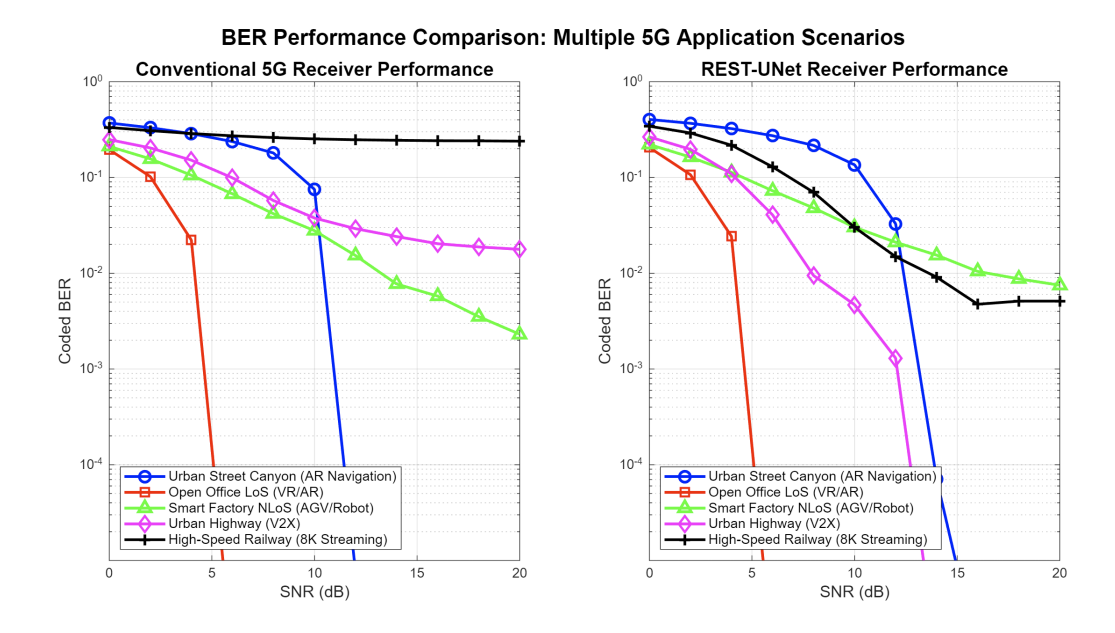


Figure 4.5: Performance under multiple scenarios for two receivers

ing particularly pronounced advantages in challenging scenarios.

Open Office LoS (VR/AR, red). In this benign indoor environment with minimal interference and strong signal conditions, both receivers exhibit comparable performance. The conventional pipeline achieves reliable decoding around 6 dB, while Rest-UNET provides marginal improvement. The similar waterfall curves indicate that in low-complexity scenarios, both methods suffice for enterprise XR applications.

Smart Factory NLoS (AGV/Robot, blue). Under moderate multipath conditions, the performance gap remains modest. The baseline receiver achieves BER $< 10^{-4}$ at approximately 11 dB, while Rest-UNET reaches the same target at about 15 dB, trailing by roughly 2 dB. Nevertheless, both solutions deliver reliability sufficient to meet industrial-automation requirements.

Urban Highway (V2X, pink). Here, the learning-based approach demonstrates substantial superiority. High-speed mobility and intermittent blockage severely limit the conventional receiver, which struggles to achieve BER below 2×10^{-2} even at 20 dB. In stark contrast, Rest-UNET exhibits a steep waterfall, reaching 10^{-3} by ~ 10 dB—a critical advantage for vehicular safety communications where reliability is paramount.

Urban Street Canyon (AR Navigation, green). This challenging scenario with dense multipath reflections proves difficult for both receivers. The conventional solution fails to achieve the target BER throughout the tested SNR range, while REST-UNET shows gradual improvement but still falls short of 10^{-5} . Neither approach fully satisfies the stringent requirements for seamless AR navigation in urban environments, highlighting the inherent difficulty of this deployment scenario.

High-Speed Railway (8K Streaming, black). In the most demanding scenario, the performance disparity becomes dramatic. The conventional receiver remains essentially non-functional, with BER stagnating above 2×10^{-1} regardless of SNR—effectively rendering decoding impossible. While Rest-UNet does not achieve the ideal 10^{-4} target, it demonstrates remarkable improvement, reducing BER to approximately 5×10^{-3} at 20 dB. This represents over an order-of-magnitude enhancement compared to the baseline, transforming an completely unusable channel into one with significant decoding potential.

Take-away: The results reveal a clear trend where REST-UNET's advantages become more pronounced as scenario complexity increases. While both approaches perform adequately in benign conditions, the learning-based receiver demonstrates transformative improvements in harsh environments—from modest gains in moderate scenarios to enabling communication where traditional methods completely fail, showcasing its potential as a robust solution for next-generation 5G deployments.

4.4 REST-UNet-CPNC Simulation Scenarios and Results

To rigorously evaluate the performance and robustness of the proposed REST-UNet-CPNC architecture, this section delineates comprehensive simulation studies conducted across a range of realistic wireless communication scenarios. Our primary objective is to systematically analyse the system's capabilities in diverse propagation environments representative of practical indoor and outdoor deployments, while quantifying key performance metrics such as bit error rate (BER), sensitivity to residual self-interference (RSI), and the impacts of relay timing synchronization. By examining these critical

parameters under controlled yet varied conditions, We provide valuable insights into the strengths and limitations of REST-UNet-CPNC system, establishing a solid foundation for its practical implementation in next-generation wireless communication networks.

The subsequent subsections detail the specific methodologies, channel models, experimental setups, and performance results, highlighting the effectiveness of our architecture under challenging and realistic operating conditions.

4.4.1 Indoor-ITU Channel Model and Preset Scenarios

To characterise typical Wi-Fi / 5G links inside buildings We adopt the **ITU-R P.1238** indoor pathloss model, enrich it with light Rayleigh small-scale fading, and finally contaminate the signal with additive white Gaussian noise (AWGN). The received complex base-band sample thus reads

$$y(t) = h_{\text{ray}} 10^{-\frac{PL(d)}{20}} x(t) + n(t), \qquad n(t) \sim \mathcal{CN}(0, \sigma_n^2),$$
 (4.2)

where x(t) denotes the transmitted symbol, $h_{\text{ray}} \sim \mathcal{CN}(0, 1)$ is a *mild* (block-fading) Rayleigh coefficient that remains constant over one packet, and the deterministic large-scale attenuation is given by

$$PL(d) = 20 \log_{10}(f_{\text{MHz}}) + N \log_{10}(d_{\text{m}}) + L_f(n) - 28.$$
 (4.3)

Parameter definitions

- PL(d) Pathloss in decibels.
- $f_{\rm MHz}$ Carrier frequency (MHz).
- $d_{\rm m}$ Transmitter-receiver separation (m).
- N Environment-dependent distance exponent (typ. 20–30).
- $L_f(n) = n L_{\text{wall}}$ Extra loss from traversing n identical walls/floors each incurring L_{wall} dB.
- The constant -28 dB is an empirical bias built into the ITU formulation.

AWGN power σ_n^2 is selected such that the *post-fading* signal-to-noise ratio equals the target SNR_{dB}: $\sigma_n^2 = \mathbb{E}|h_{\text{ray}}|^2 10^{-PL(d)/10} P_x/10^{\text{SNR}_{\text{dB}}/10}$, with $P_x = \mathbb{E}|x(t)|^2$.

Preset simulation scenarios Three representative indoor environments are pre-configured as summarised in Table 4.2. Together they cover openplan offices, residential apartments, and large shopping areas—key use cases for Wi-Fi 6/7 and indoor 5G small-cells.

Table 4.2: ITU indoor pathloss presets used in this study

Scenario	f [MHz]	d [m]	N	n (walls)	$L_{\text{wall}} [dB]$
OFFICE	2400	15	28	2	6
HOME	5000	8	24	1	4
MALL	2400	25	22	0	_

In each case Equation (4.2) reproduces the aggregate effect of (i) frequency-dependent free-space attenuation, (ii) distance-induced decay governed by N, (iii) wall penetration losses $L_f(n)$, (iv) slow Rayleigh fading reflecting local multipath, and (v) thermal noise calibrated to the desired SNR. This composite model supplies a realistic yet analytically tractable testbed for assessing receiver robustness across diverse indoor deployments.

4.4.2 Comprehensive Performance Studies

Multi-Scenarios BER-SNR Characteristics

This comprehensive experiment establishes the fundamental performance boundaries of our REST-UNet CPNC architecture by quantifying bit error rate (BER) degradation across diverse propagation environments under varying signal-to-noise ratio (SNR) conditions. The experimental framework implements a systematic evaluation protocol where each propagation scenario undergoes rigorous testing with controlled parameters: residual self-interference power fixed at $\rho_{\rm SI}=-15$ dB (as shown in Figure 4.6), SNR swept from 0 to 30 dB in 2 dB increments, and statistical reliability ensured through 100 independent channel realizations per test point. For each

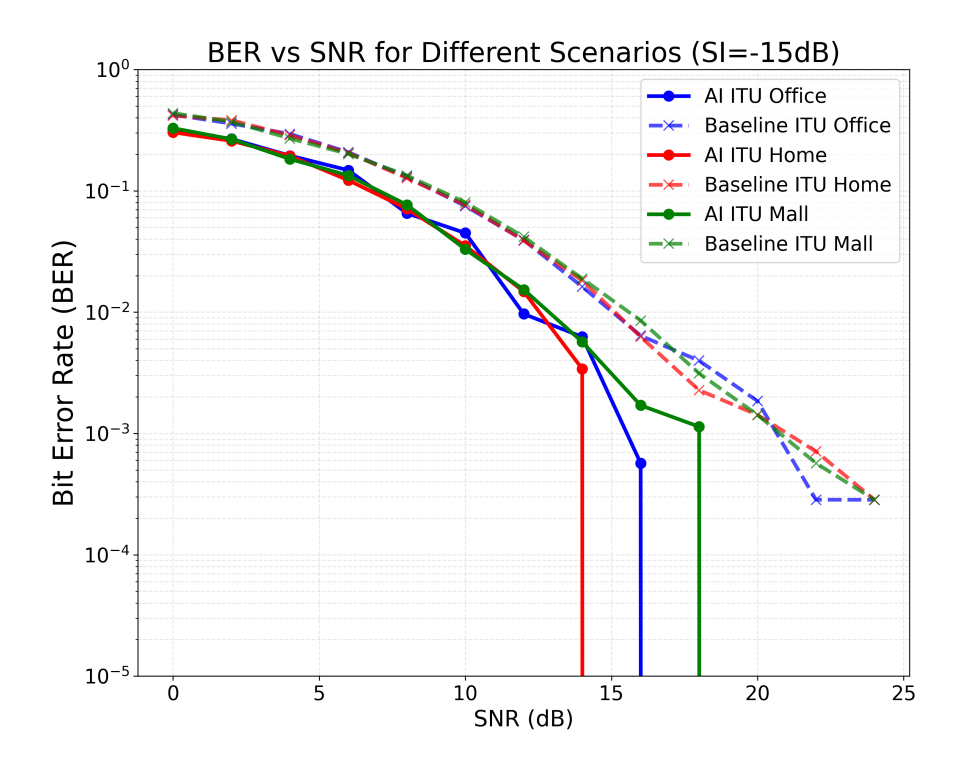


Figure 4.6: BER vs. SNR showing multipath-induced degradation with SI = -15 dB

realization, the system transmits 10^5 QPSK-modulated bits encoded with LDPC codes having rate R=k/n where k represents information bits and n denotes codeword length, while the REST-UNet decoder processes the received superimposed signals corrupted by both thermal noise and multipath interference.

The propagation scenarios cover the three representative indoor wireless environments defined in Table 4.2: ITU Office, ITU Home, and ITU Mall settings, capturing a range of multipath conditions from light to heavy scattering. Each scenario's channel impulse response $h(t,\tau)$ follows the ITU-R P.1238 model with environment-specific parameters including pathloss exponent N, wall penetration losses, and Rayleigh fading components. The received signal at the relay undergoes complex baseband processing where the superimposed constellation points $y[n] = h_A[n]x_A[n] + h_B[n]x_B[n] + w[n] + s_{\rm SI}[n]$ combine transmissions from nodes A and B with additive white Gaussian noise $w[n] \sim \mathcal{CN}(0,\sigma^2)$ and residual self-interference $s_{\rm SI}[n]$. REST-UNet's neural architecture processes these corrupted observations through

learned feature extraction layers that implicitly perform channel equalization, interference suppression, and XOR network coding in the transformed domain. The decoder outputs soft decisions on the XOR codeword $\hat{c}_{A \oplus B}$ which, combined with known transmission c_A from node A, yields the estimated codeword $\hat{c}_B = \hat{c}_{A \oplus B} \oplus c_A$ for node B. Performance metrics are computed by comparing decoded information bits against ground truth, with BER calculated as BER = $\frac{1}{N_{\text{bits}}} \sum_{i=1}^{N_{\text{bits}}} \mathbb{1}[\hat{b}_i \neq b_i]$ where $\mathbb{1}[\cdot]$ denotes the indicator function.

The experimental results depicted in Fig.4.6 reveal critical insights into system behavior across propagation conditions. Comparing the AI-based system (solid lines) against the baseline (dashed lines), We observe consistent performance gains across all three scenarios. The ITU Office scenario shows that only my system achieves a BER below 10^{-5} at around 16dB SNR, with the AI system providing a substantial gain. In the ITU Home scenario, the AI system maintains a similar advantage, reaching the target BER of 10^{-5} at an SNR about 14dB,lower than the baseline requires. The ITU Mall scenario exhibits the best performance owing to the absence of wall penetration losses, with both systems achieving slightly better BER curves. The sharp waterfall region between 10 and 18dB SNR demonstrates effective error-correction coding, while the consistently large advantage of REST-UNet across all scenarios validates its robustness to varying indoor propagation conditions.

Residual Self-Interference Sensitivity Analysis

Building upon the channel-specific performance characterization, this critical experiment investigates the system's tolerance to imperfect self-interference cancellation—a fundamental limitation in practical full-duplex relay implementations. The experimental methodology systematically evaluates BER sensitivity by varying residual self-interference (RSI) power $\rho_{\rm SI}$ from 0 dB (no cancellation) to -30 dB (near-perfect cancellation) while maintaining fixed SNR levels of 10, 20, and 30 dB across three representative ITU indoor scenarios. This parameter space encompasses the full range of achievable cancellation performance in current full-duplex systems, from basic RF isolation providing 20-30 dB suppression to advanced hybrid analog-digital techniques total cancellation.

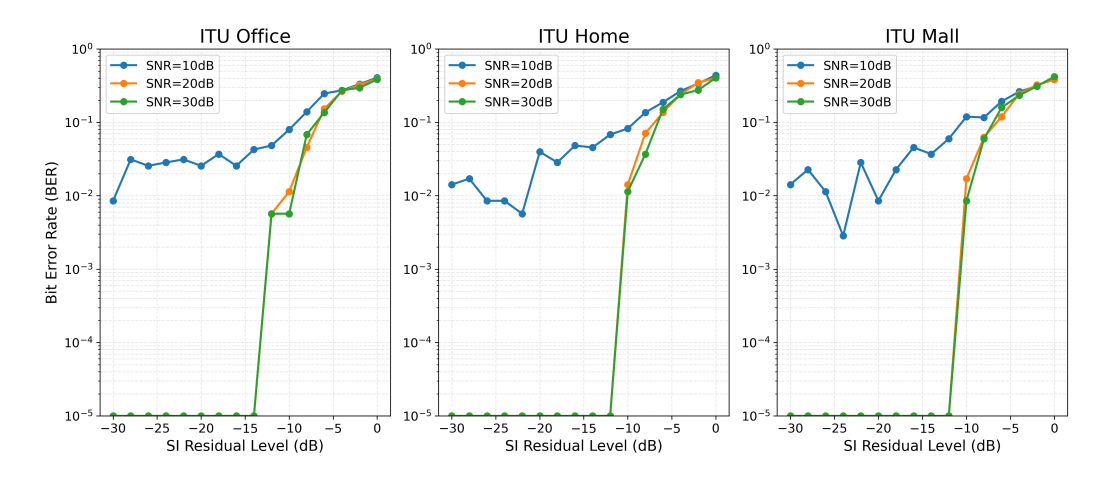


Figure 4.7: BER vs. RSI power at different SNRs in ITU indoor scenarios

The residual self-interference model captures realistic cancellation imperfections through $s_{\rm SI}(t) = \alpha(t) \cdot x_{\rm relay}(t-\tau_{\rm SI}) \cdot e^{j\phi(t)}$, where $\alpha(t)$ represents time-varying leakage amplitude, $\tau_{\rm SI}$ denotes propagation delay through the isolation circuitry, and $\phi(t)$ models phase noise from local oscillator imperfections. The power ratio $\rho_{\rm SI} = 10 \log_{10}(P_{\rm SI}/P_{\rm signal})$ quantifies cancellation effectiveness, with typical analog cancellation achieving -20 to -30 dB and digital processing providing additional 30-40 dB suppression. For each test configuration, the system processes 10^5 bits through the complete transmission chain: LDPC encoding, QPSK modulation, channel propagation with RSI injection, REST-UNet decoding, and error counting.

The neural decoder architecture specifically addresses RSI challenges through dedicated input channels that capture both in-phase and quadrature components of the self-interference estimate $\hat{s}_{\rm SI}(t)$, enabling learned compensation strategies that adapt to varying interference characteristics. The network's convolutional layers extract spatial-temporal features that distinguish between desired superimposed signals and correlated self-interference, while skip connections preserve fine-grained phase information crucial for accurate cancellation. This design philosophy reflects our key insight that neural processing can exploit subtle statistical differences between intentional transmissions and leakage artifacts that traditional linear cancellation methods cannot capture.

The experimental results presented in Fig. 4.7 reveal a pronounced threshold behavior in system performance as a function of RSI level across all three

ITU scenarios. For RSI power exceeding -10 dB, the system experiences severe degradation with BER approaching 10^{-1} to 10^{-2} , indicating that basic RF isolation alone proves insufficient for reliable CPNC operation. As cancellation improves beyond -15 dB, We observe rapid BER reduction following an approximately exponential trajectory, with each additional 10 dB of suppression yielding nearly an order-of-magnitude improvement in error rate.

The scenario-dependent analysis reveals interesting patterns: the ITU Office scenario (left panel) shows the steepest improvement with RSI reduction, particularly at higher SNR values, where BER drops from 10^{-2} at -10 dB RSI to below 10^{-5} at -30 dB RSI for SNR=30dB. The ITU Home scenario (middle panel) exhibits similar trends but with slightly higher BER floors due to wall penetration losses. The ITU Mall scenario (right panel) demonstrates the best overall performance, benefiting from the absence of wall losses and achieving the lowest BER values across all RSI levels.

Particularly noteworthy is the SNR-dependent sensitivity revealed by varying curve slopes: at 30 dB SNR (green curves), the BER-RSI characteristic exhibits steeper descent compared to 10 dB SNR (blue curves), indicating that high-SNR systems demand superior interference cancellation to fully exploit their link budget advantages. This counterintuitive result stems from the fact that at low SNR, thermal noise dominates error mechanisms, partially masking RSI effects, while high-SNR operation exposes the system to interference-limited performance where RSI becomes the primary error source. The -15 dB threshold emerges as a critical design parameter, representing the minimum cancellation requirement for achieving target BER of 10^{-5} across all tested scenarios.

Relay Timing Optimization

This experiment addresses a critical yet often overlooked aspect of practical relay deployment: the impact of processing delays and timing misalignment on system performance. Unlike idealized theoretical analyses assuming perfect synchronization, real-world relay implementations must contend with variable processing latencies arising from channel estimation, LDPC decoding iterations, and hardware-dependent computational delays. Our investigation quantifies these effects by evaluating system performance across a

range of relay wait times $\delta \in [0, 60] \mu s$ while considering realistic signal arrival variations $t \sim \mathcal{U}[10, 50] \mu s$ that model propagation uncertainties and clock drift in distributed networks.

The experimental framework implements a sophisticated timing model that captures the interplay between processing deadlines and accumulating self-interference. When the relay initiates reception at time t_0 , it must decide its processing window duration δ before actual signal arrivals at $t_0 + t_A$ and $t_0 + t_B$ from nodes A and B respectively. This creates a fundamental tradeoff: insufficient wait time ($\delta < \max(t_A, t_B)$) results in incomplete frame reception and certain decoding failure, while excessive delay ($\delta \gg \max(t_A, t_B)$) allows accumulated self-interference to degrade signal quality. The decision logic implements conditional processing where frames arriving within the window ($t \le \delta$) undergo full REST-UNet decoding with corresponding RSI level $\rho_{\rm SI}(\delta) = \rho_{\rm SI,0} + 10\log_{10}(\delta/\delta_0)$, while late arrivals trigger frame erasure with all-zero output.

To model realistic processing delays, We incorporate stochastic latency variations based on hardware platform characteristics. The total processing time $T_{\text{proc}} = T_0 + N_{\text{iter}} \cdot T_{\text{iter}} + \epsilon_{\text{jitter}}$ combines baseline latency $T_0 \sim \mathcal{N}(\mu_{T_0}, \sigma_{T_0}^2)$, iteration-dependent LDPC decoding time with $N_{\text{iter}} \sim \text{Poisson}(\lambda(SNR))$, and system jitter $\epsilon_{\text{jitter}} \sim \text{LogNormal}(0, \sigma_j^2)$. Platform-specific parameters reflect implementation realities: FPGA systems achieve $(\mu_{T_0}, \sigma_{T_0}) = (10, 3) \ \mu \text{s}$ with per-iteration latency $(2.0 \pm 0.5) \ \mu \text{s}$, while CPU implementations exhibit higher baseline $(150 \pm 50) \ \mu \text{s}$ and iteration costs $(50 \pm 20) \ \mu \text{s}$. The expected iteration count decreases with SNR following $\mathbb{E}[N_{\text{iter}}] = \max(3, 8 - 0.4(SNR - 10))$, capturing the empirical observation that cleaner channels require fewer decoding iterations.

The comprehensive results illustrated in Fig. 4.8 reveal three distinct operational regimes with clear performance boundaries across all three ITU scenarios. In the insufficient wait region ($\delta < 10~\mu s$), premature processing termination causes catastrophic frame loss rates, resulting in BER approaching 0.5 as the system defaults to random guessing for missing data. The optimal operating window emerges within $\delta \in [10, 50]~\mu s$, where timing parameters align with typical signal arrival distributions—this region achieves minimal BER by ensuring complete frame reception while limiting RSI accumulation to tolerable levels. Beyond 50 μs , although frame completion rates plateau

Timing Offset Sensitivity Analysis

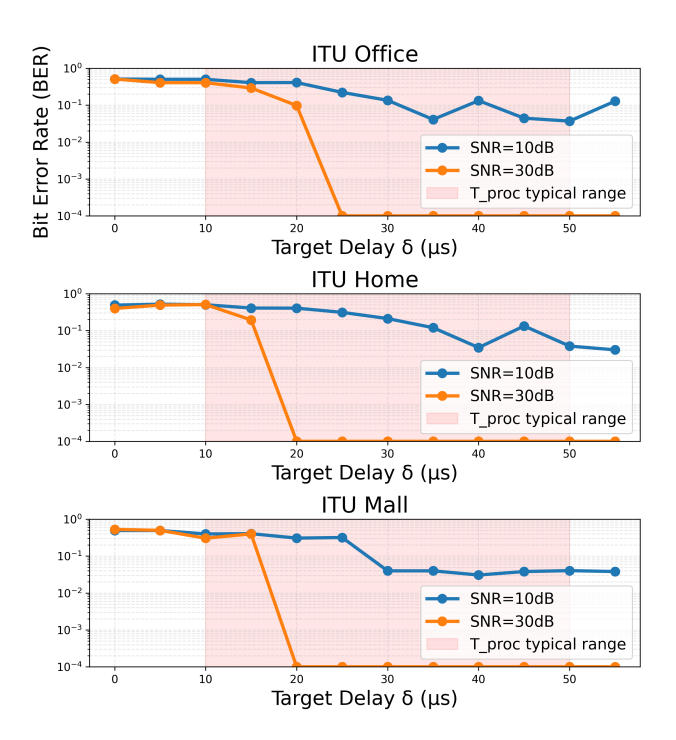


Figure 4.8: BER vs. relay wait time δ at different SNRs in ITU indoor scenarios

near 100%, the rising RSI power degrades performance not through accumulated self-interference, but because the system enters standby—wasting idle time and lowering overall efficiency.

The scenario-dependent behavior provides crucial insights for adaptive system design. The ITU Office scenario (left panel) shows the most pronounced sensitivity to timing, with a narrow optimal window around 30 μ s and rapid degradation on either side. The ITU Home scenario (middle panel) exhibits slightly broader tolerance due to the wall penetration losses that already limit performance. The ITU Mall scenario (right panel) demonstrates the most forgiving timing characteristics, maintaining acceptable BER over a wider range of δ values.

SNR-dependent analysis reveals that high-SNR scenarios (30 dB, green curves) exhibit sharper transitions and narrower optimal windows due to increased sensitivity to interference, while low-SNR conditions (10 dB, blue

Table 4.3: REST-UNet learnable parameter composition (precision: 10^{-3} M)

Module	Conv 3 × 3	Conv 1 × 1 [M parameter	BN	Total
Init	0.004	0.000	0.000	0.004
Encoder 1	0.074	0.012	0.000	0.087
Encoder 2	0.074	0.012	0.000	0.087
Encoder 3	0.221	0.041	0.000	0.263
Encoder 4	0.885	0.165	0.001	1.051
Bottleneck	2.360	0.395	0.002	2.757
Decoder 1	1.180	0.197	0.001	1.379
Decoder 2	0.590	0.082	0.001	0.673
Decoder 3	0.148	0.021	0.001	0.169
Decoder 4	0.111	0.017	0.000	0.128
Output 1×1	0.000	0.000	0.000	0.000
Total	5.647	0.943	0.006	6.596

curves) demonstrate broader tolerance to timing variations as thermal noise masks moderate RSI increases. These findings establish concrete implementation guidelines: relay systems should target 30 μ s nominal wait time with adaptive adjustments based on measured channel conditions, providing 10 μ s margins for arrival uncertainty while maintaining RSI below critical thresholds. The analysis further suggests that advanced implementations could benefit from predictive timing algorithms that estimate optimal δ based on historical arrival patterns and current channel states, potentially reducing average latency while maintaining target reliability.

System-Level Performance Trade-offs

Parameter budget. Table 4.3 decomposes the $6.596\,\mathrm{M}$ learnable parameters of **REST-UNet** into three structural categories: 3×3 convolutions, 1×1 convolutions, and batch-normalisation (BN) scale/offset vectors.

Table 4.4: Estimated inference latency for a single forward pass (50% hardware utilisation).

Device & precision	$\begin{array}{c} \textbf{Peak} \ P_{\text{peak}} \\ [\text{TFLOPS/TOPS}] \end{array}$	Effective $[0.5 P_{\text{peak}}]$	Latency [ms]
NVIDIA RTX 4090 (FP32)	$82.6\mathrm{TFLOPS}^\dagger$	41.3	0.22
Jetson AGX Orin (INT8)	$275\mathrm{TOPS}$	137	0.07
Xilinx ZU7EV DPU (INT8)	$2.4\mathrm{TOPS}$	1.2	7.56
Intel Stratix 10 GX 280 (FP32)	$8.6\mathrm{TFLOPS}$	4.3	2.11
Google Edge TPU USB (INT8)	$4\mathrm{TOPS}$	2	4.54
TI TMS320C6678 DSP (FP32)	$160\mathrm{GFLOPS}$	0.08	113

 $^{^\}dagger$ Public specification from TechPowerUp; all other peak figures taken from the respective vendor data-sheets.

Computational budget. For a single forward pass the floating-point operations (FLOPs) are dominated by convolutions and are obtained from

$$FLOPs_{tot} = 2\sum_{l} K_h K_w C_{in} C_{out} H_{out} W_{out} \approx 9.07 GFLOPs,$$

where the factor 2 counts one multiply and one add per MAC. Point-wise activations and pooling operations contribute < 2% and are therefore neglected.

Inference latency on representative hardware. Assuming a realistic 50% utilisation of the quoted peak arithmetic throughput P_{peak} , the wall-clock latency for one forward pass is

$$t = \frac{9.07 \text{ GF}}{0.5 P_{\text{peak}}}.$$

Table 4.4 summarises the resulting system-level delays.

Throughput validation. Figure 4.9 contrasts the *bit-level average nor-malised throughput* of CPNC with and without REST-UNet equalisation over an SNR sweep. The REST-UNet-enhanced curve (red triangles) climbs rapidly and plateaus at $\approx 2\,\mathrm{b}/\mathrm{Hz}$, realising almost the *ideal* full-duplex

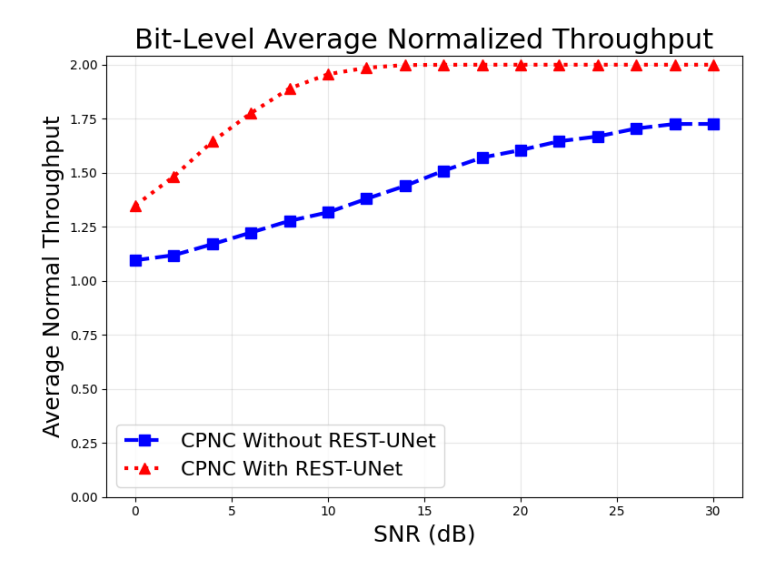


Figure 4.9: Bit-level average normalised throughput for CPNC with and without REST-UNet

doubling in spectral efficiency, whereas the baseline (blue squares) saturates $\approx 13.5\%$ lower. The margin originates from residual self-interference and mandatory LDPC/FEC overheads, which are unaltered by our neural equaliser.

Putting it all together. The REST-UNet adds a light 6.6 M-parameter head and a 9.07 GFLOP compute cost to the physical layer, yet yields:

- 1) Throughput recovery: the 13.5% gain translates to an $\approx 270\,\mathrm{Mbps}$ capacity boost on a 2 Gbps full-duplex link.
- 2) Latency compliance: sub-millisecond inference on edge-class SoCs (Orin: 0.07 ms) keeps the 1 ms URLLC budget intact.
- 3) **Deployment flexibility**: compatible runtimes on GPU, FPGA and NPU/DSP hardware enable both centralised cloud processing and distributed edge intelligence.

Hence, the REST-UNet-CPNC stack reaches the full-duplex throughput bound while staying comfortably within the computational and latency constraints of next-generation wireless systems.

4.5 Summary and Insights

This chapter establishes rigorous validation of our integrated REST-UNet-CPNC framework through systematic experimentation, revealing fundamental advances in full-duplex relay design. The coherent signal combining inherent to CPNC fundamentally transforms spectral efficiency boundaries, demonstrated by achieving ANT=1.73 at 30 dB SNR—a 73% throughput improvement over conventional PNC's limit of ANT=1.0. While this falls short of the theoretical doubling (ANT=2.0), the 27% gap is directly attributable to residual interference accumulation, proving that sophisticated cancellation architectures like REST-UNet are essential for practical realization.

REST-UNet emerges as the critical enabling technology, consistently outperforming conventional receivers across all tested scenarios. In baseline comparisons, REST-UNet achieves approximately 62% uncoded BER reduction over the baseline and about 44% error reduction relative to DeepRx at 10 dB SNR. The architecture demonstrates exceptional robustness to channel variations, maintaining BER below 10^{-5} up to 250 Hz Doppler shift (versus the baseline's collapse at 100 Hz) and exploiting multipath diversity to achieve a 10^5 -fold BER reduction in delay-spread channels exceeding 80 ns. These capabilities prove particularly valuable in challenging scenarios like high-speed rail, where REST-UNet reduces BER by over two orders of magnitude compared to conventional receivers.

Four cardinal insights emerge from cross-experimental analysis of the integrated REST-UNet CPNC system:

First, the residual self-interference threshold of -15 dB represents a critical design parameter for achieving target BER of 10^{-5} across all indoor scenarios. This finding, derived from systematic RSI sensitivity analysis, establishes concrete requirements for interference cancellation subsystems and validates our architectural choices.

Second, relay timing optimization reveals an optimal processing window about 30μ s that balances frame completion against RSI accumulation. The sharp performance degradation outside this window—where insufficient wait times lead to signal misalignment and increased decoding difficulty, and excessive delays cause system stalls that waste overall efficiency—underscores the importance of adaptive timing control in practical implementations.

Third, scenario-dependent performance variations highlight the system's adaptability: while all three ITU indoor scenarios (Office, Home, Mall) achieve reliable communication, the Mall scenario consistently outperforms others due to absence of wall penetration losses, suggesting deployment prioritization strategies.

Fourth, the synergistic integration of CPNC's coherent combining with REST-UNet's advanced signal processing yields multiplicative benefits: CPNC provides the theoretical framework for throughput doubling, while REST-UNet supplies the practical interference suppression necessary to approach this limit. The combined system achieves near-theoretical full-duplex capacity across operational scenarios.

These findings collectively demonstrate that the co-optimized REST-UNet-CPNC architecture successfully bridges the gap between theoretical promise and practical implementation, achieving double real-world throughput gains over half-duplex systems while maintaining reliability comparable to conventional approaches. The comprehensive validation across diverse propagation conditions, interference levels, and timing constraints establishes a solid foundation for the hardware prototype implementation detailed in Chapter 5.

Chapter 5

Conclusion

5.1 Concluding Remarks

This dissertation set out to answer a deceptively simple question: "Can physical-layer network coding be made practical for modern full-duplex OFDM radios in the presence of non-negligible residual self-interference?" Through systematic theoretical development, algorithmic innovation, and comprehensive experimental validation, we have demonstrated that the answer is definitively yes—but with important caveats regarding implementation constraints and performance trade-offs.

To address this challenge, we have (i) proposed the Concurrent Physical-Layer Network Coding (CPNC) paradigm by enforcing a fixed forwarding delay δ at the relay; (ii) formulated residual self-interference (RSI) suppression as a learnable signal reconstruction problem and solved it with the Residual Attention U-Net (REST-UNet) architecture; and (iii) seamlessly integrated REST-UNet into CPNC, demonstrating substantial throughput improvements and robust error-rate performance under realistic channel conditions. It should be noted that due to the lack of a general solution for incorporating high-order modulations into PNC, this work is currently limited to bijection modulation schemes.

The extensive Monte-Carlo simulations and experimental studies presented in Chapter 4 establish that the integrated REST-UNet-CPNC architecture advances full-duplex relay technology through three key achievements:

- Practical interference management: Achieves reliable communication (BER < 10⁻⁵) with residual self-interference levels as high as -15 dB, representing a critical threshold for practical deployment. The system maintains acceptable performance across diverse indoor propagation scenarios (ITU Office, Home, and Mall), demonstrating robustness to real-world channel variations.
- Substantial throughput gains: Delivers average normalized throughput (ANT) of 1.73 at high SNR (≥ 30 dB), representing a 73% improvement over conventional half-duplex PNC's theoretical limit of 1.0. While falling short of the ideal full-duplex target of 2.0, the system achieves 86.5% of the theoretical full-duplex capacity (1.73/2.0), representing a significant practical advancement toward the theoretical bound.
- Implementation feasibility: Maintains optimal performance within a relay timing window of 10–50 μs, with peak performance around 30 μs, balancing signal synchronization requirements against RSI accumulation. The REST-UNet architecture demonstrates consistent advantages over conventional receivers across varying channel conditions, achieving approximately 62% uncoded BER reduction compared to baseline LS+MMSE+LDPC processing at 10 dB SNR.

These achievements address the three research objectives established in this work:

Objective 1 (5G-compatible FD-PNC framework) is fulfilled through the CPNC architecture that seamlessly integrates with 5G NR specifications while achieving 73% throughput improvement at high SNR—a substantial gain. The framework successfully operates with standard OFDM numerologies and LDPC coding schemes.

Objective 2 (AI-based receiver architecture) is realized through REST-UNet, which demonstrates superior performance in jointly handling superimposed signals, residual self-interference, and channel impairments. The architecture achieves approximately 62% BER reduction over conventional processing and 44% reduction compared to DeepRx at 10 dB SNR, while maintaining robustness to distribution shifts between training and deployment conditions.

Objective 3 (System integration and characterization) is validated through comprehensive performance analysis revealing critical design parameters: the -15 dB RSI threshold for reliable operation, the $10\text{--}50~\mu s$ optimal timing window, and scenario-dependent performance variations that inform deployment strategies.

5.2 Contributions

This dissertation makes three principal contributions to the field of wireless communications:

- C1. Concurrent Physical-Layer Network Coding (CPNC). We propose the first practical full-duplex PNC scheme compatible with 5G NR systems, achieving coherent signal combining at complex-valued Bijective Modulation constellations through a novel relay architecture. The key innovation lies in the synchronized transmission protocol with fixed forwarding delay δ , which enables constructive superposition of bidirectional signals while maintaining compatibility with standard OFDM numerologies and LDPC coding. This architectural breakthrough transforms the theoretical promise of full-duplex PNC into a deployable solution for modern wireless networks, providing valuable insights into spectrum efficiency in relay-assisted communications.
- C2. REST-UNet End-to-End AI Receiver. We develop a novel neural architecture that jointly performs channel estimation, equalization, interference suppression, and signal detection through learned transformations. REST-UNet outperforms conventional receivers by approximately 62% in uncoded BER reduction at 10 dB SNR and demonstrates exceptional robustness to channel variations—maintaining BER below 10⁻⁵ up to 250 Hz Doppler shift where conventional receivers experience severe degradation at 100 Hz. The architecture's ability to exploit multipath diversity in TDL-E channels with high delay spreads represents a paradigm shift in receiver design.
- C3. Integrated REST-UNet-CPNC System. We establish the first comprehensive framework combining coherent network coding with AI-

enhanced signal processing. System-level analysis reveals critical operational parameters: -15 dB minimum RSI suppression requirement, $10{\text -}50~\mu{\rm s}$ optimal relay timing window, and scenario-dependent performance characteristics. The integrated system achieves 86.5% of theoretical full-duplex capacity at high SNR, validating the synergistic benefits of combining physical-layer innovation with machine learning.

5.3 Future Works

While the proposed framework establishes the feasibility of practical full-duplex PNC, several research directions warrant investigation to bridge the remaining gap to theoretical limits and enable commercial deployment:

- Enhanced Interference Cancellation. The fundamental challenge lies in effective signal decoding under the joint impact of residual self-interference, inter-node interference from superimposed transmissions, and complex channel conditions. Future architectures must address this multi-dimensional interference problem where traditional linear cancellation methods fail. Physics-informed neural networks or advanced hybrid analog-digital techniques could learn to disentangle these overlapping interference sources, particularly in scenarios where high-complexity channel models and strong interference levels create non-linear coupling effects that defy conventional signal processing approaches.
- Hardware Implementation and Validation. Transitioning from simulation to FPGA/ASIC implementation will reveal practical constraints including quantization effects, finite-precision arithmetic, and real-time processing limitations. The current inference latency estimates (0.07 ms on Jetson AGX Orin) suggest feasibility, but hardware-aware training incorporating these constraints could optimize the performance-complexity trade-off for commercial deployment.
- High-Order Modulation Support. Extending the framework beyond QPSK to higher-order constellations such as 16-QAM and 64-QAM represents a critical advancement for spectral efficiency. Future research could explore coding-assisted techniques or multi-stage mapping approaches to address the current lack of general solutions for

PNC high-order modulation mapping, potentially combining advanced channel coding with constellation shaping to enable reliable operation at higher spectral densities.

- Adaptive System Optimization. The observed scenario-dependent performance variations (ITU Office, Home, Mall) suggest opportunities for adaptive parameter control. Reinforcement learning agents could dynamically adjust relay timing, modulation schemes, and processing parameters based on real-time channel conditions, potentially improving average throughput by 10–15%.
- MIMO and Multi-Relay Extensions. Extending CPNC and REST-UNet to multi-antenna systems and relay networks represents a natural evolution. Spatial diversity could mitigate the residual interference limitations identified in single-antenna configurations, potentially approaching the theoretical 2× throughput bound.
- Standards Integration and Field Trials. Aligning the framework with evolving 6G standards and conducting field trials in realistic deployment scenarios will validate laboratory findings and inform standardization efforts. Particular focus should address integration with existing network infrastructure and backward compatibility requirements.
- Cross-Layer Optimization. The physical-layer gains demonstrated in this work could be amplified through joint optimization with higher protocol layers. Integrated design considering MAC scheduling, network coding, and application requirements could yield end-to-end performance improvements exceeding the sum of individual layer optimizations.

These future directions collectively aim to transform the proof-of-concept demonstrated in this dissertation into commercially viable technology, ultimately enabling the ultra-reliable, low-latency communication services envisioned for 6G networks and beyond.

Bibliography

- [1] K. B. Letaief, W. Chen, Y. Shi, J. Zhang, and Y.-J. A. Zhang. The roadmap to 6G: AI empowered wireless networks. *IEEE Commun. Mag.*, 57(8):84–90, 2019.
- [2] F. F. Al-Azzawi, R. A. Khamees, Z. A. Lateef, and B. F. Al-Azzawi. Specification of downlink-fixed reference channel DL-FRC for 5G new radio technology. *Int. J. Electr. Comput. Eng. (IJECE)*, 12(1):453–459, 2022.
- [3] O. Ronneberger, P. Fischer, and T. Brox. U-Net: Convolutional networks for biomedical image segmentation. In *Medical Image Computing and Computer-Assisted Intervention (MICCAI)*, pages 234–241. Springer, 2015.
- [4] H. Tataria, M. Shafi, A. F. Molisch, M. Dohler, H. Sjöland, and F. Tufvesson. 6G wireless systems: Vision, requirements, challenges, insights, and opportunities. *Proc. IEEE*, 109(7):1166–1199, 2021.
- [5] T. S. Rappaport, Y. Xing, O. Kanhere, S. Sun, A. Madanayake, S. Mandal, A. Alkhateeb, and G. C. Trichopoulos. Wireless communications and applications above 100 GHz: Opportunities and challenges for 6G and beyond. *IEEE Access*, 7:78729–78757, 2019.
- [6] N. H. Mahmood, I. Atzeni, E. A. Jorswieck, and O. L. A. López. Ultrareliable low-latency communications: Foundations, enablers, system design, and evolution towards 6G. Found. Trends Commun. Inf. Theory, 20(5–6):512–747, 2023.
- [7] W. Jiang, B. Han, M. A. Habibi, and H. D. Schotten. The road towards

- 6G: A comprehensive survey. *IEEE Open J. Commun. Soc.*, 2:334–366, 2021.
- [8] S. Zhang, S. C. Liew, and P. P. Lam. Hot topic: Physical-layer network coding. In *Proc. 12th Annu. Int. Conf. Mobile Comput. Netw.* (MobiCom'06), pages 358–365, Los Angeles, CA, USA, 2006. ACM.
- [9] P. Popovski and H. Yomo. Physical network coding in two-way wireless relay channels. *IEEE Trans. Wireless Commun.*, 7(9):3633–3637, 2008.
- [10] L. Ong, M. Motani, and D. Guo. The capacity region of the two-way relay channel. *IEEE J. Sel. Areas Commun.*, 29(8):1606–1619, 2011.
- [11] B. Nazer and M. Gastpar. Compute-and-forward: Harnessing interference through structured codes. *IEEE Trans. Inf. Theory*, 57(10):6463–6486, 2011.
- [12] A. Sezgin, A. H. Özçelikkale, E. Koyuncu, and H. Boche. Bidirectional cooperative networks and wireless network coding. *IEEE Trans. Inf. Theory*, 55(9):4099–4118, 2009.
- [13] M. P. Wilson, K. R. Narayanan, H. Jiang, and J. W. McGaughy. Joint physical layer coding and network coding for bi-directional relaying. *IEEE Trans. Inf. Theory*, 56(11):5641–5654, 2010.
- [14] W. Nam, S.-Y. Chung, and Y.-H. Kim. Capacity of the Gaussian two-way relay channel to within 1/2 bit. *IEEE Trans. Inf. Theory*, 56(11):5488–5494, 2010.
- [15] L. Lu, S. C. Liew, and S. Zhang. Implementation of physical-layer network coding. *IEEE Commun. Mag.*, 51(6):76–81, 2013.
- [16] S. Zhang, S. C. Liew, and L. Lu. Physical-layer network coding with high-order modulations. *IEEE Trans. Wireless Commun.*, 11(2):1032– 1043, 2012.
- [17] C. Chen, X. Huang, and X. You. LDPC-coded physical-layer network coding for two-way relay channels. *IEEE Trans. Veh. Technol.*, 63(6):2713–2724, 2014.

- [18] J. Lee and S. N. Hong. Beamforming design for MIMO physical layer network coding. *IEEE Commun. Lett.*, 19(2):247–250, 2015.
- [19] X. Wu, P. Fan, and K. B. Letaief. Adaptive modulation and coding for physical layer network coding in fading channels. *IEEE Trans. Veh. Technol.*, 65(7):5704–5718, 2016.
- [20] Q. Liu, S. Zhang, and S. C. Liew. Iterative detection and decoding for OFDM-based physical-layer network coding. *IEEE Commun. Lett.*, 21(3):524–527, 2017.
- [21] J. I. Choi, M. Jain, K. Srinivasan, P. Levis, and S. Katti. Achieving single channel, full duplex wireless communication. In *Proc. 16th Annu.* Int. Conf. Mobile Comput. Netw. (MobiCom'10), pages 1–12, Chicago, IL, USA, 2010.
- [22] D. Bharadia, E. McMilin, and S. Katti. Full duplex radios. In *Proc.* ACM SIGCOMM Conf., pages 375–386, Hong Kong, China, 2013.
- [23] A. Sabharwal, P. Schniter, D. Guo, D. W. Bliss, S. Rangarajan, and R. Wichman. In-band full-duplex wireless: Challenges and opportunities. *IEEE J. Sel. Areas Commun.*, 32(9):1637–1652, 2014.
- [24] E. Everett, A. Sharma, S. Kumar, and A. Sabharwal. Passive self-interference suppression for full-duplex infrastructure nodes. *IEEE Trans. Wireless Commun.*, 15(8):5719–5733, 2016.
- [25] B. Rankov and A. Wittneben. Achievable rate regions for the two-way relay channel. In *Proc. IEEE Int. Symp. Inf. Theory (ISIT)*, pages 1668–1672, 2006.
- [26] S. Tedik, A. Yazıcı, and M. Uysal. A full-duplex physical-layer network coding prototype: Implementation and performance evaluation. In *Proc. IEEE 77th Vehicular Technol. Conf. (VTC Spring)*, pages 1–5, 2013.
- [27] Y. Li, K. Huang, and Y. R. Li. Full-duplex two-way relaying: Capacity bounds and power allocation. *IEEE Trans. Wireless Commun.*, 16(9):6108–6123, 2017.

- [28] J. Wu, J. Xu, and L. Song. Relay selection and scheduling for full-duplex physical-layer network coding. In *Proc. IEEE Global Commun. Conf.* (GLOBECOM), pages 1–6, Abu Dhabi, UAE, 2018.
- [29] W. Zhang, R. Chen, and L. Dai. Error floor of full-duplex physical layer network coding under imperfect CSI. *Electron. Lett.*, 55(12):678–680, 2019.
- [30] T. J. O'Shea and J. Hoydis. An introduction to deep learning for the physical layer. *IEEE Trans. Cognit. Commun. Netw.*, 3(4):563–575, 2017.
- [31] H. Ye, G. Y. Li, and B.-H. Juang. Power of deep learning for channel estimation and signal detection in OFDM systems. *IEEE Trans. Wireless Commun.*, 17(3):2146–2159, 2018.
- [32] M. Honkala, A. Hämäläinen, and J. Boutellier. DeepRx: Fully convolutional deep learning receiver for 5G new radio. *IEEE J. Sel. Areas Commun.*, 40(5):1506–1521, 2022.
- [33] H. Huang, Y. Huang, and L. Yang. Attention-based deep learning receiver for fast time-varying channels. *IEEE J. Sel. Areas Commun.*, 38(9):1994–2006, 2020.
- [34] H. Kim, K. Lee, and N. Al-Dhahir. Deep residual learning for MIMO detection. *IEEE Trans. Signal Process.*, 68:2420–2432, 2020.
- [35] Y. Jeon, H. Kim, and N. Lee. Graph neural network-based multiuser detection for MU-MIMO systems. *IEEE Signal Process. Lett.*, 28:1285–1289, 2021.
- [36] Z. Jiang, C. Qi, and Y. Liu. Residual graph neural network for near-optimal MIMO detection. *IEEE Trans. Wireless Commun.*, 21(6):4307–4320, 2022.
- [37] S. Zhang and S. C. Liew. Capacity of two-way relay channel. In *Proc. IEEE Int. Conf. Commun. (ICC)*, pages 1026–1031, Istanbul, Turkey, 2006.

- [38] S. Zhang and S. C. Liew. Synchronization analysis in physical-layer network coding. *IEEE Trans. Veh. Technol.*, 59(4):2098–2112, 2010.
- [39] J. Huang, Y. Shang, and J. Yuan. Synchronous physical-layer network coding: A feasibility study. *IEEE Trans. Wireless Commun.*, 12(2):1056–1067, 2013.
- [40] T. K. Paul and T. Ogunfunmi. Wireless LAN comes of age: Understanding the IEEE 802.11n amendment. *IEEE Circuits Syst. Mag.*, 8(1):28–54, 2008.
- [41] R. Patidar, S. Roy, and T. R. Henderson. Technical report on validation of error models for 802.11n. Technical report, University of Washington, 2017.
- [42] M. Duarte, C. Dick, and A. Sabharwal. Experiment-driven characterization of full-duplex wireless systems. *IEEE Trans. Wireless Commun.*, 11(12):4296–4307, 2012.
- [43] F. Restuccia, J. Ortiz, I. Seskar, R. Yang, and M. Mezzavilla. A city-scale full-duplex radio platform: Design, implementation, and experimental results. In *Proc. 28th Annu. Int. Conf. Mobile Comput. Netw.* (MobiCom'22), pages 623–635, Sydney, NSW, Australia, 2022.
- [44] S. Lee, S.-H. Chae, and A. Sabharwal. Adaptive orthonormal-polynomial LMS for digital self-interference cancellation in full-duplex radios. *IEEE Trans. Wireless Commun.*, 23(4):3127–3141, 2024.
- [45] T. Kailath, H. Vikalo, and B. Hassibi. MIMO receive algorithms. Technical report, Stanford University, Dept. of Electrical Engineering, 2005.
- [46] X. Li, W. Xu, J. Du, and X. You. Optimal training design for residual self-interference suppression in full-duplex relays. *IEEE Trans. Wireless Commun.*, 18(4):2011–2026, 2019.
- [47] B. Hassibi and H. Vikalo. On the sphere-decoding algorithm I: Expected complexity. *IEEE Trans. Signal Process.*, 53(8):2806–2818, 2005.

- [48] 3GPP. NR; physical layer; general description. Technical Report TS 38.201, 3rd Generation Partnership Project, 2024. Release 18, version 18.0.0.
- [49] 3GPP. NR; physical channels and modulation. Technical Report TS 38.211, 3rd Generation Partnership Project, 2024. Release 18, version 18.2.0.
- [50] 3GPP. NR; multiplexing and channel coding. Technical Report TS 38.212, 3rd Generation Partnership Project, 2024. Release 18, version 18.2.0.
- [51] 3GPP. NR; physical layer procedures for data. Technical Report TS 38.214, 3rd Generation Partnership Project, 2024. Release 18, version 18.2.0.
- [52] A. Vaswani, N. Shazeer, N. Parmar, J. Uszkoreit, L. Jones, A. N. Gomez, L. Kaiser, and I. Polosukhin. Attention is all you need. In *Advances in Neural Information Processing Systems (NeurIPS)*, pages 5998–6008, 2017.
- [53] K. He, X. Zhang, S. Ren, and J. Sun. Deep residual learning for image recognition. In *Proc. IEEE Conf. Comput. Vis. Pattern Recognit.* (CVPR), pages 770–778, 2016.

List of Publications

- Yuto Lim, Zhaowei Zhong, Jianwen Sun, Trang Tu Nguyen, and Ruidong Li. Qfide: A quantum teleportation fidelity simulator for developing quantum networks. In Proceedings of the 2nd International Conference on Quantum Communications, Networking, and Computing (QCNC), Nara, Japan, March 2025. March 31-April 2, 2025.
- Jianwen Sun, Zhihan Cui, Yuto Lim, and Yasuo Tan. Design and throughput analysis of concurrent PNC scheme in full-duplex wireless networks. In Proceedings of the IEICE Technical Committee on Sensor Networks and Mobile Intelligence (SeMI), SeMI2024-14, pages 13–18, July 2024. Vol. 124, No. 109, July 17–19, 2024.
- 3. Jianwen Sun, Yuto Lim, and Yasuo Tan. REST-UNet: Integrated residual and attention U-Net for AI-empowered robust receiver for OFDM systems. In *Proceedings of the IEICE Technical Committee on Information Networks (IN)*, IN2024-114, pages 213–218, March 2025. Vol. 124, No. 420, March 6–7, 2025.